

Title	Two-dimensional semiconductors for future electronics
Authors	Mirabelli, Gioele
Publication date	2020
Original Citation	Mirabelli, G. 2020. Two-dimensional semiconductors for future electronics. PhD Thesis, University College Cork.
Type of publication	Doctoral thesis
Rights	© 2020, Gioele Mirabelli. - https://creativecommons.org/licenses/by-nc-nd/4.0/
Download date	2024-04-23 09:56:59
Item downloaded from	https://hdl.handle.net/10468/10151

OLLSCOIL NA HÉIREANN, CORCAIGH

NATIONAL UNIVERSITY OF IRELAND, CORK



**TWO-DIMENSIONAL SEMICONDUCTORS
FOR FUTURE ELECTRONICS**

THESIS PRESENTED BY

GIOELE MIRABELLI

FOR THE DEGREE OF

DOCTOR OF PHILOSOPHY

UNIVERSITY COLLEGE CORK

SCHOOL OF ELECTRICAL ENGINEERING

TYNDALL NATIONAL INSTITUTE

HEAD OF SCHOOL: PROF. WILLIAM P. MARNANE

SUPERVISORS: DR. RAY DUFFY, PROF. PAUL HURLEY, DR. SCOTT MONAGHAN

2020

Table of Content

ABSTRACT	XI
CHAPTER 1: INTRODUCTION.....	1
1.1 Background and motivation	1
1.2 2D-Materials properties and applications	4
1.2.1 Crystal structure	4
1.2.2 Growth of TMDs.....	8
1.2.3 Optoelectronic applications.....	10
1.2.4 Electronic applications.....	12
1.2.5 Comparison and advantages of TMDs for electronics applications	13
1.3 Challenges of 2D-Materials.....	17
1.3.1 Defects and impurities	17
1.3.2 Metal-TMD interface: Schottky barrier and Fermi-level Pinning effect.....	20
1.3.3 Modelling capabilities.....	24
1.4 Thesis structure	30
CHAPTER 2: AIR SENSITIVITY OF TMDS	33
2.1 Introduction	34
2.2 Experimental.....	34
2.3 Surface and cross-sectional analysis	36
2.4 EDX and XPS analysis	45
2.5 Discussion	50
2.6 Conclusions	54
CHAPTER 3: THE EFFECT OF IMPURITIES AND DIELECTRIC ENVIRONMENT ON 2D-SEMICONDUCTORS	55
3.1 Introduction	56
3.2 Experimental.....	56
3.3 Material analysis.....	57
3.4 Electrical analysis	59
3.4.1 Extraction of impurity concentration	59
3.4.2 Effect of the dielectric environment.....	67
3.5 Discussion	73
3.6 Conclusions	75

CHAPTER 4: CONTACT RESISTANCE STUDY OF HIGHLY DOPED P-TYPE MOS₂	77
4.1 Introduction	78
4.2 Experimental	78
4.3 Device fabrication	78
4.4 Electrical characterisation	79
4.5 Doping extraction	80
4.6 Discussion	82
4.7 Conclusions	88
CHAPTER 5: EFFECTS OF ANNEALING TEMPERATURE AND AMBIENT ON METAL-PTSE₂ INTERFACE	89
5.1 Introduction	90
5.2 Experimental	92
5.3 Experimental results	93
5.4 Discussion	103
5.5 Conclusions	104
CHAPTER 6: TCAD MODELLING AND ANALYSIS OF MOS₂	107
6.1 Introduction	108
6.2 TCAD modelling for new material systems	108
6.3 Basic material parameters	110
6.4 Mobility model	112
6.4.1 Low carrier density	112
6.4.2 High vertical electric field	114
6.5 Application of the developed model	116
6.5.1 MoS ₂ -metal: contact barriers	116
6.5.2 MoS ₂ -oxide: interface traps	117
6.6 Conclusions	126
CHAPTER 7: THE LAYERED STRUCTURE CONCEPT	127
7.1 Introduction	128
7.2 Methodology development	131
7.3 Application of the developed model: back-gated MoS ₂	135

7.4	Methodology improvement.....	138
7.5	Junctionless and Inversion-Mode Transistors	140
7.6	Discussion.....	145
7.7	Conclusions	147
CHAPTER 8: CONCLUSIONS AND FUTURE PERSPECTIVES		149

This is to certify that the work I am submitting is my own and has not been submitted for another degree, either at University College Cork or elsewhere. All external references and sources are clearly acknowledged and identified within the contents. I have read and understood the regulations of University College Cork concerning plagiarism.

Gioele Mirabelli

To my family

Acknowledgements

I want to express my sincere gratitude to my supervisors Dr. Ray Duffy, Prof. Paul Hurley and Dr. Scott Monaghan. Their knowledge and experience truly helped during these years and greatly enriched my career both as a student and as a researcher. A special thank also to my Intel mentor, Mr. Roger Nagle, for his invaluable industrial insight along these years.

Besides my supervisors, I am also grateful to Prof. Ageeth Bol and Dr. Stefan Schulz for serving on my dissertation committee and for their insightful comments and questions.

My sincere thanks to Dr. Karim Cherkaoui, Dr. Farzan Gity, Dr. Enrico Caruso, Emmanuele Galluccio, and Dr. Lee Walsh for their scientific contributions, stimulating discussions and support over the past years.

I am also very grateful to Prof. Robert Wallace, Prof. Chadwin Young, Dr. Peng Zhao and Dr. Pavel Bolshakov for their warm welcome in University of Texas at Dallas. As well, I extend my thanks to Prof. Greg Hughes, Prof. Tony Cafolla, Dr. Conor McGeough, Prof. David McNeill, Dr. Prachi Budania, Dr. Conor P. Cullen, Dr. Cormac Ó Coileáin, Dr. Niall McEvoy and Prof. Georg Duesberg for a very fruitful collaboration.

I would like to thank Dr. Jennifer McKenna and Mr. Bernie Capraro for their invaluable encouragement to all the PhD students supported by Intel Ireland.

I convey my gratefulness to the many engineers, researchers and fellow students for the many discussions and support: Dr. Michael Schimdt, Dr. Brendan Sheehan, Mr. Dan O'Connell, Prof. Emanuele Pelucchi, Dr. Gediminas Juška, Prof.

Enrico Napolitani, Dr. Brenda Long, Dr. Nikolay Petkov, Ms. Emma Coleman, Mr. Fintan Meaney, Mr. Shane Garvey, Ms. Margarita Georgieva, Dr. Jun Lin, Dr. Carlos Marquez, and Dr. Shubhadeep Bhattacharjee.

Finally, I also thank my father Emanuele, my mother Debora, my sister Ersilia, my brother-in-law James, my nieces Giulia and Chole and my grandfather Sebastiano for their never-ending support, encouragement and prayers.

Without each and every one of you this would not have been possible.

ABSTRACT

The aggressive scaling imposed by CMOS technology has put very stringent requirements on the dimensions of Silicon transistors. According to the semiconductor roadmaps (ITRS, IRDS, Nereid), the dimensions of the device might have reached its limits in terms of gate length. Although new device architectures are being studied to keep the pace up with Moore-law, new material systems are still relevant to further improve the performance of integrated circuits. On this regard, 2D-semiconductors, as transition metal dichalcogenides (TMDs), are being considered as potential replacement for Silicon. Because of their intrinsic thin nature, they can guarantee a better channel control at similar channel length, without suffering from high mobility degradation as other 3D-semiconductors.

In this dissertation, the limits and potentials of 2D-semiconductors are investigated by material analysis, electrical characterization and TCAD modeling.

First, the air sensitivity of few TMDs is considered. An initial AFM study show high reactivity in HfSe₂, with blisters growing up to 60 nm after one day from ambient exposure. These results are later confirmed by other techniques, showing a high detrimental effect on the semiconductor surface. The surface treatment or protection of these materials needs to be carefully studied for their use in the semiconductor industry.

A second limitation of 2D-electron devices is their low mobility compared with theoretical studies. Material and electrical characterizations of 3-layers MoS₂ transistors show a high impurity concentration, which drastically limits the field-effect

mobility and so device performance. Mobility could be improved carefully selecting a proper dielectric environment, which plays an important role in the current transport in thin semiconductors.

However, the major limitation of 2D-based electronics is related to a poor metal-TMD interface, often characterized by high Schottky barriers and Fermi-level pinning. Taking as example modern semiconductor technologies, highly doped MoS₂ devices are carefully studied. The contact resistance extracted is lower with respect of undoped or untreated samples, and close to the requirements imposed by the semiconductor roadmaps. Another solution might rely on the annealing of the metal-TMD interface in order to create a 3D-alloy, which might be optimal in terms of contact resistance.

The final part is related to the development of a TCAD model for 2D-semiconductors. At first, the model parameters were carefully tuned against theoretical and experimental results. Then, a TCAD software was used for a deeper understanding of experimental devices, regarding the metal-TMD and oxide-TMD interface. Later, the same model was improved considering a layered-structure, taking into consideration the semiconductive layers as well as the Van-der-Waals gaps in between them.

Chapter 1: INTRODUCTION

1.1 BACKGROUND AND MOTIVATION

The modern electronics technology has its roots in 1947, when the first working transistor was experimentally proven and for which John Bardeen and Walter Brattain together with William Shockley received the Nobel Prize in Physics for their discovery of the transistor effect.¹ Even if revolutionary, another step needed was the integration of more components onto the same chips. The idea of Jack Kilby at Texas Instruments in 1958 was to make all the components and the chip out of the same block of semiconductor material, developing the first integrated circuit. In this way there were no need of discrete components, the process could be automated, and it would allow a much higher performance.

The evolution of electronics technology of those years can be summarized by “Moore’s law”.² Gordon Moore predicted that the numbers of transistors that can be installed on an integrated circuit could be doubled every two years. This can be achieved by shrinking down all the dimensions of the device. In 1974 Dennard et al.³ showed the benefits of scaling. This is based on the assumption that the electric field inside the transistor is kept constant. Considering a scaling factor α , switching speed increases by a factor α , power dissipation is reduced by a factor α^2 and the power-delay product by a factor α^3 . This scaling law implies a reduction in the supply voltage and threshold voltage by a factor α .

A clear image of this is reported in Figure 1,⁴ where each year the dimension of the single device decreases, allowing a higher density and an always better performance in terms of circuit speed and power dissipation.

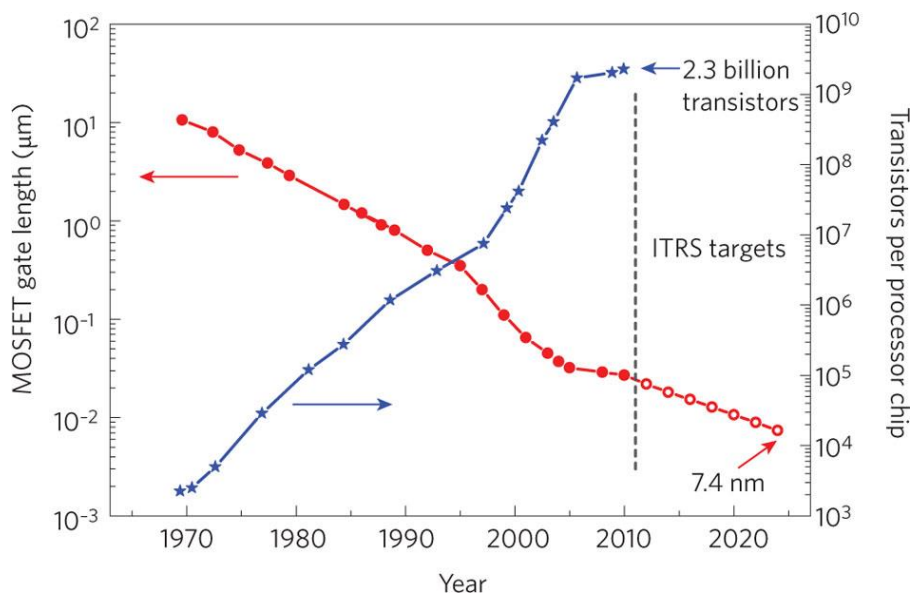


Figure 1: Trend of gate length and number of transistors per processor chip per year.⁴

As a consequence of this trend, the miniaturization of circuits by scaling down transistor's dimensions has been a central topic for the last 60 years and Dennard's scaling law was followed by semiconductor industry until 2005 approximately.

The aggressive scaling of devices brought new kind of problems known as "short-channel effects" (SCE), which arise when distance between source and drain regions become very small. Considering a classic MOSFET (Metal-Oxide-Semiconductor Field Effect Transistor) architecture, the source and drain junctions create depletion regions which make the actual channel length shorter. The electric fields that penetrate the channel regions make the control of the gate on the channel less effective, because the channel potential doesn't depend on the gate voltage only, but they are also dependent on the voltages applied on source and drain.⁵ A visual example is shown in Figure 2, where the drain-junction depletion regions increases for higher drain voltages.

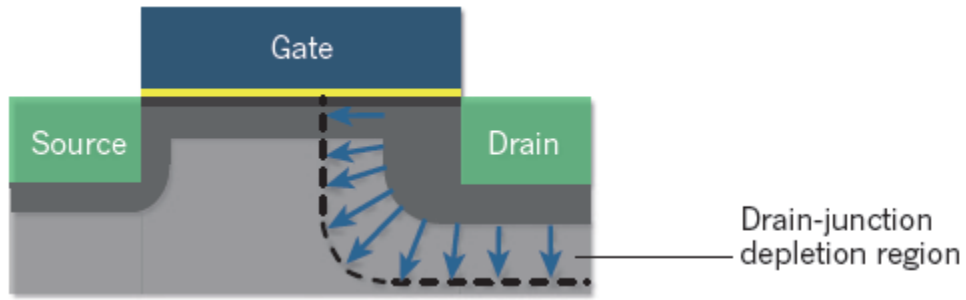


Figure 2: example of drain-junction depletion region, responsible for short-channel effects.⁵

In order to mitigate SCE, the research community is actively looking for promising materials to replace Silicon in the future. Among all of them III-V semiconductors, Germanium and 2D materials are the most studied. In particular this last class of semiconductors are gaining much interest in the recent years. Their general characteristics, potential and major limitations will be discussed in the following paragraphs.

A second issue in modern technology is related to power consumption. Figure 3 shows the two components of power consumption in MOSFET technology versus gate length: active and subthreshold power density. The former is related to the operation frequency of the device:

$$P_{Act} = CV_{DD}^2 f \quad (1)$$

where P_{Act} is the active power consumption, C is the load capacitance, V_{DD} is the supply voltage and f is the operation frequency.

The latter, subthreshold power consumption, depends on the OFF current, I_{OFF} :

$$P_{Sub} = V_{DD} I_{OFF} \quad (2)$$

Although the active power consumption can be reduced with a scaling of V_{DD} , this will in turn affect I_{ON} and so device performances. That is why beyond the 100 nm technology node the improvement of device performance departed from dimensional scaling alone,⁶ and an increase in the drive current was supplemented by boosting mobility with uniaxial strain,⁷ high-k oxides⁸ and novel architectures.⁹ It is also clear from Figure 3 that below 20-nm gate length the subthreshold power density is higher than the active power density.¹⁰ For this reason materials or architectures capable of achieving a lower I_{OFF} are necessary to optimize power consumption.

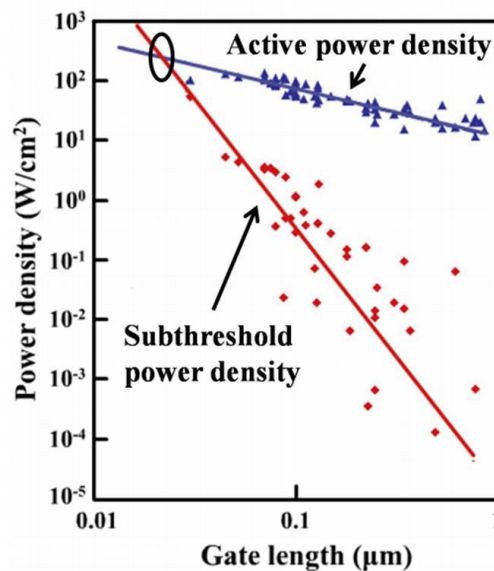


Figure 3: Active and subthreshold power densities for Si MOSFETs with respect of gate length. The cross-over point at 20-nm gate length indicates where subthreshold power density surpasses active power density.¹⁰

1.2 2D-MATERIALS PROPERTIES AND APPLICATIONS

1.2.1 Crystal structure

The interest in 2-Dimensional materials started after the successful experimental demonstration of graphene in 2004, one atomic layer of carbon atoms.¹¹

These carbon layers are held together by weak Van-der Waals forces, which allows the isolation of thin flakes by mechanical exfoliation. Graphene has interesting characteristics, such as high mechanical strength, thermal and electrical conductivity, which makes it an interesting material for next-generation interconnects.¹² Nevertheless, graphene is characterized by a zero bandgap, and a bandgap is essential for logic based electron device applications. Several 2D materials have been studied by the research community since the discovery of graphene, and the class of materials called Transition-Metal Dichalcogenides (TMDs) have been the subject of particular research attention. These are semiconductors in the form of MX_2 , where M is a transition metal (Mo, W, Hf), and X is a chalcogen (S, Se, Te). Each TMD layer is composed by a layer of metal atoms “sandwiched” between the chalcogen atoms and the interlayer distance is ~ 0.65 nm, as schematically shown in Figure 4a.¹³ The metal and chalcogen atoms are covalently bonded together, while each layer is held together by weak Van-Der-Waals forces. Figure 4b shows a high-resolution Cross-Section TEM of MoTe_2 to highlight the layered structure of the material system. The atom configuration of Figure 4a was overlapped in some regions in order to help the eye distinguishing each semiconductive layer. The weak Van-Der-Waals forces between each monolayer of which they are formed, allow thin multilayers to be easily exfoliated by a scotch tape technique from their bulk form, as was first shown for graphene. Although a large area growth technique will be needed to integrate them with the modern technologies, the mechanical exfoliation offers a fast and reliable route to characterize the material properties.

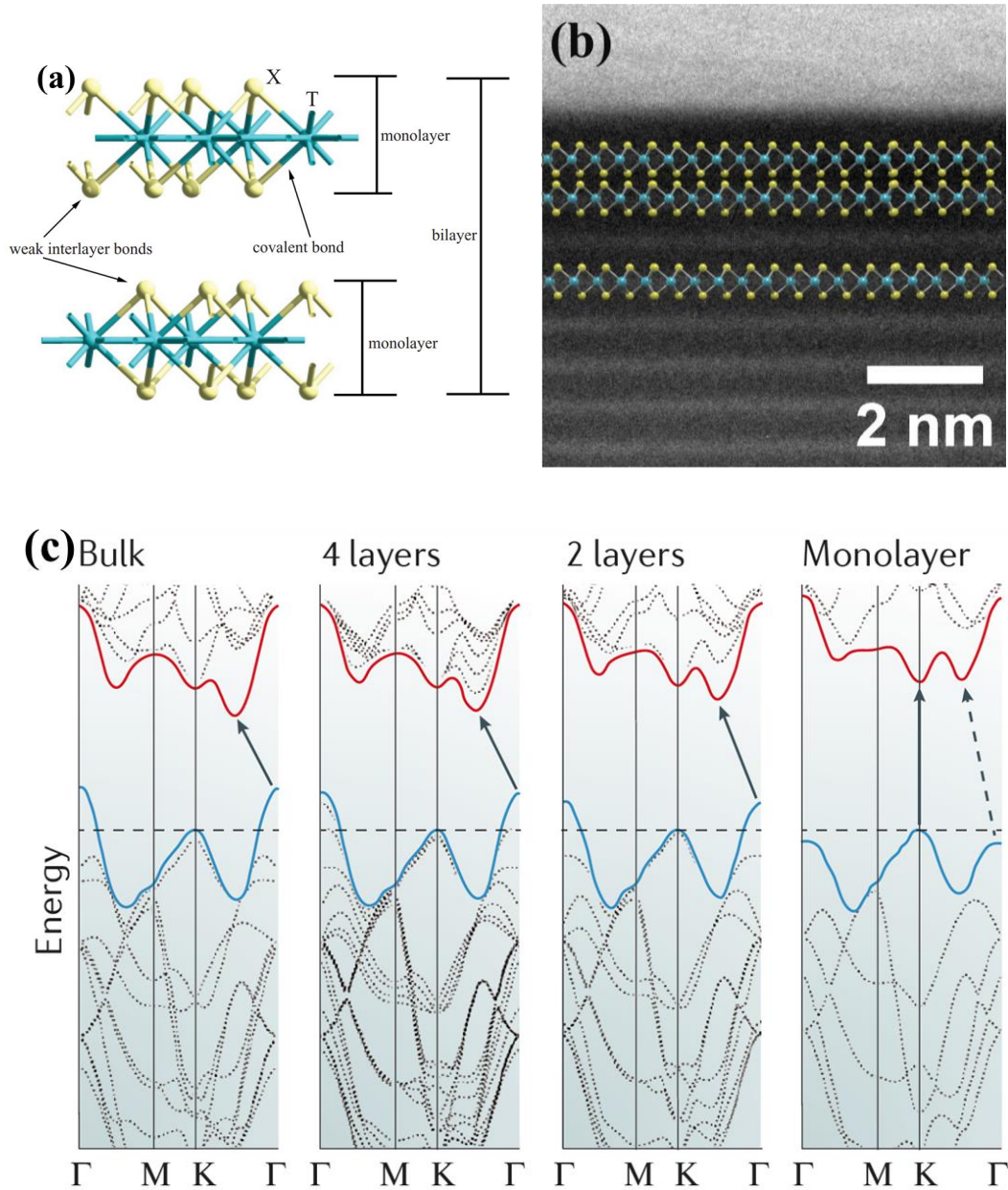


Figure 4: (a) Typical crystal structure of a TMD.¹³ (b) Transmission electron microscopy cross section of a MoTe₂ exfoliated flake. Superimposed the crystal structure to emphasize the layered nature of these materials. (c) Bandgap evolution with respect of number of layers of MoS₂, from monolayer to bulk.¹⁷

As said, TMDs show a finite direct bandgap from few meV to ~2 eV, predicted by density-functional-theory (DFT) calculations,¹⁴ which makes them suitable for logic devices.^{15, 16} Figure 4c show the bandgap variation with respect of number of layers for MoS₂. The gap of bulk MoS₂ is ~1.2 eV and it increases to ~1.9 eV in its

monolayer form. Interestingly, bulk MoS₂ is an indirect bandgap semiconductor, while it becomes direct at the monolayer. As shown in Figure 4c, the bandgap properties of MoS₂ with respect of number of layers depend on the transition of the top of the valence band from the Γ to the K point, while the minimum of the conduction band shifts from halfway between Γ and K to the K point.¹⁷ It is important to notice that this point is not a high symmetry point of the Brillouin zone, and its exact position depends on thickness and Metal/Chalcogen.¹⁸ These two valley have been shown to be important for to understand the velocity saturation in monolayer MoS₂.¹⁹

Table 1: comparison of Nb, Ta,²⁰⁻²² Mo and W^{13, 22-26} TMDs considering their electronic characteristics. Table adapted from ²⁷.			
	-S₂	-Se₂	-Te₂
	Electronic characteristics	Electronic characteristics	Electronic characteristics
Nb	Metal; Superconducting; Charge density wave;	Metal; Superconducting; Charge density wave;	Metal
Ta	Metal; Superconducting; Charge density wave;	Metal; Superconducting; Charge density wave;	Metal
Mo	Semiconducting 1L: 1.8 eV Bulk: 1.2 eV	Semiconducting 1L: 1.5 eV Bulk: 1.1 eV	Semiconducting 1L: 1.1 eV Bulk: 1.0 eV
W	Semiconducting 1L: 2.1 eV Bulk: 1.4 eV	Semiconducting 1L: 1.7 eV Bulk: 1.2 eV	Semiconducting 1L: 1.1 eV

In addition, TMDs exist in other phases as well. The 2H is the most common semiconducting phase, but interesting properties were also found in the metallic 1T-phase.²⁸ As will be detailed later in chapter 3 and 5, the opportune modulation of the

material below the contact region can open up new ways in order to drastically reduce contact resistance in 2D-Field Effect Transistors (2D-FETs). Due to the high number of possible combinations between transition metal and chalcogenides, TMDs show a wide range of electrical properties as summarized in Table 1, where four different chalcogens, namely Nb, Ta, Mo and W are compared. Considering a variation of the transition metal or the chalcogen the properties of the material can change drastically, from semiconducting to superconducting, which makes TMDs generally suitable for a wide range of applications.

1.2.2 Growth of TMDs

As briefly said in the last section, most studies on the electrical or optical behaviour and material properties of TMDs have been based on mechanically exfoliated flakes. In these works, TMDs are exfoliated by scotch tape technique from their bulk counterpart, grown by chemical vapour transport at high temperature.^{29, 30} It is relatively easy to isolate few or single layers of material, and the flakes so obtained are surely a fast and easy way to study the material. However, the process is not scalable, and therefore not compatible with the modern nano-electronic industry. Therefore, many research groups showed interest in looking for the optimal growth technique and condition of TMDs in the recent years. The most common techniques used to grow TMD films is probably chemical vapour deposition (CVD), although there are also examples of atomic layer deposition (ALD) or molecular beam epitaxy (MBE) grown materials.³¹⁻³⁴

In CVD, a film of metal oxide (e.g.: MoO_3) is in close proximity or deposited directly to the desired substrate. The desired chalcogen is then heated and flows in vapour phase in the same chamber. It then reacts with the pre-deposited (or adjacent)

film at relatively high temperature, usually around 800 °C.³⁵⁻³⁷ The growth is not homogenous, and it is characterized mainly by “triangular” grains that merge together after sufficient growth time.³⁸ The thermal budget of these processes is usually high to obtain a reaction of the chalcogen with the metal oxide. However, high performance devices were reported by this method, where MoS₂ was deposited on Al₂O₃.³⁹

Conversely, ALD allow the deposition of TMDs at relatively lower temperatures between 100 and 475 °C.⁴⁰⁻⁴⁵ An example is the work of Tan et al.,⁴² where a high control over the MoS₂ thickness was achieved. Nonetheless, a high temperature annealing of 800 °C was necessary to grow large size crystals of ~2 μm. Similarly, Jurca et al.⁴⁶ studied the ALD deposition of MoS₂ varying temperature and pulse time. The temperatures used are very low, between 60 and 120 °C. Although a uniform deposition was achieved the grain size is extremely small, and it is improved only by annealing for 5h at 1000 °C. This is extremely detrimental for TMD-based FET, as mobility is highly dependent on the grain size.

An alternative technique is thermal assisted conversion (TAC), by which a metal initially deposited on the desired substrate is converted into a TMD through high temperature annealing in a chalcogen atmosphere. This method has previously been used for MoS₂, and both a high temperature (750 °C) and a thin initial film thickness were necessary to obtain a complete conversion and a uniform film coverage.^{47, 48} This process can also be used for the growth of PtSe₂,⁴⁹ a TMD which interest increased in the last few years. In contrast to other TMDs, the synthesis by TAC of PtSe₂ does not require a high thermal budget⁵⁰ (temperature is ~400 °C) which it makes growth compatible with back-end-of-line processing.⁵¹⁻⁵³

Molecular beam epitaxy is another technique that has become more common in the last years. With respect of CVD, it requires typically lower temperature, offers a greater control of film thickness,³⁴ as well as the possibility to incorporate dopants⁵⁴ or to grow high quality heterostructures.⁵⁵ Recently, Yue et al.⁵⁶ studied the deposition of WSe₂ by MBE, considering the effect of the metal flux, chalcogen flux and temperature in order to achieve higher grain sizes. Although promising and improved with respect of similar works, the results are far from satisfying the large area growth required by the CMOS industry.

A proper compromise of the temperature growth with the requirements of the preferred application is certainly required for the usage of TMDs in future electronics and optoelectronics applications. In order to respect the stringent temperature requirements of the CMOS industry and still obtaining high crystal quality, Huyghebaert et al.⁵⁷ proposed the high temperature growth of WS₂ and its transfer to the target substrate, since several methods wafer scale quality growth of TMDs have been reported.⁵⁸ With this process a temporary adhesive/laser release layer is spun on the glass wafer and bonded to the WSe₂ layer. The WS₂ is then peeled off from the initial substrate and transferred to the preferred substrate. The temporary stack is then released by laser. The transfer process can influence the electrical properties of 2D-materials, because of local strain, cracks and wrinkles,⁵⁹ but the use of a 300 mm grown material allow the use of wafer handling methods, with higher control and precision.

1.2.3 Optoelectronic applications

These characteristics open a wide range of possible applications for TMDs in optoelectronics and photonic applications, as photo-detectors, emitters, single-photon

emitters and valleytronics.^{60, 61}

Due to the enhanced absorption observed in MoS₂ photovoltaic applications are of particular interest. This research area is not recent and started in 1982, when Fortin and Sears reported the photovoltaic effect in bulk MoS₂ with efficiency of 1%.⁶² More recent results showed an efficiency of 4.5% of 12.5 nm of MoS₂ on p-type Silicon.⁶³ Similar results were obtained considering heterojunction of MoS₂ on Si or GaAs, which yielded 5.23% and 4.82% respectively.^{64, 65} These results might be further improved considering that the MoS₂ was transferred after growth with a sacrificial PMMA layer, where residues might affect the device efficiency. In addition further improvement can be achieved by considering a h-BN interlayer, electrical gating or chemical doping or with graphene quantum dots.^{65, 66} The change of bandgap with respect of number of layers, or through heterostructures of different TMDs, might be particularly suitable for photovoltaic applications.⁶⁷ In particular, using materials with different bandgaps in a singular multijunction solar cell, would allow photons of different energies to be absorbed, reducing losses due to thermalization.⁶⁸

In addition, several reports have shown photodetection using a wide range of TMDs. Considering MoS₂, phototransistors were fabricated with mono- or few-layers of material, exfoliated or grown by chemical vapour deposition, with photoresponses ranging from 7.5 mA/W to 800 A/W.⁶⁹⁻⁷¹ However, similar results were also obtained considering MoSe₂,^{35, 72, 73} WS₂^{74, 75} and WSe₂.⁷⁶ The photodetection sensitivity in specific wavelength ranges can also be tuned considering different thicknesses, as mono- and bi-layer MoS₂ showed greater green light sensitivity, while tri-layers showed an improved sensitivity to red light.⁷⁷ Interestingly, some reports showed photodetectors based on heterostructure using MoS₂ and WS₂.

1.2.4 Electronic applications

TMDs have been shown to be a possible solution for high performance electronic devices. Due to their properties and 2D-nature TMDs can be very useful for Tunnel-FET (TFET). With respect to classic MOSFET, TFET can show subthreshold swing below the classic 60 mV/dec, which is very important for low-power devices, as portable electronics and sensors in the future. The working principle between the two architectures is different.⁷⁸ As depicted schematically in Figure 5a, n-type MOSFET devices can be switched on when the gate voltage applied lowers enough the barrier between the source and drain region for electron transport from source to drain in the semiconductor conduction band. On the contrary, for a n-channel TFET carriers originate from the valence band in the source. The gate voltage applied lowers the conduction band of the channel region, so it overlaps with the valence band of the source region, allowing tunneling of carriers.

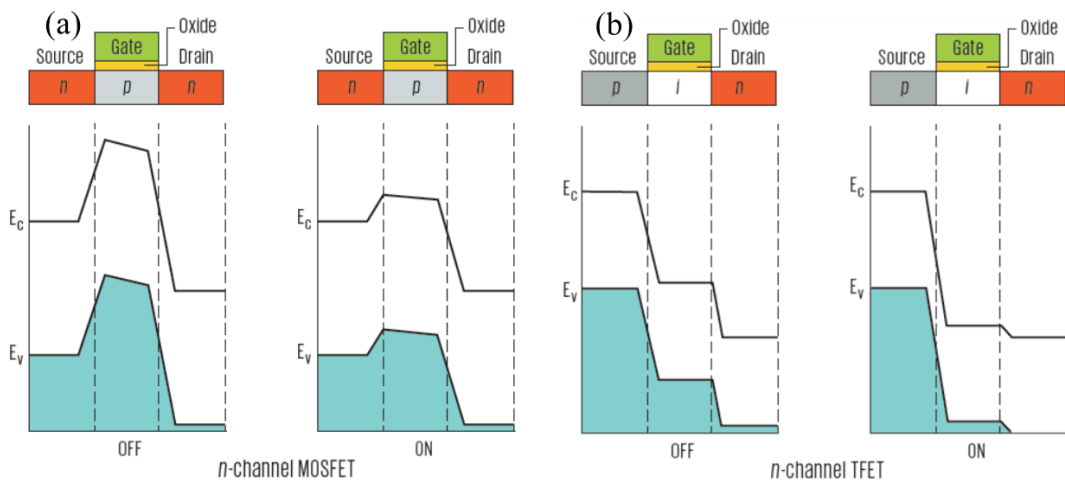


Figure 5: Comparison of band diagrams of (a) a n-channel MOSFET and (b) a n-channel TFET during off and on operation, showing the main difference between their working principle. The terms E_c and E_v refer to the minimum energy of the conduction band and maximum energy of the valence band, respectively. Adapted from ⁷⁸

The difference in bandgap and electron affinity among different TMDs can be exploited in order to properly align the conduction and valence band of the source and drain regions, which can be made out of two different materials.^{79, 80} Since both materials are layered, the interface can in principle be free of defect states or dangling bonds, which can cause inelastic trap-assisted tunneling in the OFF-state and degrade the device behavior.⁸¹⁻⁸³

On this topic, Li et al.⁸⁴ explored by theoretical simulations the band alignment of vertically stacked WSe₂ and SnSe₂. It was reported a subthreshold swing of ~14 mV/dec for both p- and n-TFET at a V_{DS} of 0.4V, with higher energy efficiency with respect of other architectures. A similar architecture was fabricated by Sarkar et al.⁸⁵ using p-type Germanium and bi-layer MoS₂. Although the desired I_{ON} performances were not achieved, a steep subthreshold slope of ~31.1 mV/dec was obtained for almost 4 orders of magnitude.

1.2.5 Comparison and advantages of TMDs for electronics applications

Although promising, the study and experimental reports of TFET based on 2D-semiconductors is still at an early stage. In order to compare the characteristics of 2D-materials with other semiconductors it is possible to consider a MOSFET architecture, which has been extensively used as a benchmark architecture to analyze and study the properties of these materials. On this regard, it is important to consider that the NanoElectronics Roadmap for Europe (NEREID) states that a fully depleted Silicon On Insulator (SOI) node “can be a long lasting technology with differentiated options (RF, mixed signal, ultra-low power, embedded memories, sensors...)”.⁸⁶ MOSFET based on TMDs can be considered as a close analogy to fully-depleted SOI due to their intrinsically thin nature. Therefore, the study and optimization of this architecture is

still of interest. To do so, it is possible to study the behavior with respect to SCEs. As will be clarified in this section, the minimization of SCEs depends on several different properties.

To quantify the effectiveness against SCEs it is possible to consider the natural length λ , which represents the electric field lines of source and drain region in the channel. In a single gate MOSFET, as evaluated by Yan et al.⁸⁷:

$$\lambda = \sqrt{\frac{\epsilon_{Ch}}{\epsilon_{ox}} t_{Ch} t_{ox}} \quad (3)$$

Where ϵ_{Ch} is the electrical permittivity of the channel material, ϵ_{ox} is the electrical permittivity of the oxide, t_{Ch} is the channel thickness and t_{ox} is the oxide thickness.

Generally, to produce a good subthreshold behavior the natural length should be 5-10 times lower than the effective channel length. Since a short channel length is desired to keep up with Moore's law, the natural length should decrease too in order to guarantee a good device behavior. From Equation 3, λ is proportional to both the thickness of the oxide and the thickness of the channel. As known a thinner oxide guarantees a better capacitive coupling of the gate, but the channel thickness impacts the natural length just as much. Even if Equation 3 was derived for fully depleted SOI and does not strictly apply to 2D materials,⁸⁸ a thinner channel can be more effective against SCE. This is true for every semiconductor device, but the electrical properties of 3D-semiconductors degrade significantly when thinned down to the 5-10 nm scale.

To appreciate the difference between different materials when the thickness is scaled, as initial step it is possible to consider the semiconductor carrier mobility. DFT calculations for monolayer MoS₂ showed an upper limit of 400 cm²/V.s.⁸⁹

Experimental results show usually much lower values because of the presence of impurity, defects and contact resistance.⁹⁰⁻⁹² The mobility of 3D-semiconductors instead scales between t_{ch}^6 and t_{ch}^4 due to surface roughness and phonon scattering.^{93, 94} High-mobility materials, such as III-V, can easily exceeds 10^4 cm²/V.s. However these values degrade drastically at low thicknesses.⁹⁵⁻⁹⁷ As well, Silicon films showed a high resistivity approaching small dimensions (1-5 nm).^{98, 99} The situation is depicted schematically in Figure 6a.¹⁰⁰ The mobility of TMDs is lower with respect of graphene or classic 3D-semiconductors, yet they keep a reasonable mobility at low thicknesses.

High mobility values are a consequence of low effective masses. The comparison is depicted in Figure 6b. Since the effective mass is inversely proportional to mobility, the trend is opposite with respect of Figure 6a. For aggressive scaled devices (sub-5 nm scaling), the distance between source and drain region is short enough that quantum-mechanical source-drain tunneling can significantly degrade the subthreshold swing and increase I_{OFF} (indirectly it reduces I_{ON} as well, as gate work-functions are chosen to match a certain I_{OFF}). For this reason, the physical gate length predicted by the ITRS roadmap in 2015 reached a plateau value of 10 nm from 2021 onwards. The newer IRDS roadmap in 2017 predicted instead an even larger value, from 16 to 12 nm from 2021 to 2030.¹⁰¹ Therefore, materials with lower mobility but higher effective mass might become preferable.^{89, 102, 103} 2D-semiconductors are in general characterized by a higher effective mass (Figure 6b), making them more immune to SCEs. It is also important to consider that both mobility and effective mass values might still be optimized by strain engineering,^{104, 105} which might be another method to tune the properties of 2D-semiconductors.

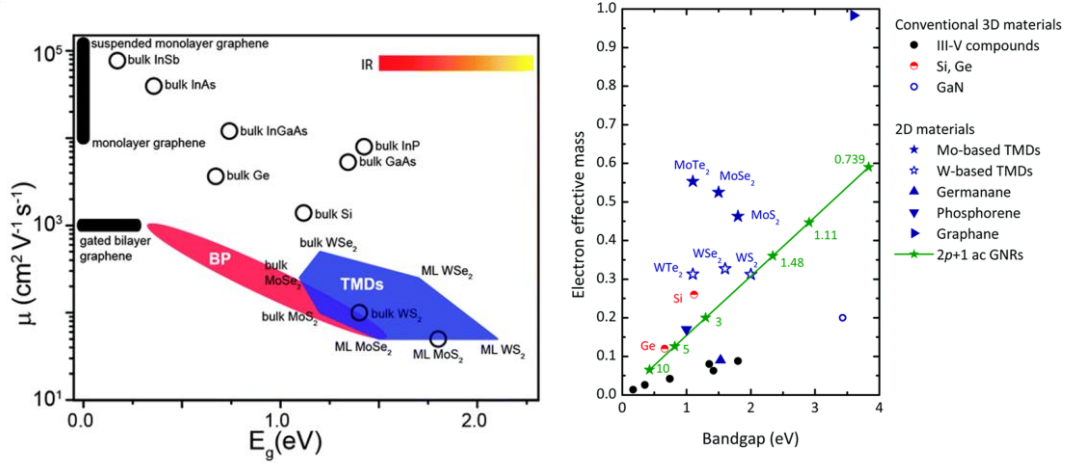


Figure 6: (a) Plot of mobilities versus band gap for TMDs, Si, Ge and III-Vs. The color scale represents the energy range of visible and infrared light with respect to the band gap energy.¹⁰⁰ (b) Electron effective mass versus bandgap. III-V data are InSb, InAs, In_{0.53}Ga_{0.47}As, InP, GaAs, Al_{0.3}Ga_{0.7}As from left to right.⁸⁸

It is also important to consider that effective mass is directly related to the effective conduction band density of states (DOS). III-V materials for example, are characterized by a low effective mass and so low density of states in the conduction band. This problem is commonly known as “DOS bottleneck”, where a large gate voltage is necessary to swing the Fermi enough to strongly invert the III-V surface.¹⁰⁶ For the sake of comparison, the effective DOS for the conduction band of GaAs is 4.7×10^{17} , while it is 3.2×10^{19} for Silicon and in the order of 10^{20} for monolayer MoS₂.^{107, 108}

In addition, following again Equation 3, λ is also directly proportional to the dielectric constant of the semiconductor, ϵ_{ch} . The dielectric constant of TMDs ($\sim 3-6$) is generally lower than the one of Silicon (~ 12), Germanium (~ 16) or III-V materials ($\sim 9-16$). Therefore, for the same oxide or channel thickness, the immunity to SCE is higher.

An advantage that holds for both the MOSFET and the TFET architecture is

related to the interface of the material. As briefly introduced in the previous section, the lack of dangling bonds allows a more performant TFET. However, in addition to that, for both architectures, a semiconductor-oxide interface is also necessary. For this same reason the interface between an oxide and a 2D-semiconductor is theoretically perfect, allowing for low density of interface traps and so better performances in terms of subthreshold swing, mobility and reliability.

1.3 CHALLENGES OF 2D-MATERIALS

1.3.1 Defects and impurities

The performances of any FET device are highly dependent on the quality of the channel material as defects and impurities can drastically change its electrical behaviour. Considering Silicon as example, unintentional impurities are controlled to be less than $5 \times 10^{10} \text{ cm}^{-2}$, and structural defects below 0.008 cm^{-2} .¹⁰⁹ This is necessary in order to maintain a good mobility and avoid variability between different devices. Several reports using different techniques have shown a high concentration of defects and impurities on different TMDs.

Studies on the surface of natural and synthetic exfoliated MoS₂ by scanning tunnelling microscopy (STM) showed a high concentration of defects present on the surface, attributed to Sulphur vacancies.^{90, 110} Some point defects instead pointed to a high concentration of impurities. An inductively-coupled plasma mass spectroscopy analysis carried out on the same crystals showed that a concentration greater than 10^{13} cm^{-2} , way higher with respect of what is required in the Si-based integrated circuit industry. The high presence of impurities is extremely detrimental for the carrier mobility of these materials. Several theoretical calculations have shown how the effect of impurity concentration impacts the carrier mobility in 2D semiconductors.^{92, 111, 112}

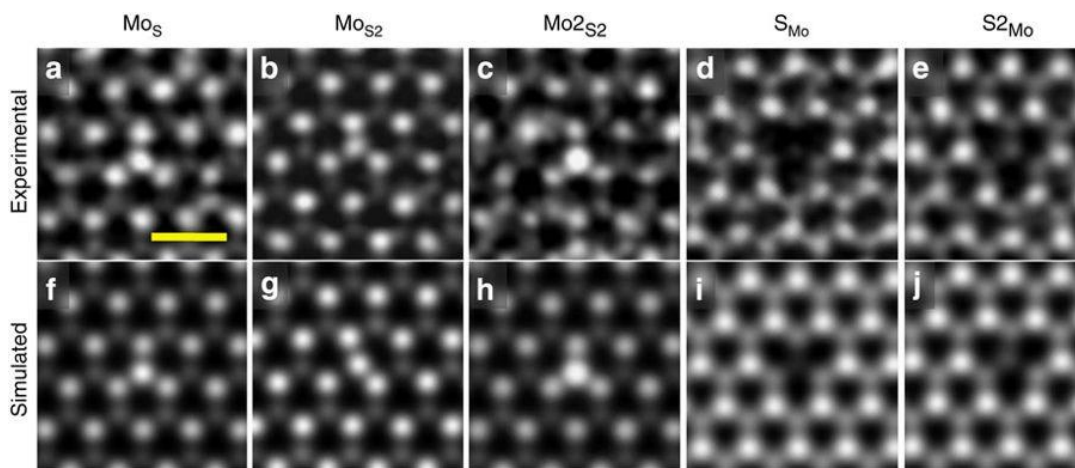


Figure 7: Atomically resolved annular dark-field scanning transmission electron microscopy of defects in MoS₂: (a) Mo replacing (a) one or (b) two S atoms, (c) two Mo atoms replacing two S atoms, (d) one and (e) double S vacancy. Scale bar is 0.5 nm. ¹¹³

Another systematic study was performed by Hong et al.¹¹³ by electron microscopy. The monolayer MoS₂ mechanically exfoliated showed several different defects: sulphur vacancy, double sulphur vacancy, Mo vacancy, one S atom replacing Mo site, shown in Figure 7. Statistically, the sulphur vacancy (SV) is the most common defect in exfoliated MoS₂, with a concentration up to $3.5 \times 10^{13} \text{ cm}^{-2}$.

In addition, Qiu et al.¹¹⁴ combined an electron microscopy study of monolayer MoS₂, confirming a SV concentration of $\sim 10^{13} \text{ cm}^{-2}$, with density functional theory (DFT) calculations and electrical transport. The electrical transport of monolayer MoS₂ was explained by hopping transport through defects. In agreement, DFT calculations have shown that sulphur vacancies are characterised by energy levels that lie in the bandgap of MoS₂, 0.2-0.3 eV below the conduction band. In particular, theoretical works predicted that a sulphur vacancy is occupied by two electrons in its neutral state, which correspond to the valence of the missing sulphur atom.¹¹⁵⁻¹¹⁷

It is also important to state that few layers of MoS₂ are much more affected by defects with respect of thicker samples.^{118, 119} Figure 8a and 8b show the transfer

characteristic of multi- and mono-layer MoS₂ at different temperatures. For temperatures below 100 K the signature of defects is much clearer and it causes “jumps” of the transfer characteristic in the subthreshold region. Figure 8c shows a schematic of multilayer MoS₂ on SiO₂ to explain the difference related to the thickness of the two devices. Both devices are characterized by a high presence of defects, but in the multilayer case, adjacent layers can screen the defects. On the contrary this can't happen in monolayer devices. It is not certain if the defects are localised inside the MoS₂ or at the MoS₂/SiO₂ interface, but the sensitivity of thinner devices to defects is clear.

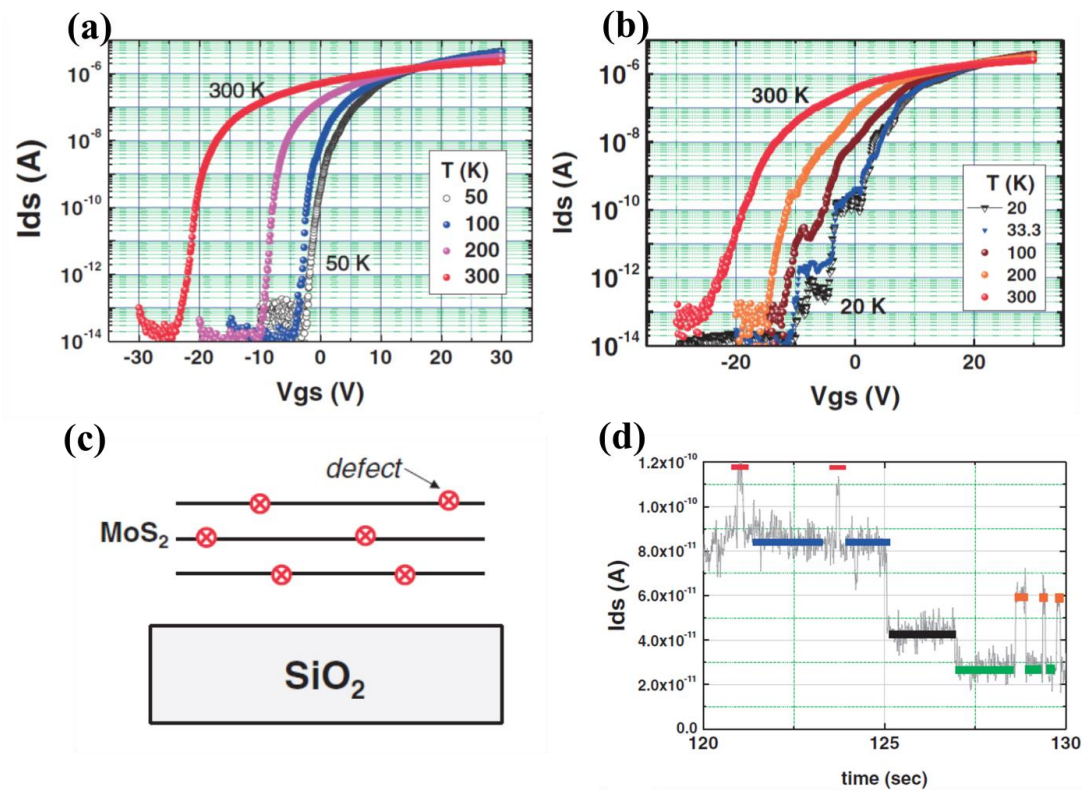


Figure 8: Subthreshold characteristics of (a) multilayer and (b) monolayer MoS₂ at different temperature. The monolayer device clearly shows the presence of active defects, on the contrary of the multilayer device (c) Schematic illustration of the multilayer device to show the difference between the multi- and mono-layer device, as in a multilayer device a defect can be screened by carrier in the adjacent layers. (d) Example of temporal characteristic of monolayer MoS₂ at 20K showing several current levels. ¹¹⁸

The high presence of these defects can also be responsible for the Fermi-Level Pinning usually present in MoS₂, and for the contact behaviour in general, but this will be further discussed in the next section. The presence of impurities and defects as well as their impact on the electrical behaviour of MoS₂ are going to be studied in Chapter 4 and 6.

1.3.2 Metal-TMD interface: Schottky barrier and Fermi-level Pinning effect

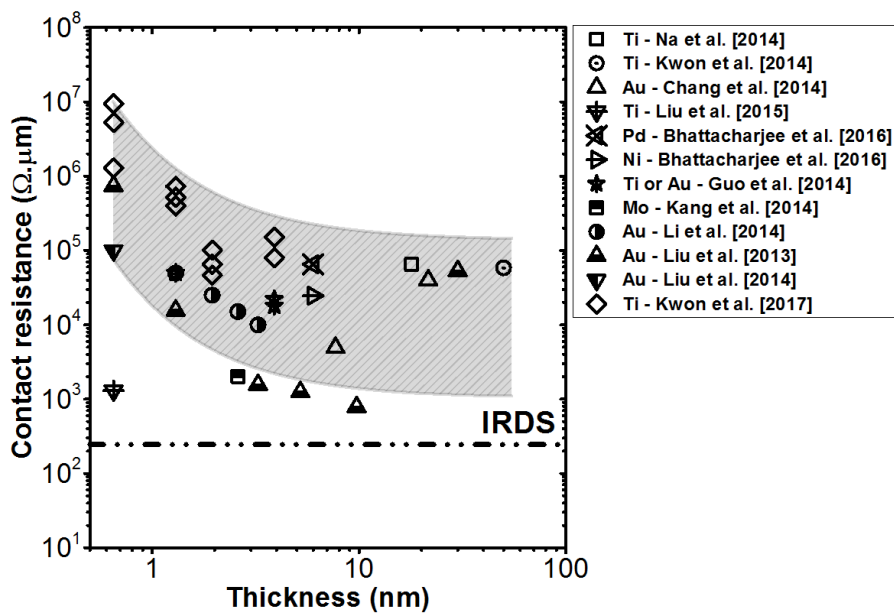


Figure 9: Summary of contact resistance values found in literature considering as-exfoliated devices. The gray area shows the general trend of contact resistance, characterized by high variability and excessive high values.

A low contact resistance is of great importance for scaled semiconductor devices and this is of particular interest for 2D semiconductors.¹²⁰ It is one of the most studied subject on TMDs and the issues has been treated from a material, electrical and theoretical perspective. Indeed, a reliable process to obtain an ohmic contact with TMDs is still missing and most of the time the contact is characterized by high Schottky barriers. For a clearer idea, Figure 9 shows a trend of contact resistance versus MoS₂ thickness considering several reports.¹²¹⁻¹³¹ The dashed line represents

the goal set by the IRDS roadmap for 2027.¹⁰¹ These data are in fair agreement with each other. The contact resistance decreases from $\sim 3 \times 10^6 \Omega \cdot \mu\text{m}$ for monolayer MoS_2 , to $\sim 6 \times 10^4 \Omega \cdot \mu\text{m}$ for thick samples. In addition, these data consider both low and high work-function metals, but there is not any trend considering a variation of the metal contact.

To explain the behavior of the MoS_2 -metal contact, Figure 10a show the band-diagram of a metal-semiconductor interface before contact. ϕ_M and ϕ_S are the metal and semiconductor work functions respectively, while $q\chi$ is the semiconductor electron affinity. When the two materials come in contact an electrical current flows across the interface.¹³² Due to the migration of electrons from the semiconductor to the metal a depletion region creates at the interface and a potential barrier is formed (Figure 10b).

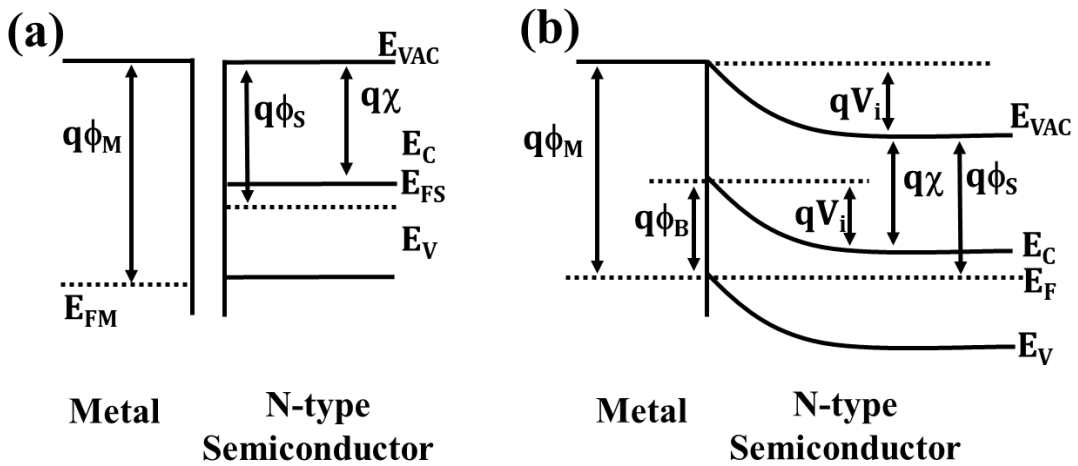


Figure 10: Schematic of the energy band diagram of metal and n-type semiconductor (a) before and (b) after making contact.

On the semiconductor side, the potential barrier formed is given by the difference of the metal work function and semiconductor work function:

$$qV_i = q\phi_M - q\phi_S \quad (4)$$

On the metal side, the built-in potential barrier formed is known as Schottky barrier height (SBH) and it is given by:

$$q\phi_B = q\phi_M - q\chi \quad (5)$$

This barrier leads to a rectifying behavior as the current flows only from one side to the other. When a positive voltage bias is applied to the metal the potential barrier is reduced for the electrons in semiconductor but not for the electrons in metal, thus increasing the electron current flow from the semiconductor to the metal. When a negative voltage is applied the potential barrier is reduced, decreasing the current flow from semiconductor to the metal. The SBH does not change in both cases. The electron current flow from the metal to the semiconductor remains unchanged leading to a rectifying non-linear current–voltage behavior.¹³³ Similar behavior applies to p-type semiconductors, where holes are the majority carriers.¹³⁴

An additional problem is related to the Fermi-level pinning at the metal contact. A study by Das et. al.¹³⁵ showed that the Schottky barriers between metals and MoS₂ are not consistent with the energy difference between the metal work function and the TMD Fermi level. They showed that even metals which would be expected to act as p-type contacts (i.e. Ni and Pt) instead exhibited electron injection consistent with n-type contacts. Due to this effect the SBH is independent on the metal work function, and it is dependent on the Schottky pinning factor S:

$$q\phi_B = S(q\phi_M - q\phi_{CNL}) + (q\phi_{CNL} - q\chi) \quad (6)$$

Where ϕ_{CNL} is the charge neutrality level with respect of the vacuum level and S is equal to:

$$S = \frac{d\phi_B}{d\phi_M} \quad (7)$$

The value S is equal to 1 for an unpinned interface (the SBH value is the same between Equation 5 and 6), and it tends to 0 when the interface is pinned. There are two principle models to explain Fermi-level pinning: Metal Induced Gap States (MIGS) and defect states.¹³⁶ In the first case a semiconductor in contact with a metal possess intrinsic states within its bandgap. These states are the MIGS, which are the evanescent states of the metal's travelling wave states that decay in the semiconductor.^{137, 138} The charge neutrality level, is the average energy of the dangling bond states. In contrast, it was shown that the Fermi energy on nonpolar (110) surfaces of III-V semiconductors was pinned at the same energy for different metals or oxygen, therefore it was related to intrinsic defect states.¹³⁹ In general both effects can cause pinning, and the prevalent one depends on their concentration.^{140, 141}

In the case of MoS₂ typical S values are between 0.11 and 0.15. The charge neutrality level was evaluated to be 4.57 eV for bulk samples and 4.48 eV for monolayers, so almost thickness independent. In terms of $E_C - \phi_{CNL}$ the values are 0.12 and 0.2 eV for bulk and monolayer MoS₂ respectively. The Fermi level is therefore pinned close to the conduction band minimum at the metal/MoS₂ interface.¹⁴² Due to the high density of defects as introduced before, these effects can be connected with the high density of defects present on the semiconductor surface. A defect density of 0.3%, which is common in TMDs, was shown to be sufficient to dominate the contact behavior.^{91, 143} Even if some early studies showed ohmic contacts, these are probably related to the high variation of the material.^{30, 144, 145}

Undoubtedly, the contact resistance is a major bottleneck for the implementation of MoS₂, or other TMDs, in modern technologies. Although several options to improve the contacts are available there is still a certain variability between similar experiments. Typical routes to reduce the contact resistance or the Fermi Level Pinning relies on interface engineering, doping, annealing or process optimization. In addition, the technique needs to be compatible with semiconductor processing and guarantee a proper device behaviour with minimal SCE. This problem will be further studied in Chapter 3.

1.3.3 Modelling capabilities

Modelling is one of the few enabling methodologies that can reduce development cycle times and costs. It was estimated in the International Technology Roadmap for Semiconductors (ITRS) Modelling chapter that from 2013 onwards a 40% reduction in development time, and equally a 40 % reduction in development cost can be made from modelling activities.^{109, 146} These development time and cost saving figures are based on detailed input on the industrial use of Technology Computer-Aided Design (TCAD) which was compiled by approximately 130 separate entities including semiconductor companies, equipment companies, and some leading research institutes working on process integration.

As will be explained in more detail later in this paragraph, in Chapter 6 and Chapter 8, the aim of this dissertation in this regard is the use of modelling to understand the main limitations of 2D-semiconductors and as well study their transport behavior. Several methods exist to model the behavior of an electronic device and several have been applied for 2D-FETs. These methods can be generally divided into two main approaches: quantum transport and semiclassical transport. The

former is based on the work by Landauer¹⁴⁷ and the Keldysh formalism,¹⁴⁸ while the latter is based on the Boltzmann transport equation (BTE).

The non-equilibrium Green's functions (NEGF) formalism is a quantum transport approach where the open-boundary Schrödinger equation is solved.¹⁴⁹ NEGF can accurately provide the free carrier concentration and the transmission coefficient and has been used on a variety of TMDs and heterostructure devices.¹⁵⁰⁻¹⁵³ However, since its formalism is based on the single-particle approach and the mean-field approximation, it is not suitable in case of strongly correlated transport or in the Coulomb blockade regime.¹⁵⁴

Monte Carlo simulations are instead a semiclassical approach. In this method the transport of free carrier is studied considering their scattering mechanisms when an electric field is applied.¹⁵⁵ This method was applied to 2D-semiconductor devices for the study of transport behavior TMDs, silicene and germanene-based devices^{156, 157}. Another semiclassical approach are drift-diffusion simulations, which is the most used approximation to model transport in traditional semiconductors. It is derived for BTE under the relaxation time approximation, resulting in independent expressions for the electron and hole current. The continuity equation needs to be solved as well.^{158, 159} Lastly, the hydrodynamic model considers in addition to the drift-diffusion model heating effects.

The main difference of these methods is related to the accuracy and computational effort. Although NEGF and Monte Carlo simulations can guarantee a very high accuracy, their computational demand is high, especially if compared with drift-diffusion or hydrodynamic models. These are in turn characterized by lower accuracy since they cannot completely capture quantum confinement effects and ballistic transport, for example.¹⁵⁴ Nonetheless, drift-diffusion models are still being

used to study the behavior of a variety of FET devices at scaled dimensions for advanced nodes.¹⁶⁰⁻¹⁶² It was shown that the effect from quantum confinement or ballistic transport can be implemented in the drift-diffusion model considering the results from more advanced calculations (Monte Carlo, density functional theory, empirical pseudo potential method). In this way, the computational efficiency of the drift-diffusion as well as the accuracy of more advanced calculation is maintained.¹⁶⁰

Therefore, although opportune tuning from a variety of sources is necessary, drift-diffusion modelling is still a viable option to have an initial understanding of the main advantages and limitations of 2D-semiconductors.

In this dissertation, the drift-diffusion model is considered using the TCAD software Synopsys Sentaurus Device.¹⁴⁶ This is a continuum physics-based modelling software and it solves systems of equations that describe the physics of the semiconductor. The simulations depend on the solutions of Poisson and drift-diffusion equations. In these simulations, a device is represented by a 2D or 3D meshed finite-element structure. For each node each equation is self-consistently solved. In particular, the solution of the Poisson equation is the electrostatic potential:

$$\nabla^2 \phi = -q(p - n + N_D - N_A) - \rho_{trap} \quad (8)$$

Where ϵ is the electrical permittivity, q is the elementary electronic charge, n and p are the electron and hole densities, N_D is the concentration of ionized donors, N_A is the concentration of ionized acceptors and ρ_{trap} is the charge density contributed by traps and fixed charges. The electron and hole densities can be computed from the electron and quasi-Fermi potentials, and vice-versa. As will be detailed in Chapter 6, Fermi statistics will be used for electron and holes:

$$n = N_C F_{1/2} \left(\frac{E_{F,n} - E_C}{kT} \right) \quad p = N_V F_{1/2} \left(\frac{E_V - E_{F,p}}{kT} \right) \quad (9)$$

Where N_C and N_V are the effective density of states for the conduction and valence band, $E_{F,n} = -q\Phi_n$ and $E_{F,p} = -q\Phi_p$ are the quasi-Fermi energies for electron and holes respectively, E_C and E_V are the conduction and valence band edges, $F_{1/2}$ is the Fermi integral of order 1/2.¹⁶³ Lastly, the carrier transport is evaluated through the drift-diffusion model:

$$\begin{aligned} \vec{J}_n &= \mu_n (n \nabla E_C - 1.5 n k T \nabla \ln m_n) + D_n (\nabla n - n \nabla \ln \gamma_n) \\ \vec{J}_p &= \mu_p (p \nabla E_V + 1.5 p k T \nabla \ln m_p) - D_p (\nabla p - p \nabla \ln \gamma_p) \end{aligned} \quad (10)$$

where:

$$\gamma_n = \frac{n}{N_C} \exp \left(\frac{E_{F,n} - E_C}{kT} \right) \quad \gamma_p = \frac{p}{N_V} \exp \left(\frac{E_V - E_{F,p}}{kT} \right) \quad (11)$$

The first term in Equation 10 considers the contribution due to spatial variations of the electrostatic potential, the electron affinity and the bandgap. The remaining terms consider the spatial variation of the effective masses of electrons (m_n) and holes (m_p) and the contribution due to gradient of the electron and hole concentrations through the diffusion coefficient D_n for electrons and D_p for holes.^{163, 164}

In addition, to properly simulate a device any TCAD software require a so-called “parameter file” of the materials under consideration. This file contains the basic material parameters that are necessary for the software to evaluate the behavior of the material (Table 2). In the case of MoS₂, or any other new semiconductor, these parameter files are not yet present. Therefore, it was necessary to implement them

considering previous ab-initio calculations and experimental results. Table 1a summarizes the main parameters. This kind of work is similar to what was done before to develop models for Si and Ge, which are now widely used and extremely important in the integrated circuit community to analyze materials and device architecture at advanced technology nodes.¹⁶⁵ For the case of 2D-semiconductors it is necessary to manually add them, as a properly formulated model for MoS₂ or any other TMD is not yet available. Because of the high number of parameters and data required, TCAD models for new material systems are usually missing in the first years, and they take some time to be developed and tuned properly. Therefore, most of the initial work relies only on experimental results.

Table 2: Main parameters modified in Sentaurus device to introduce MoS₂.

Material parameters	Note	Thickness dependency
Bandgap	Ab-initio	✓
Electron Affinity	Experiment	✓
Effective mass	Ab-initio	✓
Dielectric	Experiments and ab-initio	✓
DOS	Ab-initio	✗

Although experimental results are invaluable, the methodology used in this Thesis is slightly different.^{154, 166} This is depicted schematically in Figure 11. Instead of using only the experimental data to study the material and electrical properties of 2D-semiconductors, the experimental results are fed-back into the simulator, previously tuned considering first-principle calculations from literature. In this way, not only the TCAD model will be closer to reality as it was tuned against experimental

data, but it is also possible to have insight into physics that would be otherwise inaccessible experimentally.

In order to have a TCAD model closer to experiment not only it is necessary to adjust basic material parameters, but it is also necessary to add the defects that are at the base of the experimental behavior. In particular, Table 3 shows the main defects or imperfections introduced in Sentaurus device in order to study the experimental devices. Through a careful tuning and introduction of several defects, not only is possible to emulate more correctly the experimental results, but it is also possible to understand the main problems of the device itself. This added knowledge can be useful for a more careful planning of future experiments.

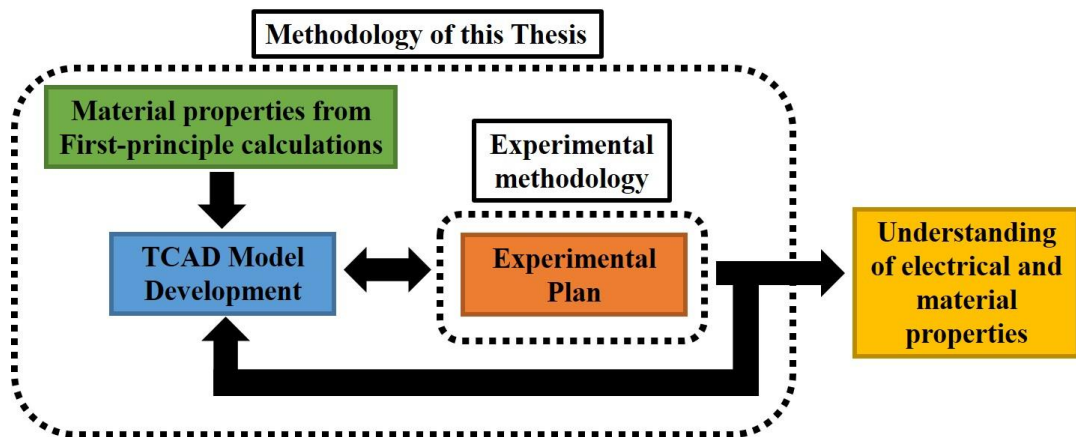


Figure 11: Schematic of the methodology used in this thesis in order to develop a TCAD model for MoS₂ based on both first-principle calculations and experimental data.

For example, as will be introduced in Chapter 6 in more detail, thanks to the TCAD model it was possible to confirm that it is the high impurity concentration in MoS₂ which is the major scattering mechanism, limiting the maximum achievable carrier mobility. As well, considering capacitance-voltage measurements on top-gated MoS₂, it was possible to pin-point the energy level responsible for the dispersion in

CV response. This energy level is consistent with the one on Sulphur vacancies, most common defect in exfoliated MoS₂ as introduced in the previous paragraph.

A similar methodology was rarely but effectively used in other works related to MoS₂. For example, a combination of experimental results and TCAD analysis was used described the charge capture and emission processes in gate oxide trap which were causing hysteresis in monolayer MoS₂ back-gated FET.¹⁶⁷ Another study focused on the carrier injection at the metal/MoS₂ interface and opportune steps to reduce contact resistance.¹⁶⁸ These works along with a deeper insight on the use of the software will be studied in Chapter 6.

Table 3: Main models and defect modified in Sentaurus device for a better modelling and understanding of MoS₂-based devices.

Models considered to study TMD-based devices
Interface traps
Impurities
Mobility
Schottky barrier and FLP

1.4 THESIS STRUCTURE

This dissertation addresses different issue of 2D-semiconductors considering from both a material and an electrical characterization perspective.

Chapter 2 provides a systematic study of the air sensitivity of different TMDs. In particular, HfSe₂, the most reactive, is further studied by a combination of several techniques in order to elucidate the degradation mechanism.

Chapter 3 deals with the optimization of contact resistance of MoS₂ devices by employing highly doped samples. The data are compared with a short literature review on contact optimization for TMD devices. In addition, the data are used in conjunction with the TCAD model developed for MoS₂ in order to study the optimal device structure for ultimate device scaling.

In Chapter 4 a combination of experimental results on thin MoS₂ are combined with fitting from DFT calculations to study the impact of impurities on the carrier mobility. The data consider different thickness, doping and substrates of MoS₂.

Chapter 5 introduces the electrical and material characterization of a different TMD, PtSe₂. Due to the ability of growing this material over a large area, a systematic material and electrical study is carried out in order to elucidate the effect of annealing on the metal-PtSe₂ interface.

Chapter 6 summarizes the development of the TCAD model. The first part deals with the setup of all the necessary material parameters and tuning of the basic models. Then, mobility models are opportunely tuned in order to match previous theoretical and experimental results. This model is then used to elucidate experimental results, focusing on contact and interface traps.

In Chapter 7, the software is used to introduce the layered structure concept, in order to further improve the modelling and understanding of 2D-semiconductors. The model is tuned against experimental data and used to study the scaling behaviour of MoS₂-based FETs.

Finally, Chapter 8 summarizes the major result of this study and discusses possible future works that can help to expand the understanding of 2D-semiconductors.

Chapter 2: AIR SENSITIVITY OF TMDs

This chapter is adapted from the following publication:

Mirabelli, G.; McGeough, C.; Schmidt, M.; McCarthy, E. K.; Monaghan, S.; Povey, I. M.; McCarthy, M.; Gity, F.; Nagle, R.; Hughes, G.; Cafolla, A.; Hurley, P. K.; Duffy, R., Air sensitivity of MoS₂, MoSe₂, MoTe₂, HfS₂, and HfSe₂. *Journal of Applied Physics* 2016, 120 (12), 125102.

2.1 INTRODUCTION

In this chapter a systematic study of several TMDs have been carried out to study their reactivity in air. The sensitivity of a material system to ambient degradation can pose significant challenges in their use for electronics applications. First, an AFM study over a period of 27 days was carried out to understand the main differences between each TMD. The study considered the following TMDs: MoS₂, MoSe₂ and MoTe₂ to explore the 3 dichalcogenides of molybdenum. The study also considered HfS₂ and HfSe₂ which are also of interest as they have energy gaps of 0.9eV and around 2 eV, in the range of interest for logic devices. SEM analysis is used to corroborate the findings of the AFM studies. The most reactive TMD, HfSe₂, was studied by XRD to provide a quantitative insight on the reactions of the material. XPS measurements were used to determine the surface chemical composition and to investigate changes in the chemical state of the surface with ambient exposure. By observing the binding energy shifts and broadening of the core level peaks the extent of surface oxidation can be inferred. Finally, TEM cross-sections and EDX analysis give a better understanding of the structure of the surface features.

2.2 EXPERIMENTAL

For each of the 5 TMD's studied (MoS₂, MoSe₂, MoTe₂, HfS₂, HfSe₂) flakes were mechanically exfoliated from their bulk crystal counterpart with Scotch tape¹¹ and transferred to a substrate composed of 85 nm of SiO₂ on a highly-doped Si handle wafer. Immediately after the exfoliation, the samples were examined by AFM for an initial comparison of the materials under study. No methods were applied to clean the TMD surface. The AFM was operated in Tapping-Mode in order to avoid any alteration of the surface due to the contact between the AFM tip and the surface itself.

For each sample, every effort was made to repeatedly measure the same flake at approximately the same location, over an area of $5 \times 5 \mu\text{m}^2$. In the AFM study, the same analysis was systematically carried out periodically on each material over a 27-day period. Root-mean-square (RMS) roughness evolution of the surfaces was used to compare and understand the main differences between the TMDs studied, considering both a change of the metal (Mo or Hf) and/or a change of the chalcogen element (S, Se or Te).

The morphologies of the TMD sample surfaces were investigated using a FEI Quanta 650 SEM in high-vacuum. To improve the imaging gold was sputtered on the samples using an Agar sputter-coater. For structural analysis, cross-section samples were obtained by using the Dual Beam Helios Nanolab 600i system from FEI, using a Ga ion beam. Layers of protective material were used consisting of electron beam deposited C, Pt, and ion beam deposited C. Lamellas were thinned and polished at 30 kV 100 pA and 5 kV 47 pA, respectively. Cross-sectional Transmission Electron Microscopy (XTEM) imaging was carried out using a JEOL 2100 HRTEM operated at 200 kV in bright field mode using a Gatan Double Tilt holder. EDX analysis was performed using STEM-EDX on a FEI Titan 80-300kV S/TEM. Analytical STEM provides a sub-nanometre, high current probe ($\sim 0.5 \text{ nm}$, 0.56 nA) allowing for site specific EDX analysis on the nanometre scale.

For the XPS analysis flakes were mounted and held on an XPS sample holder using an adhesive carbon pad. Flakes were then cleaved using the Scotch tape method and placed into a vacuum chamber in less than 30 seconds to minimise atmospheric contamination for the base, freshly cleaved, measurement. Once the freshly cleaved flake was measured the sample was removed and exposed to ambient atmospheric conditions for a period of 1 hour and reloaded for XPS measurement. The process of

exposing the sample was repeated for a 3 hour and a 48-hour exposure. Following the 48-hour measurement the flake was re-cleaved using Scotch tape. For HfSe₂ the XPS spectra were taken of the Hf 4f and the Se 3d core level peaks following the different exposure times to observe how the peaks shapes change and more importantly the relationship of the ratio of the area under each peak which directly reflects the relative concentrations of the elements present within the XPS sampling depth which is typically 5-7 nm. The XPS system used an aluminium anode to generate X-ray photons of 1486 eV and had an operating base pressure of approximately 2.0×10^{-9} mbar with the analysis area of the order of 0.5 cm².

2.3 SURFACE AND CROSS-SECTIONAL ANALYSIS

Right after exfoliation none of the materials showed obvious signs of degradation. Figure 1a and 1b are representative AFM images of MoS₂ and HfSe₂ surfaces 24 hours after exfoliation. These two materials were the most stable and least stable extremes respectively, among the TMDs studied. Twenty-four hours after exfoliation, HfSe₂ showed signs of degradation. Its surface, as shown in Figure 1b, is characterised by several protrusions randomly located across the surface, reaching a height of 57.4 nm high after 1 day. This behavior is in clear contrast with the one of MoS₂. The 2D AFM image in Figure 1a shows a darker z-shaped region. A cross-sections analysis shows this feature to be ~0.65 nm deep, which suggests a missing single-layer of MoS₂, which is known to be ~0.65 nm thick. This slight non-uniformity of the top surface might be related to the mechanical exfoliation method, which does not always guarantee a uniform surface over a large area. The same feature was located in later AFM measurements and there were no signs of any deterioration. Therefore, the material is relatively stable upon air exposure.

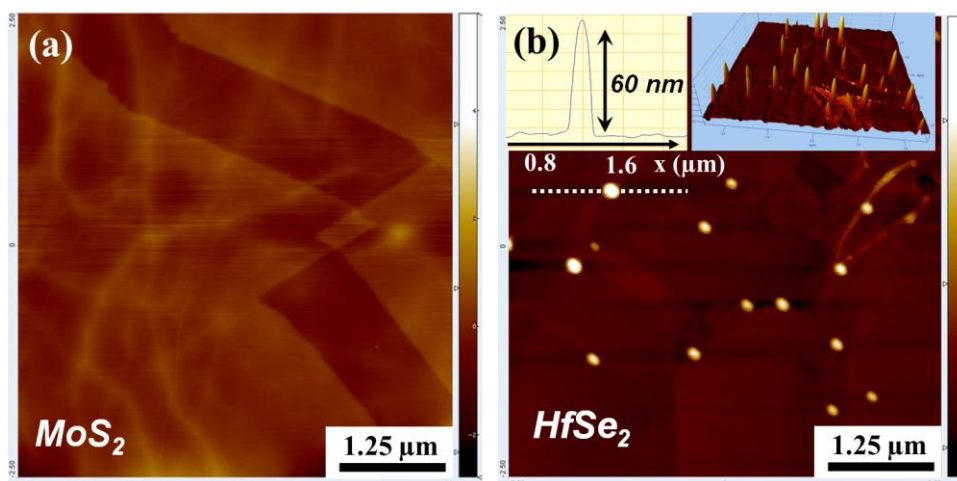


Figure 1: (a) Representative MoS₂ AFM image taken 24 hours after exfoliation. (b) Representative HfSe₂ AFM image taken 24 hours after exfoliation. The insets show cross-section of the tallest protrusion found on HfSe₂ of approximately 60 nm (white line scan in the main Figure), and a 3D representation of the data.

The main results of the AFM study can be summarised by the RMS roughness trends of the surfaces shown in Figure 2, for both the Mo-based and Hf-based TMDs. As previously stated, the MoS₂ is the most stable and it is the only TMD that did not show any obvious visible features or surface change during the period of study, implying that it is the most suitable TMD for electronic applications from a material point of view. The RMS roughness values for MoS₂ are relatively and constant (~0.2-0.4 nm) throughout the 27 days. MoSe₂ showed one peak related to air exposure, similar to those found on HfSe₂ surface, of ~27 nm height on the 9th day after exfoliation. Subsequently, on the 27th day, the surface was quite degraded, but without any other tall protrusions. MoTe₂ surface features were detectable after 3 days and were spread almost uniformly across the surface. These studies indicate a general trend in decreasing ambient stability for a given metal in the TMD as the chalcogen element changes from S to Se and finally Te. For example, from Figure 2(a) it is seen that the RMS roughness of HfS₂ is significantly lower than that of HfSe₂ during the period

studied. The degradation of HfSe_2 is visible 1 day after exfoliation, while signs of degradation are only visible 9 days after exfoliation for HfS_2 .

Some variation is noted in the RMS data shown in Figure 2 which may be attributed to a number of factors; while it was attempted to return to the exact same $5 \mu\text{m} \times 5 \mu\text{m}$ area on each flake, there may have been some misalignment due to handling or variation caused by changing AFM tip over the period of study. Furthermore, for the HfSe_2 it was noted that some of the surface features disappeared from one measurement to the next, which may indicate that these features are not tightly bound to the surface. Despite this “noise” in the data in Figure 2, the overall

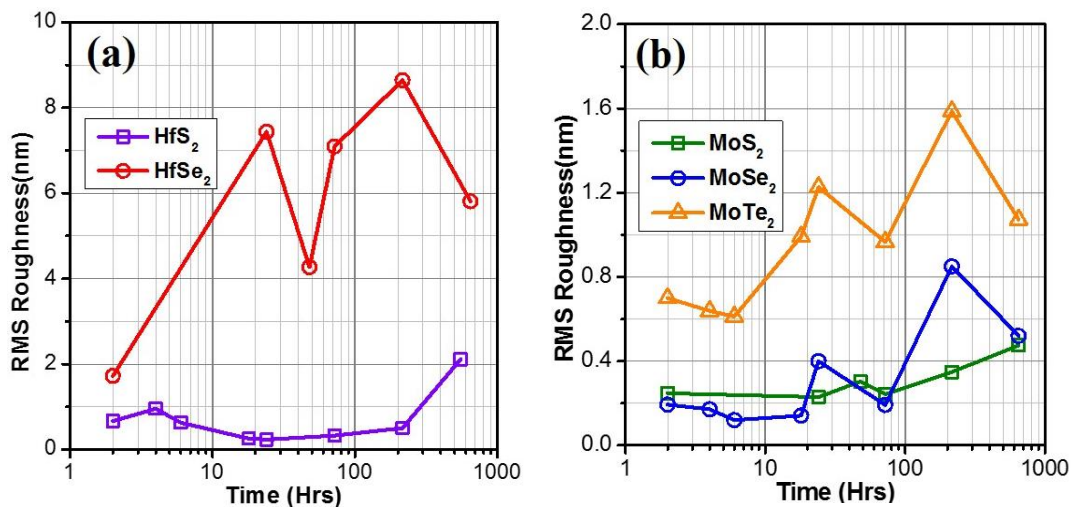


Figure 2: RMS surface roughness trends for (a) Hf-based and (b) Mo-based TMDs. Note the difference in the y-axis scales.

trends observed are reliable, namely a general surface roughening with time, with observable differences between the five TMDs under study.

To emphasize the quick degradation of HfSe_2 , Figure 3a reports the height of the tallest blister found during each AFM measurement, along with the defect density. The blister height is steadily increasing with time, going from $\cong 60$ nm after 1 day to $\cong 100$ nm after 27 days. On the contrary the defect density seems to decrease with time.

Nevertheless, this is likely related to a non-uniform distribution of the blisters and the fact that they coalesce together with time, as it will be clearer later from SEM images. In support of this Figure 3b shows an optical picture of a freshly exfoliated HfSe₂. In contrast, Figure 3c shows the same flake after 4 months. Clearly the degradation affects the overall surface of the flake.

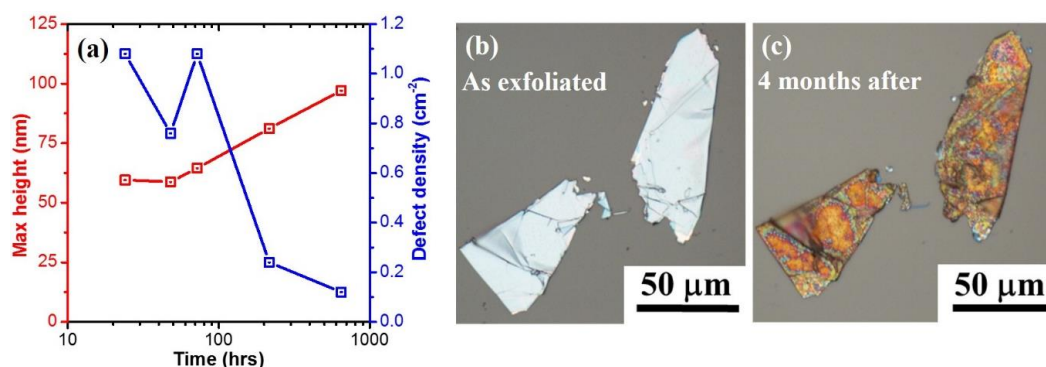


Figure 3: (a) Maximum height of the blister and defect density found for HfSe₂. Optical pictures of HfSe₂ (b) as exfoliated and (c) 4 months after.

In order to analyse the results of the AFM study more thoroughly, all TMDs were examined by SEM, and HfSe₂ was further studied by STEM, XTEM, EDX, and XPS, since it showed the highest reactivity on contact with air.

Figure 4a shows an SEM measurement of the HfSe₂ surface 1 day from exfoliation. The blisters are found primarily along step edges, even if some are found on the planar surface as well. The inset in Figure 4a show a flake five months after exfoliation. Considering the two images, they show the same kind of blister like protrusions in terms of form and shape, only smaller in fresher samples. Furthermore, it is clear from the images that the blisters have a higher density at the step-edges. The step-edges of the top-surface, related to the mechanical exfoliation method, are characterised by dangling bonds that may be optimal nucleation sites for the growth of the features. Nevertheless, Figure 4b show HfSe₂ five months from exfoliation on

a much bigger scale. Even if the protrusions might preferentially growth initial along the step edges, after a certain amount of time the whole surface is degraded, as seen before from optical pictures in Figure 3c.

Also, it is important to compare the density of protrusions found during the AFM study. The blister density in the AFM image in Figure 2, is approximately $8 \times 10^7 \text{ cm}^{-2}$, while the SEM image in the inset of Figure 5a has a blister density of approximately $4.3 \times 10^7 \text{ cm}^{-2}$. The difference in defect density is attributed to the fact that a different area was scanned in AFM and SEM. Note, the same type of terrace edges were found on MoS_2 (Figure 1a), but they were not decorated with growths of blister-like features during the period of study. Other TMDs were studied by SEM in a similar way, but no obvious surface features were observed. For example, the inset in Figure 4b shows the HfS_2 surface after 5 months of air exposure. The terraced nature of the material is obvious and is related to the layered structure of the material itself, and the mechanical exfoliation process. The surface appears to be uniform with no blisters present, at least under this magnification. A similar lack of obvious surface features was characteristic in the SEM images of MoS_2 , MoSe_2 , and MoTe_2 .

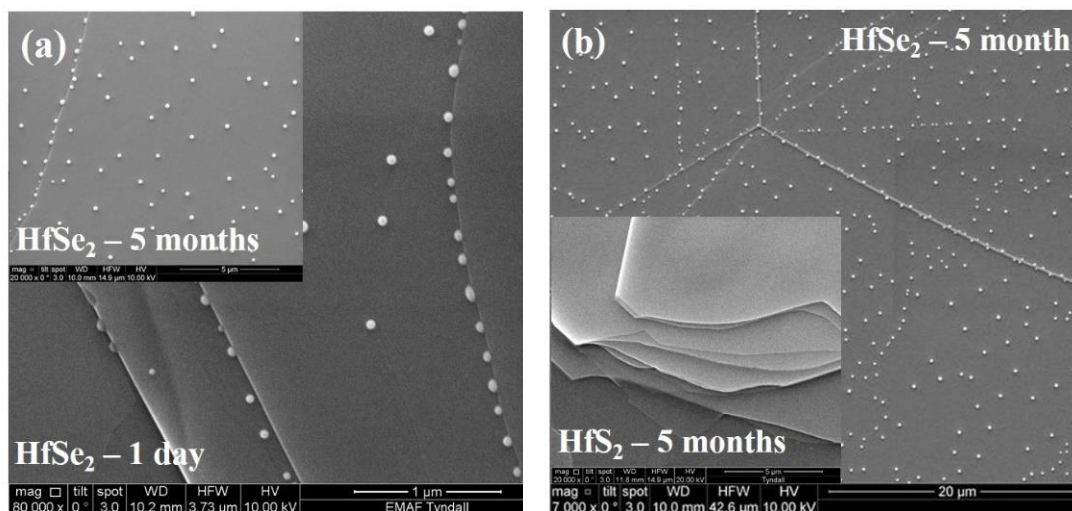


Figure 4: (a) Representative SEM image of HfSe₂ after 1 day from exfoliation; the inset shows the surface 5 months from exfoliation. (b) Representative image of HfSe₂, which shows how the whole surface is contaminated with blisters. The inset show HfSe₂ after 5 months from exfoliation. The terracing is related to the mechanical exfoliation and the layered nature of the material. No blister features appear to be evident.

A similar comparison was done considering TEM cross-sections of MoS₂, MoTe₂ and HfSe₂ as exfoliated (day 0) and after 30 days from exfoliation. These group of TMDs comprise the best and the worst of the whole group considered before (MoS₂ and HfSe₂), and the best and worst of the Mo-based TMD group (MoS₂ and MoTe₂). Figure 5a and 5d show the HfSe₂ cross-section at day 0 and 30 respectively. An initial oxidation layer can be clearly seen in Figure 5a, with a complete degradation of the surface after 30 days. In sharp contrast, MoS₂ on day 0 (Figure 5c) shows a very sharp interface from the top layer and the C-layer used as protection layer. Similarly, after 30 days (Figure 5d), there are no sign of apparent degradation, and the layered structure is clearly visible throughout the whole lamella (~10 μm). Comparably, MoTe₂ did not show any surface imperfections as exfoliated (Figure 5e). After 30 days (Figure 5f), the surface does not show any sign of reaction from this analysis. Interestingly, both the MoS₂ and MoTe₂ crystals exposed in air for 30 days show sign of what seems to be stress. Nonetheless, it is difficult to conclude that this effect is

strictly related to air exposure. The fabrication process steps used to prepare the lamella might have induced stress in the structure as well.

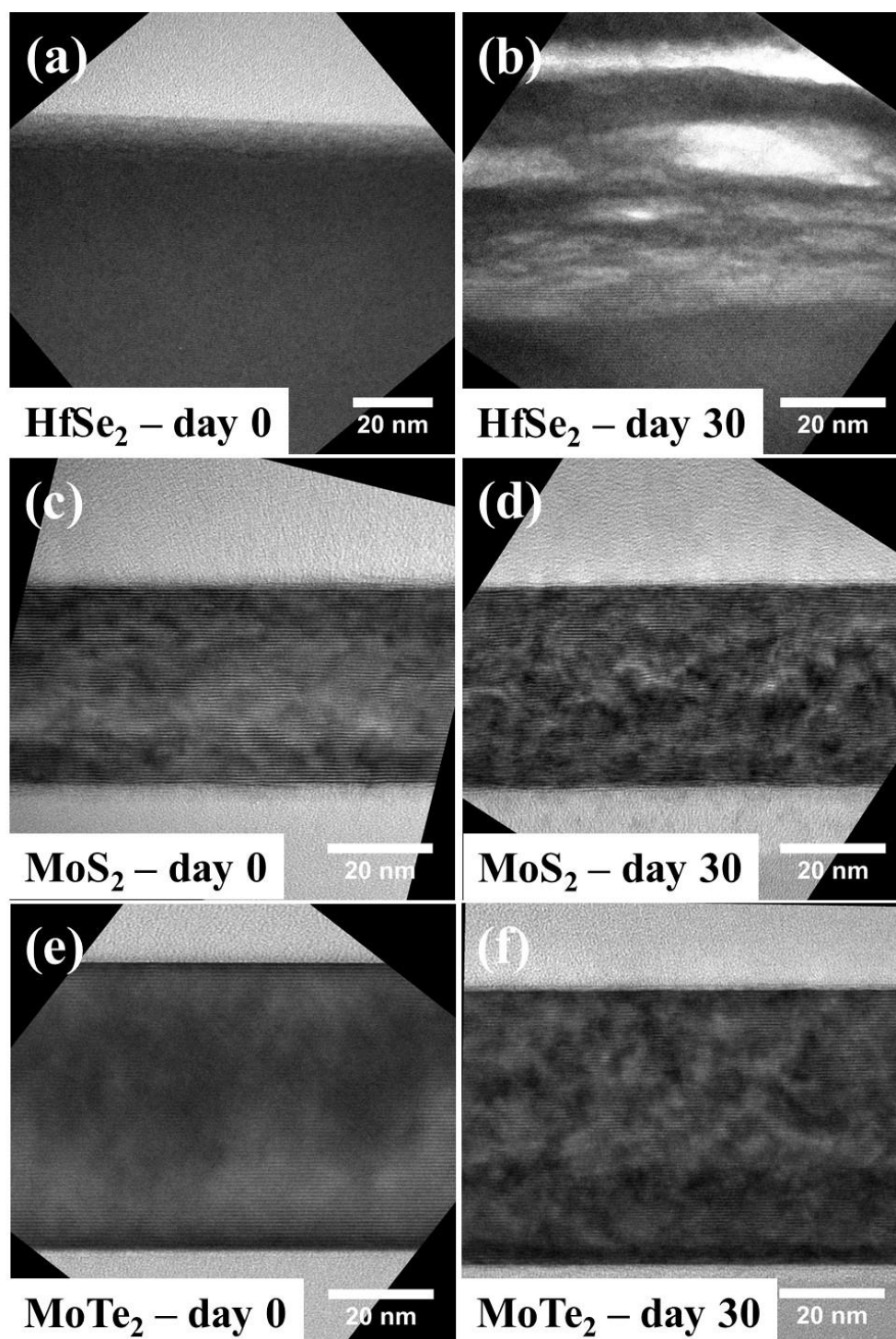


Figure 5: Cross-section TEM of HfSe₂, MoS₂ and MoTe₂ as exfoliated (a, c, e) and after 30 days (b, d, f) respectively.

Additionally, EDX analysis was used to study the chemical composition of the blisters found on HfSe₂. Figure 6 shows representative TEM images of HfSe₂ after 5 months of air exposure. In the following Figures (Figure 6-8) the surface features look like hemispherical shaped blisters which are approximately 180-240 nm tall and 420-540 nm wide. Figure 6a shows a HfSe₂ flake approximately 280 nm thick, while Figure 6b shows a thinner flake, approximately 40 nm thick. Blisters appear on both thick and thin flakes with approximately the same dimensional size. The material within the blister appears to be amorphous in nature. Also, they are surface features, as they are not formed throughout the bulk of the material. As it is clear from Figure 6a, the surface region of the HfSe₂ beneath the blister is highly disordered. Also the top surface of the HfSe₂, between the blisters, appears to be degraded as it is non-uniform and less homogeneous than the bulk portion of the flake. Thus, the surface reactions resulting from ambient exposure of HfSe₂ could be considered to consist of two distinct features, namely localised blisters and planar surface modification. A delamination crack is evident in the same figure within the HfSe₂, highlighting that these TMDs are layered materials that may have mechanical weaknesses between the layers. It should be noted that the crack is likely to have occurred during TEM sample preparation.

In terms of area coverage, assuming a circular blister with average width of 480 nm, and a density of $4.3 \times 10^7 \text{ cm}^{-2}$, the area covered by these features is approximately 8% of the HfSe₂ surface.

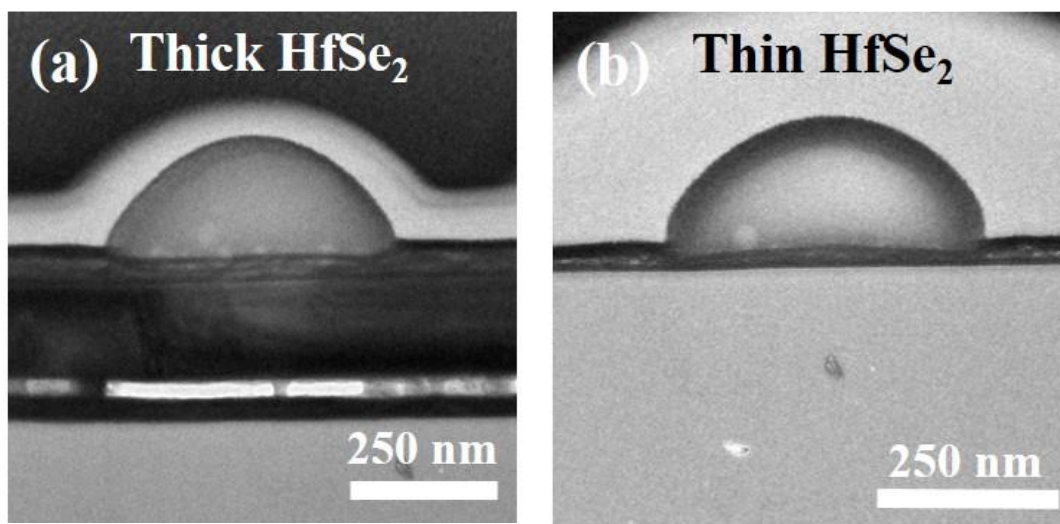


Figure 6: Representative TEM images of HfSe₂ after 5 months from exfoliation. Hemispherical shaped surface features appear amorphous in nature and are of similar dimensional size on both the (a) thick and (b) thin flakes.

Figure 7 provides extra insight into the structural makeup of the blisters, as the thinner flake, seen in Figure 6b was examined further. A surface blister was magnified, and initially appeared homogeneous. However prolonged electron irradiation over several minutes, a void appeared in the middle of the feature (Figure 7b). The void is likely formed by beam induced knock-on damage causing a small void to appear and proliferate to a large hole. It may be coupled with beam induced heating causing a melting type effect. This may indicate that the middle of these features are structurally less stable, much like a bubble. Also note that the Au, deposited to enable the SEM imaging as indicated earlier, is visible on the outer surfaces of these features.

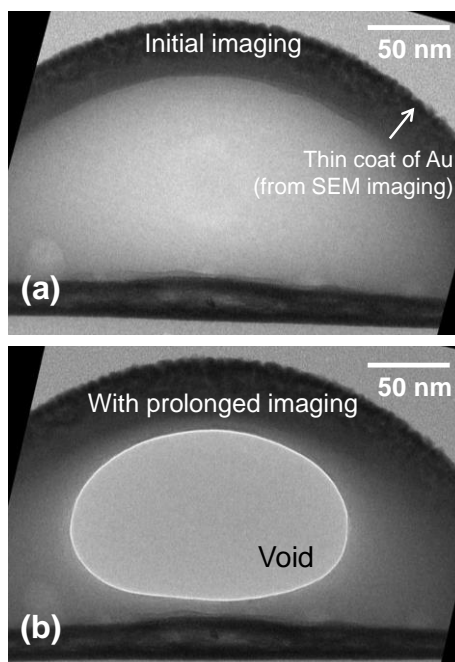


Figure 7: TEM imaging of the blisters on the thin HfSe₂ flake shows that (a) during initial imaging the blister is continuous and that (b) after a few minutes of electron irradiation a void is formed in the middle.

2.4 EDX AND XPS ANALYSIS

Figure 8 shows compositional analysis performed on the surface blisters via STEM based EDX. Figure 8(a) shows a STEM image across which the EDX analysis was performed. In the STEM image the contrast is reversed compared to bright field TEM. The structural non-uniformity is again evident in regions below the blister, and to the left and right of it. Figure 8b and 8c show the EDX maps for Hf and Se respectively recorded across the STEM image in shown in Figure 8a. Notice that the blister is primarily composed of Se, with only trace amounts of Hf. There are patches within the HfSe₂ layer that show increased concentrations of Hf accompanied by a Se deficit in the same region. These Hf/Se concentration changes are only present at the top of the layer. The bulk region of the HfSe₂ is uniform.

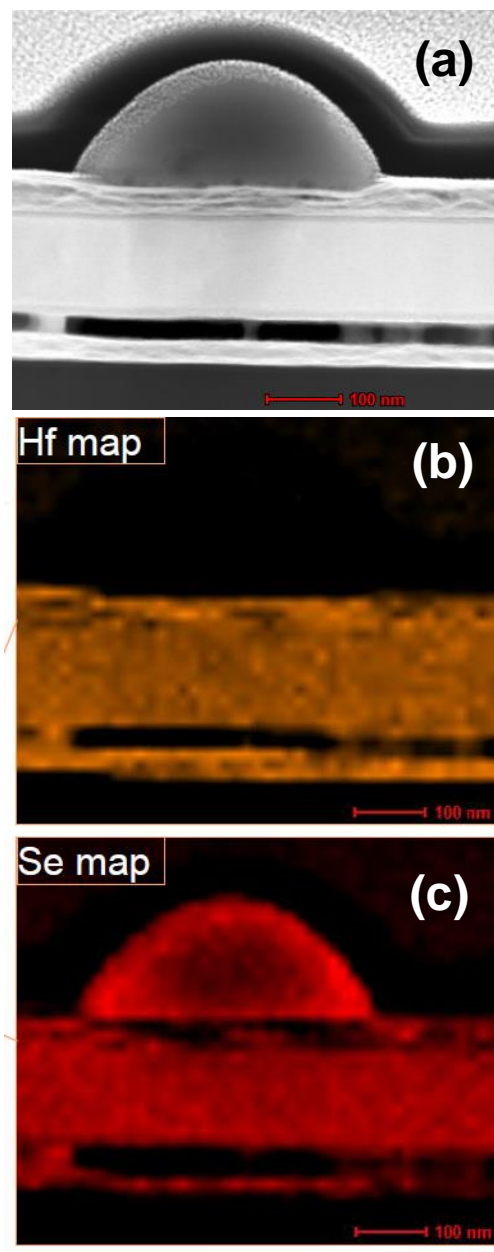


Figure 8: EDX data showing (a) the region mapped, (b) the Hf map, and (c) the Se map within the HfSe₂ flake and surface blister. The blister is Se-rich with little or no Hf present. The regions below the blister are depleted of Se.

The XPS study data for HfSe₂ as a function of ambient exposure are displayed in Figure 9-12. The change in the elemental stoichiometry with ambient exposure time is displayed in Figure 9 and clearly shows the progressive loss of Se from within the XPS sampling depth (5-7 nm) over the 48 hr monitoring period with the Se:Hf ratio reducing from the initial 2:1 to 1.4:1. Note a similar study on MoS₂ showed no changes

in the elemental composition under an equivalent ambient exposure again confirming relative surface stability.

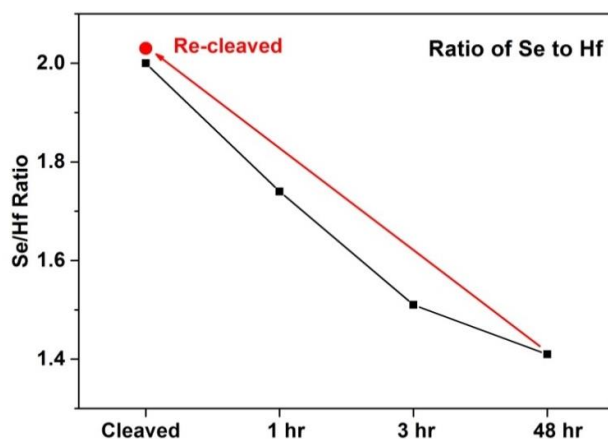


Figure 9: Plot of the change in Se/Hf elemental ratio following ambient exposure of the freshly cleaved surface. The re-cleaving process restores the surface to the original elemental composition by removal of the oxidised surface.

Analysis of the changes in the profile of the Hf 4f peak over the time span of this ambient exposure study shown in Figure 10 indicates increasing evidence for Hf oxidation. The Hf 4f peaks from a freshly cleaved sample in Figure 10(a) have a binding energy of 14.3 eV and 16 eV for the Hf 4f_{7/2} and Hf 4f_{5/2} component peaks respectively,¹⁶⁹ which are indicative of a Hf signal in the HfSe₂ crystal. The appearance and subsequent increase in intensity of component peaks, at binding energies of 15.4 eV and 17.1 eV in Figure 10 (b, c, and d), are indicative of the progressive oxidation of the Hf as the higher electronegativity of oxygen compared to selenium results in this core level shift.¹⁷⁰ The corresponding curve fitted Se 3d spectra,¹⁷¹ displayed in Figure 11 show a broadening of the peak profile without any evidence of higher Se oxidation states.

This can be interpreted in terms of the preferential formation of Hf oxides following ambient exposure with the consequential release of Se, some of which

desorbs from the surface and some of which gets trapped in the blister structures. The fact that these blisters are predominantly found along step edges is consistent with the Hf oxidation process initiating along the step edges where ideal surface termination is absent.

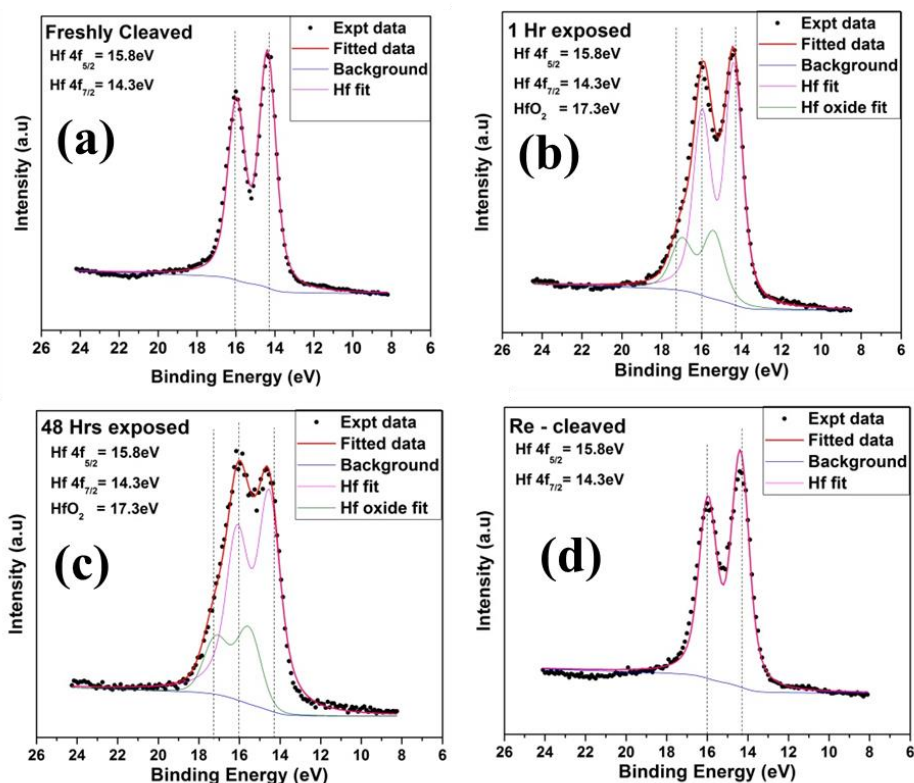


Figure 10: Hf 4f peaks; (a) Freshly cleaved HfSe₂ surface shows the Hf 4f_{5/2} and Hf 4f_{7/2} component peaks at binding energies of 14.3 eV and 16 eV, respectively. The peak profiles following ambient exposure of 1 hr (b) and 48 hrs (c) clearly display the growth of higher binding energy oxide component peaks at 15.4 eV and 17.1 eV. The unoxidised Hf signal is regained after re-cleaving of the top surface (d), removing the surface oxide.

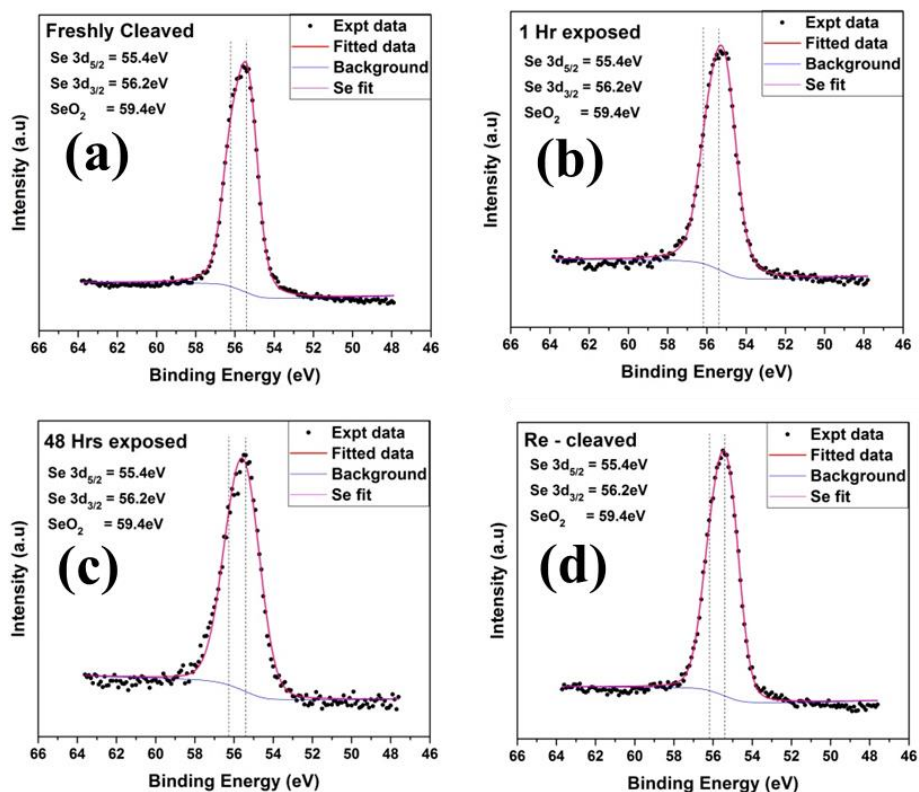


Figure 11: Se 3d peaks; (a) Freshly cleaved Se3d peak is curve fitted with an unresolved doublet with binding energy of Se $3d_{5/2}$ =55.4 eV and Se $3d_{3/2}$ = 56.4eV. Curve fits of the 1 hr (b) and 48 Hrs (c) air exposed samples show no significant change to the peak profile with no evidence of higher oxidation states of selenium (e.g. SeO_2 which has a binding energy of 59.4eV). Recleaning the sample as shown in (d) leaves the peak profile unchanged.

Further evidence for the preferential oxidation of Hf over Se comes from the binding energy and FWHM of the O1s peaks. In Figure 12, the FWHM of the 48 hrs exposed sample is 2.9 eV at 530.9 eV binding energy in agreement with Zhu et al.¹⁷² who reports a HfO_2 peak on a Si substrate to have a FWHM of 2.6 eV at a binding energy of 530.8 eV. Combined with the lack of evidence for SeO_2 in the Se3d spectra it can be concluded that the oxide is due to HfO_2 .

Considering the surface area contributing to the XPS spectra is of the order of 0.5 cm^2 , it is reasonable to conclude that the photoemission spectra are dominated by the areas between the blisters, which remain largely unchanged, as the surface coverage of these feature was estimated to be approximately 8%.

A remaining question is why the Se atoms produced by the preferential Hf oxidation coalesce into hemispherical features, as opposed to aligning parallel to the surface. The presence of a hemispherical shape suggests a construction to minimise surface tension. One possible explanation is that, as a result of the high temperature vapour phase growth process for the HfSe₂, gases are trapped between the 2D layers of the crystal, and the surface features contain a gas.

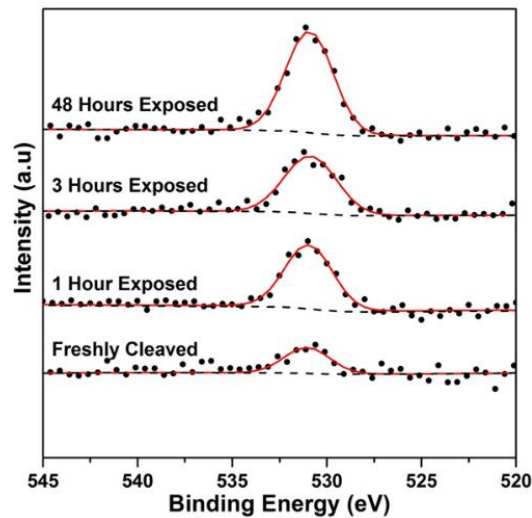


Figure 12: The O1s core level spectra as a function of exposure time.

2.5 DISCUSSION

Even though HfSe₂ was the most reactive among the TMDs studied here, HfSe₂-based FETs are currently found and studied in literature, with $I_{on}-I_{off}$ ratio exceeding 7.5×10^6 reported by Kang et al.¹⁷³ These devices were quickly passivated with resist, which can limit the effects of surface deterioration due to air exposure. The AFM images reported in that work of un-passivated HfSe₂ surface 1 and 8 days after exfoliation, show similar features to those presented in Figure 1b.

Also, a study of air exposure stability of HfSe₂ films grown by MBE is reported by Yue et al.⁵⁵. The oxidation reactions are reported to be related to the top surface of the film, which is less prone to oxidation when the crystalline quality of the film is improved. A higher quality might also mean fewer discontinuities on the surface, like step-edges, which this study would suggest are the optimal (but not essential) sites for HfSe₂ surface degradation. Gao et al.¹⁷⁴ showed that CVD grown monolayers of MoS₂ and WS₂ were very air sensitive. X-ray photoelectron and Auger electron spectroscopy performed in that work showed that gradual oxidation proceeded along grain boundaries along with the adsorption of organic contaminants. Degradation of CVD WS₂ was also reported by He et al.¹⁷⁵. Similar effects were also seen after a longer period on exfoliated thin flakes of MoS₂.¹⁷⁶

Another promising 2D-material is Black Phosphorus, whose surface shows similar features to that found for HfSe₂ here.¹⁷⁷⁻¹⁷⁹ The so-called bubbles grow in density and height after air exposure, regardless of the actual thickness of the Black Phosphorus flake, meaning that these effects are top-surface related. The density of these features on Black Phosphorus eventually decreases with air exposure since they become wider, merging together. In a subsequent study, Kim et al. reported the successful preparation of air stable multilayer phosphorene thin-films and transistors.¹⁸⁰ In that work a double layer capping of Al₂O₃ and hydrophobic fluoropolymer was used to produce air stability of the material.

The surface roughness trends observed in our AFM data are in accordance with the DFT calculations carried out by Liu et al.¹⁸¹. In that work it was stated that a TMD is more prone to oxidation as the chalcogen is varied from S, to Se, to Te, i.e. descending the periodic table. This can be due to the decrease in the electronegativity of the chalcogen from S to Te, which in turn makes the metal-chalcogen bond being

more susceptible to oxidation. Moreover, that work restricts the interaction between oxygen and TMDs to single chalcogen vacancies. These defects are more likely to occur in more reactive TMDs, so, considering that the S vacancy density for MoS₂ is reported to be in the order of 10^{13} cm^{-2} ,^{113, 114} the Se vacancy density would be expected to be higher in HfSe₂. Considering that defect density related to air exposure in this work is found to be in the order of 10^7 cm^{-2} from both the AFM and the SEM analysis, it is possible that these kinds of features are not related to chalcogen vacancies alone. These defects could play a role in the overall process,^{110, 182} but not all of them appear to be optimal sites for the growth of the blister shaped protrusions.¹⁸³ Indeed, for the case of MoS₂, DFT calculations have shown that a large kinetic barrier of 1.6 eV is present on a pristine MoS₂ surface for O₂ dissociation, which result in good stability. The calculated dissociation barrier at the edge sites is only 0.31 eV, making the edges and grain boundaries of MoS₂ susceptible to oxidation.^{182, 184} In addition, sulphur vacancies at the surface of MoS₂ are expected to reduce the oxidation barrier to 0.8eV, which would make them reactive defect sites.¹⁸⁵

It is clear that some of the TMD materials of interest from a device perspective are remarkably air sensitive.^{186, 187} Many other groups have reported material or electrical data indicating this, while the systematic study in this work gives more insight into the relative reactivity of the TMDs and the formation of the surface features. To think that these materials are purely 2D in nature is probably misleading, as this implies that top surface is totally unreactive in the perpendicular plane as there are no available covalent bonds in that plane. Unfortunately, it is not that simple, as it is clear that molecules present in air react with the TMD surfaces. As stated above a surface encapsulation using resists, insulators, or dielectrics have been demonstrated elsewhere as being effective protection layers.

Other solutions may lie in the area of chemical functionalisation or passivation of surfaces. For example one might think of graphene as a perfectly 2D material with no free bonds available for surface reactions or functionalisation, however Long et al.¹⁸⁸ found that graphene bonds non-covalently with alkane-amine groups, providing a pathway for solution-phase self-assembly. Furthermore O'Connell et al. discovered recently that molecular monolayer doping via chemisorption of organic molecules on Si surfaces actually suppressed oxidation of the Si surface.¹⁸⁹ In terms of surface protection of TMDs, non-covalent surface reactions or functionalisation may prove important to improving their air stability. Additionally, surface functionalization could potentially control the oxidation process of TMDs, which native oxide could be used as top-oxide for FET applications or for the growth of other oxides. On this, Mleczko et al.,¹⁹⁰ evaluated the performance of HfSe₂ and ZrSe₂ with native high-k dielectrics. Nonetheless, the devices were fabricated in an air-free environment, using nitrogen gloveboxes and vacuum chambers. In addition, 2.5 nm of AlO_x were deposited by low-temperature ALD to act as protective encapsulation layer and as a thin tunnelling barrier for the contact. Therefore, the material itself, even if sensitive, presents interesting characteristics and opportunities if the fabrication process is designed correctly. Similarly, FETs were fabricated using HfS₂ in a vacuum cluster system combined with a number of gloveboxes to maintain an air-free environment.¹⁹¹ In this work, even if HfS₂ was passivated with BN for passivation, it was not enough to completely suppress ambient degradation effectively. Therefore, it is evident that air contact affects the structural and electrical properties of these TMD materials by various degrees. Tackling this issue can be one of the biggest challenges for future TMD-based devices and technologies.

2.6 CONCLUSIONS

In this work we compared and contrasted the reactivity of MoS₂, MoSe₂, MoTe₂, HfS₂ and HfSe₂ in air. AFM, SEM, EDX, S-TEM, and XPS data were collected. Overall, surface roughening occurs for all TMDs over a period of time which indicates a formation of oxides or molecular adsorption on the surfaces. HfSe₂ and MoTe₂ were the most reactive of the TMDs studied. HfSe₂ in particular was characterised by the growth of Se-rich surface blisters, which form within one day of air exposure. It is theorised that the Hf is oxidising into HfO₂, which breaks down the HfSe₂ and excludes the Se at the surface. The Se atoms coalesce into blisters which continue to grow as more HfSe₂ is consumed and more HfO₂ is formed.

Chapter 3: THE EFFECT OF IMPURITIES AND DIELECTRIC ENVIRONMENT ON 2D- SEMICONDUCTORS

This chapter is adapted from the following publication and conferences:

Mirabelli, G.; Gity, F.; Monaghan, S.; Hurley, P. K.; Duffy, R. In Impact of impurities, interface traps and contacts on MoS₂ MOSFETs: Modelling and experiments, 2017 47th European Solid-State Device Research Conference (ESSDERC), 11-14 Sept. 2017; 2017; pp 288-291.

Mirabelli, G.; Duffy, R.; Hurley, P. K.; Monaghan, S.; Cherkaoui, K.; Schmidt, M.; Sheehan, B.; Povey, I. M.; McCarthy, M.; Nagle, R.; Bell, A., Mo-Based Transition-Metal-Dichalcogenide Junctionless Field-Effect-Transistors. Meeting Abstracts 2016, MA2016-01 (26), 1289-1289.

3.1 INTRODUCTION

One of the main problems of 2D-materials is the lack of a proper large-area growth technique. Often, grown TMD films are characterised by defects or grain boundaries, which limit their performances. Therefore, most of the MOSFET results to date showing high on/off ratios, low SS and mobilities in the range of tens of $\text{cm}^2\text{V}^{-1}\text{s}^{-1}$, have come from flakes mechanically exfoliated from bulk crystals. Nevertheless, a large concentration of unintentional impurities was reported in TMD crystals,^{90, 192} which is known to affect the behaviour of the material. In this study, we report on the electrical characterisation of back-gated MoS_2 flakes in order to study the impact of unintentional impurity concentration and dielectric environment. Overall, the performance of the devices are comparable with literature, with good $I_{\text{on}}/I_{\text{off}}$ ratio, but still, the unintentional impurities present in the material affect its transport properties masking the maximum potential of MoS_2 channel MOSFETs.

3.2 EXPERIMENTAL

Mechanical exfoliation with scotch tape was used to obtain thin flakes from a MoS_2 bulk crystal. The flakes were transferred on a substrate of 85 nm of SiO_2 and a highly-doped Si handle wafer. The height of the flakes was established by optical color-contrast.¹⁹³ Ti/Au metal contact pads and electrodes were defined by electron-beam lithography, followed by metal evaporation and a lift off process. The definition of the contact pads and electrodes was achieved using 15 kV beam exposures with a Zeiss SUPRA SEM with a Raith Elephy Plus blanker. The metal consisted of a 5 nm Ti adhesion layer and 45 nm of Au using e-beam evaporation.

For structural analysis, cross-section samples were obtained by using FEI's Dual Beam Helios Nanolab 600i system using Ga ion beam. Three layers of protective

material were used, namely electron beam C, electron beam Pt, and ion beam C. Lamellas were thinned and polished at 30 kV 100 pA and 5 kV 47 pA, respectively. Cross-sectional Transmission Electron Microscopy (XTEM) imaging was carried out using a JEOL 2100 HRTEM operated at 200 kV in Bright Field mode using a Gatan Double Tilt holder. For electrical characterization, the HP4156C parameter analyser was used.

3.3 MATERIAL ANALYSIS

In Figure 1 the SEM and TEM images of a typical device are reported. The device is referred to as the Trapezium based on its shape. Figure 1a shows the SEM of the flake. It was contacted by two metal tracks of Ti/Au (5/45 nm), separated by 1 μm . The width is approximately 3.5 μm along the length of the sample. Figure 1b shows the TEM cross section of the same device around the metal contact. There seems to be another 3 layers of MoS₂ above the actual flake, but in reality this is probably an artefact from TEM and there can be three explanations. Due to its low thickness, the material is bending in a direction perpendicular to the lamella. The second “top” MoS₂ is actually the same flake the bulged up inside the metal contact, so bending effects that happen in deeper regions. Probably thicker devices are less prone to bend under the same effect. Another hypothesis is that this kind of bending might be related to stress induced on the flake after the metal deposition or the lift-off process, as this effect seems to be related to regions around the metal contact (Figure 1d). Lastly, it can be related to the exposure of the SiO₂ substrate to the TEM electron-beam. The electron beam causes heating, and an associated expansion of the SiO₂ layer. The heat is removed more effectively under the metal contact area, resulting in a differential expansion of the SiO₂ inside and outside the metallised area. Considering a region

away from the metal contact in Figure 1c the three layers and thickness of 2 nm, assumed before only by optical inspection, are confirmed.

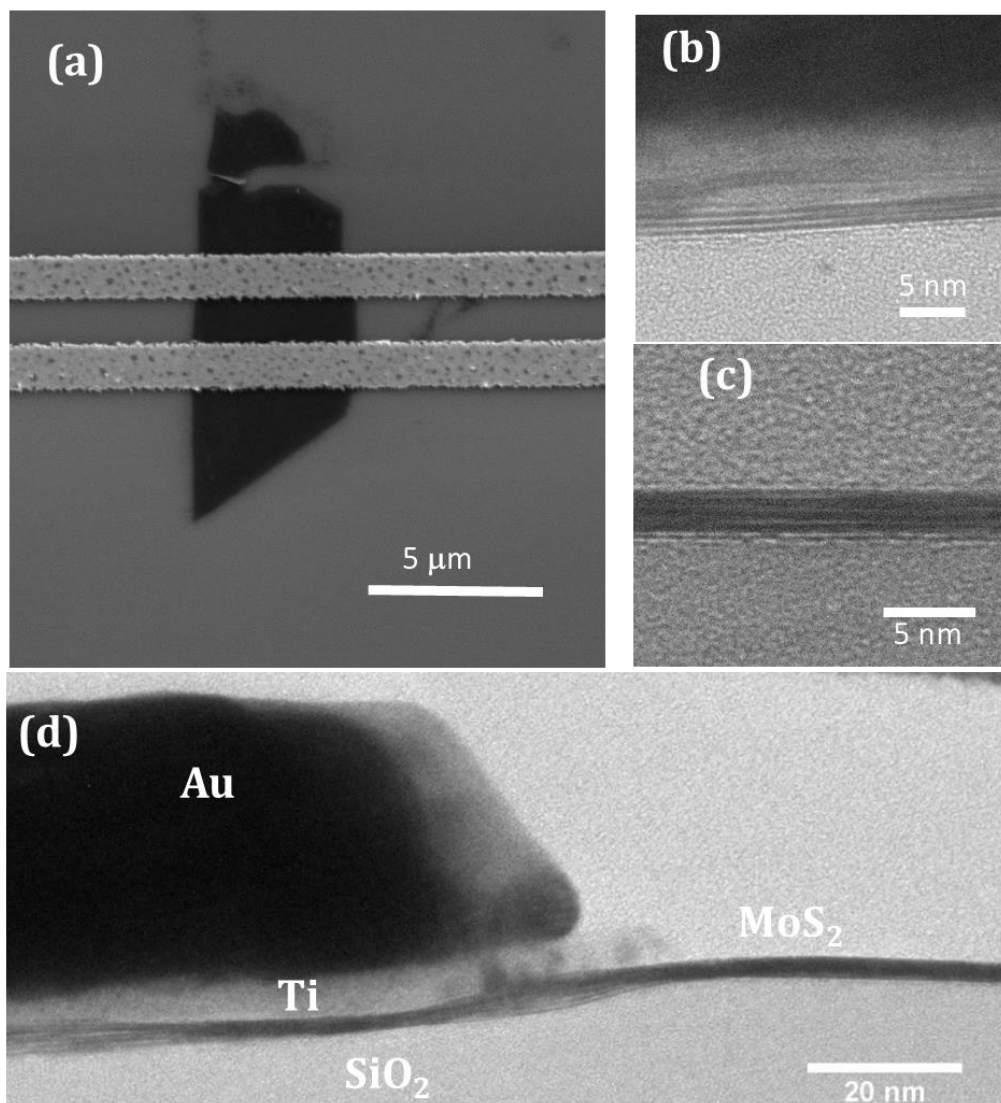


Figure 1: Representative SEM image of the Trapezium device showing the two metal tracks used to contact it. Representative higher-resolution TEM images showing (b) the MoS₂-Metal interface, and the layered structure of the flake (c) beneath and (d) outside the metal contact.

3.4 ELECTRICAL ANALYSIS

3.4.1 Extraction of impurity concentration

Figure 2 shows the transfer characteristics of the devices. The length of the devices is determined by the metal track distance, which is equal to $1\ \mu\text{m}$ for all of them. The drain current is normalized by width in order to have a clear comparison between the samples. Along the Trapezium other two devices are present: the Kite and the Triangle, similarly named after their shape. All of them have a comparable thickness of 3-4 layers.

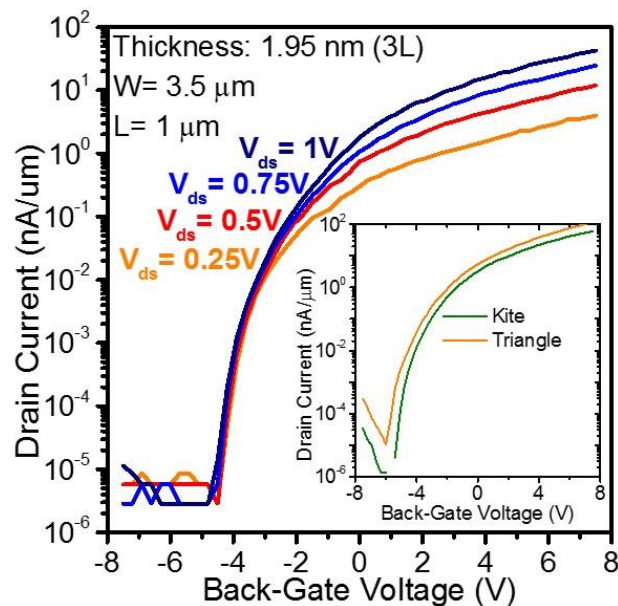


Figure 2: Transfer characteristics of the Trapezium at different drain-source voltages. Inset: transfer characteristics of the Kite and the Triangle at $V_{ds}=1\text{V}$.

It is possible to notice that there are few variations between the electrical characteristics. The drive current is almost the same, around $50\ \text{nA}/\mu\text{m}$, while the off current is limited by the analyser used, so it can actually be lower. The main differences can be related both to the slightly higher thickness or the high defect

variability of the material. As it was shown by McDonnell et al.¹⁴³, a defect density of 0.3%, which is common in TMDs can be sufficient to dominate the contact resistance.

Nevertheless, because of the inability to grow TMDs uniformly, systematic studies on a large number of samples are rare. The flakes here reported were exfoliated from the same bulk material onto the same substrate, facing all the same processes and environment-related exposure effects. Considering this, the variability among these devices is mostly related to intrinsic factors only (defects,¹¹⁰ grain boundaries,¹¹⁵ unintentional impurities¹⁹⁴) and process-related factors (metal contact¹²⁰ or air exposure¹⁹⁵) should affect them all in the same manner. Even if some variations are possible, this is still important for the sake of a first general understanding of the properties and problems of TMDs.

In order to further compare the limits and characteristics of the device field-effect mobility was systematically extracted. The mobility was determined from the derivative of the transfer characteristics, as usually done for TMD-based FET:

$$\mu = \frac{Lg_m}{WC_{OX}V_{DS}} \quad (1)$$

Where L is the length of the device, W is the width, gm is the transconductance, C_{OX} is the oxide capacitance and V_{DS} is the drain-source voltage.

Figure 3a shows the extracted mobility values (symbols) plotted against the carrier concentration, which can be simply estimated by:

$$n_e = C_{OX} \frac{(V_{BG} - V_T)}{q} \quad (2)$$

Where n_e is the carrier concentration, C_{ox} is the oxide capacitance, q is the electrical charge, V_{BG} is the back-gate voltage and V_T is the threshold voltage, which is extracted by the linear interpolation method.

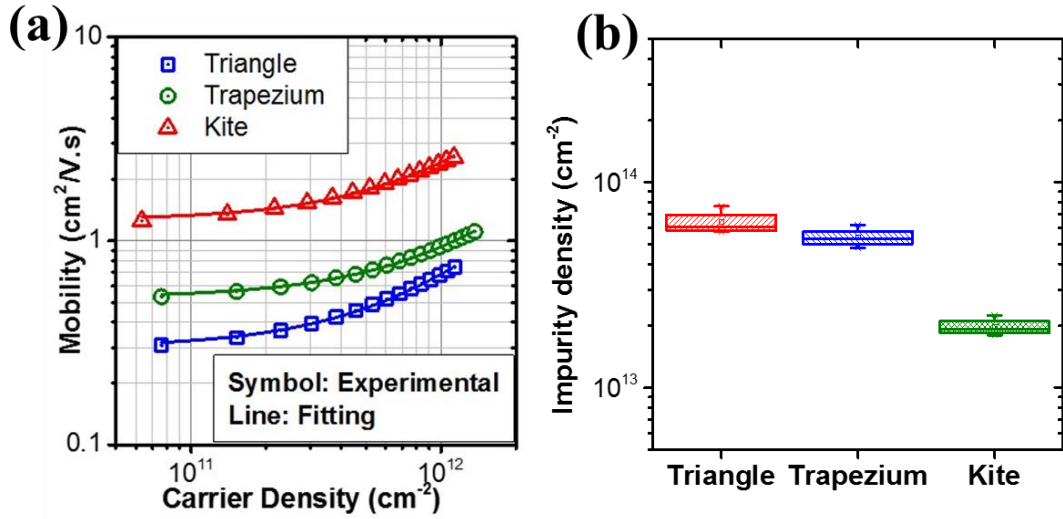


Figure 3: Mobility versus carrier density extracted from the Triangle, Trapezium and Kite. On the right the unintentional impurity concentration for the three devices.

From Figure 3a there is no degradation at high carrier concentration. Due to the low back-gate voltage applied (maximum value is 7.5 V) and the thick oxide (85 nm of SiO₂) the low vertical field might be too low to cause a degradation. Also, typical Mobility versus carrier density/gate voltages, are usually characterised by a peak and then a decrease in mobility. This is not seen here because of the low voltage applied, therefore the actual mobility is likely higher. In addition, there is another factor which affects the calculation of the field effect mobility. The calculation in Equation (1) assumes no source and drain contact resistance, so that the applied voltage V_{DS} drops entirely across the conducting MoS₂ channel from source to drain. The presence of source and drain series resistance results in a channel voltage drop $V_{CH} < V_{DS}$. As a result, the electron field effect mobility values in Figure 3 (a) represent the lower limit of the actual electron mobility in the MoS₂.

Ma and Jena⁹² reported a systematic study on carrier transport of 2D crystals, which are found to be highly dependent on the unintentional impurity density and the dielectric environment, which will be discussed in the next section. In particular, the mobility versus electron density, for low carrier density, follows the relationship:

$$\mu_{CI} \cong \frac{3500}{N_{CI}/10^{11} \text{ cm}^{-2}} [A_{CI} + (\frac{n_e}{10^{13} \text{ cm}^{-2}})^{1.2}] \text{ cm}^2/\text{V.s} \quad (3)$$

Where μ_{CI} is the mobility, N_{CI} is the unintentional impurity concentration, A_{CI} is a fitting parameter that depends on the dielectric environment and will be discussed in the next section. Considering that n_e can be evaluated experimentally, the unintentional impurity concentration can be extracted by fitting the equation with the electron mobility of the devices introduced before. From Ma and Jena⁹² fitted data show an unintentional impurity concentration of 10^{13} cm^{-2} , while Mori et al.¹⁹⁶, which implemented this same method, found different levels of unintentional impurity concentration (10^{11} and 10^{13} cm^{-2}), due to the high variability of TMDs.

Figure 3a shows the excellent fitting of the experimental mobility with Equation 1. The results of the fitting are shown in Figure 3b, which shows the unintentional impurity concentration level for each device. Even if a lot of factors can affect the parameter extractions, as widely said before, the unintentional impurity concentration level for all the device is on average $4 \times 10^{13} \text{ cm}^{-2}$ for nominally un-doped samples, which carrier concentration is expected to be in the 10^{17} cm^{-3} range or lower.¹⁹⁷

In order to confirm the extraction carried out for the Kite, the Triangle and the Trapezium, another exfoliation was done of Nb-doped MoS_2 , following the same process steps as the previous devices. The doping level for Nb-doped the crystal was

found to be in the range 4.2×10^{19} - $7.4 \times 10^{19} \text{ cm}^{-3}$ from Hall measurements.^{197, 198} In this case the mobility should as well be limited by charge scattering, therefore the unintentional impurity extraction should give a doping level (intentional impurity) in the high 10^{19} cm^{-3} range.

Figure 4a shows an optical picture of the experimental device. Labelled as C1, C2, C3, C4 and C5 the tracks that were contacted for the electrical measurements. Unfortunately some contacts were shorted during the electron beam lithography and were not used for the electrical characterisation.

Figure 4b shows the output characteristic for the contact C3 and C4 (C34) for a drain voltage of 0.5 V. From this curves it is possible to notice the advantages of using highly doped 2D-semiconductor with a Junctionless transistor configuration. Indeed, usually this device are limited by contact resistance, which even if still present in part, it is lowered by the high doping. On top of that, the current is usually higher with respect of nominally undoped flakes. As known, when a highly doped semiconductor is used in this Junctionless transistor configuration the thickness needs to be lower than the maximum depletion width in order to guarantee the full turn-off of the device.¹⁹⁹ Previous calculations have shown this value to be around 4.7 nm for this doping level.¹⁹⁸ From optical inspection the thickness of the flake is slightly higher, around 6 nm. This explains why the I_{ON}/I_{OFF} ratio of the device is around 10^4 , but with a thinner device it can be in principle much higher.

Figure 4c shows the mobility extracted from each contact configuration. The extraction followed the same steps as before. The mobility increases for low carrier density as for nominally undoped samples. For carrier concentrations higher than $2 \times 10^{12} \text{ cm}^{-2}$ the mobility starts decreasing, probably related to the high vertical electric

field. As will be discussed in later sections, mobility degradation might be possible for electrical fields higher than 10^8 V/m, which is the vertical field value at a concentration of 2×10^{12} cm⁻².

Considering the mobility at low carrier density ($< 2 \times 10^{12}$ cm⁻²) it is possible to extract the impurity concentration, which should be the doping level in this case, for the four contact configurations. Figure 4d shows the extracted intentional impurity concentration level. The contact C12 and C45 shows the same results, as for the contact C23 and C34. The difference between these devices is their length. C23 and C34 are longer (3.5 μ m) with respect of C12 and C45 (0.5 μ m). In this case the results for longer devices can be more reliable than the results for shorter devices. The fact that there is a high doping concentration means that the contact resistance of the device is lower than usual, as well as the resistance of the semiconductor. However, shorter devices might be dominated by contact resistance. Therefore, the results for longer devices (C23 and C34) might be more reliable than the results for shorter devices (C12 and C45).

Considering the intentional impurity concentration extracted for C23 and C34 at 25 °C, the average value is 8.75×10^{13} cm⁻². Considering a thickness of 6 nm, the intentional impurity concentration is 1.45×10^{20} cm⁻³. This value is slightly higher than the actual doping concentration measured by Hall effect 2×10^{19} - 7.4×10^{19} cm⁻³, but supports the approach used to extract the impurity concentration in non-intentionally doped MoS₂ samples.

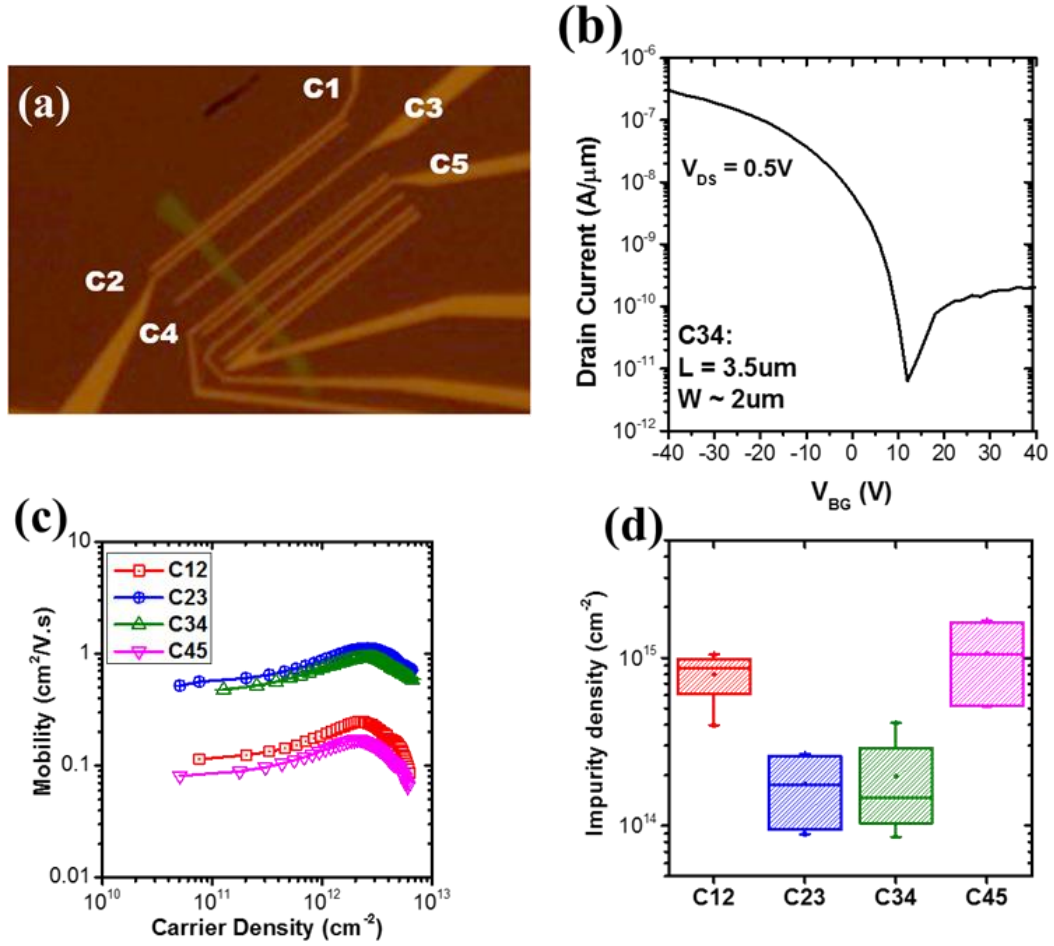


Figure 4: (a) Optical picture of a thin Nb-doped MoS₂ flake. The contacts used for electrical characterization are labelled. (b) Transfer characteristics between the contacts C3 and C4 at $V_{DS}=0.5V$. (c) Mobility versus carrier concentration extracted for each contact. (d) Extracted unintentional impurity concentration from each contact, as labelled.

The level of unintentional impurity found for the nominally undoped devices ($4 \times 10^{13} \text{ cm}^{-2}$) are significantly higher with respect of what is required by Si-based integrated circuit industry. In particular structural defects are requested to be below 0.008 cm^{-2} and impurities less than $5 \times 10^{10} \text{ cm}^{-2}$.¹⁰⁹ Structural defects of MoS₂ are outside the aim of this study, but were widely discussed in literature.

In order to confirm the high intentional impurity in the Nb-doped samples and the unintentional impurity concentration in the nominally undoped MoS₂, SIMS analysis was carried out on a series of different crystals and the results are reported in

Figure 5. The analysis was based on MoS₂, natural and synthetic, nominally doped and undoped. MoSe₂, MoTe₂, WSe₂ and HfSe₂. H, C, O, F and Sb were collected as negative ions while sputtering with a Cs⁺ beam. Na, Cr, Zr and Nb were collected as positive ions while sputtering with a O₂⁺ beam. Unfortunately, no direct comparison on the yields can be made in the figure between the different elements, but qualitatively comparisons can be made. In order to make a quantitative comparison a yield normalization of all the species to the yields of common matrix elements is needed. In our case, the yields in MoS₂, MoSe₂ and MoTe₂ have been normalized to the Mo yield, while yields in WSe₂ and HfSe₂ have been normalised to the Se yield collected in the MoSe₂ sample. This provides a way to qualitatively compare the two subsets of samples. The yields of the common matrix elements do not vary much between the different samples, supporting the reliability of the method. The exception is the WSe₂ sample analysed with Cs (H, C, O, F and Sb elements), where the normalisation has been as large as a factor of x17, thus in this sample errors on H, C, O, F and Sb might be larger. In general, the natural sample contains the highest levels of H, C and O contaminations, in particular for H and C. C contamination seems to differ significantly between the different synthetically grown samples. The Nb doping can be clearly seen in the intentionally doped synthetically-grown MoS₂ samples. Nonetheless, some Nb seems to be present in both WSe₂ and HfSe₂ samples. Na and Cr seem to be present only in synthetically grown sample and, particularly for Cr, there seems to be some correlation with doping. A clear isotope fingerprint of Zr contamination is found in the HfSe₂ sample.

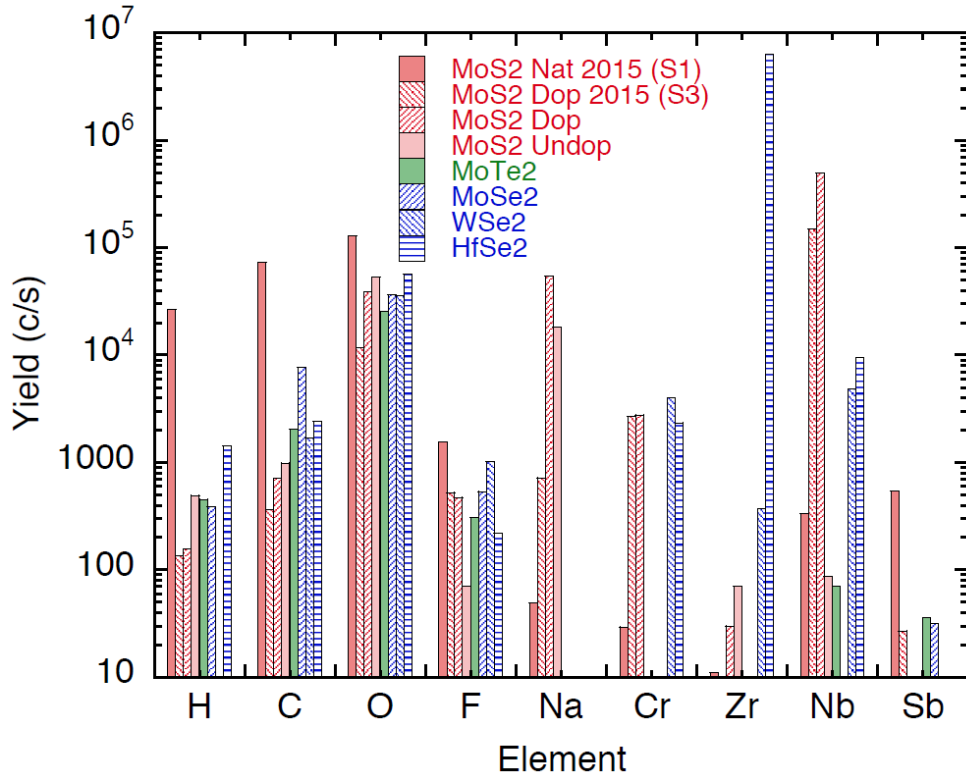


Figure 5: SIMS analysis carried out on a range of different TMD crystals.

3.4.2 Effect of the dielectric environment

The dielectric environment also plays an important role in the electron transport of thin semiconductors. The Coulomb potentials inside a thin semiconductor can be modified by the dielectric environment. As well, electrons in the semiconductors can excite polar-optical-phonon modes in the dielectrics, which become stronger for thinner materials. It is well known that high- k are beneficial for FET applications (i.e.: better electrostatic). Nonetheless, carrier transport can be severely degraded. Ab-initio calculations for monolayer MoS₂ have shown that high- k dielectric degrades mobility because of smaller surface-optical phonon energies, which can be easily excited and cause scattering in the thin material.⁹² In order to extract the best performance from 2D-semiconductor is necessary to find a balance

between high k-values, low surface optical phonon energies (and so lower surface optical phonon scattering) and as well screening of charged impurities.

In order to study the effect of the substrate through the same fitting process used before, other MoS₂ flakes were exfoliated on different oxides: 270 nm wet grown SiO₂ and 27 nm of ALD Al₂O₃. The fabrication steps are similar than the previous, with the only exception of the lithography, UV-lithography instead of e-beam lithography. The other main difference is that the contact length is not specified as it was for the metal tracks with the other devices. However, the contact area is large enough to guarantee an adequate carrier injection from the semiconductor to the metal. The channel length was defined by mask used for the lithography process and it was ~5 μm, as shown in Figure 6a. Figure 6b,c and d show typical IV curves for devices exfoliated on 27 nm of Al₂O₃, 85 nm of dry thermal SiO₂ and 270 nm of wet thermal SiO₂ respectively. The transfer characteristics are fairly similar between each other. The major differences are related to the wider hysteresis in the dry thermal SiO₂.

Mobility values were extracted and fitted by Equation 3 as before:

$$\mu_{CI} \cong \frac{3500}{N_{CI}/10^{11} \text{ cm}^{-2}} \left[A_{CI} + \left(\frac{n_e}{10^{13} \text{ cm}^{-2}} \right)^{1.2} \right] \text{ cm}^2/\text{V.s} \quad (3)$$

In this section we will focus on the fitting parameter A_{CI} instead of the impurity concentration, which is related to the dielectric environment.

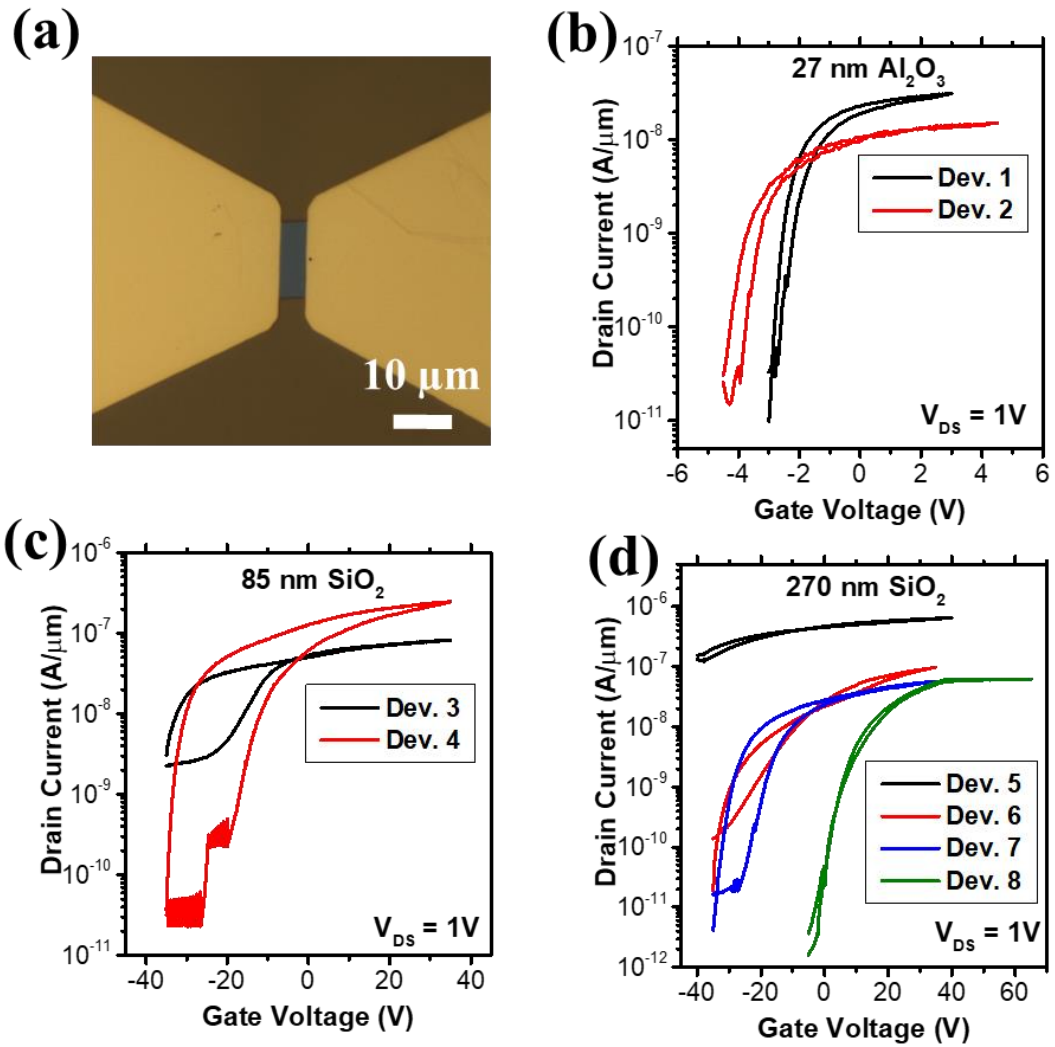


Figure 6: (a) Optical picture of a typical back-gated device structure. Transfer characteristics for the devices (dev.) exfoliated on (b) 27 nm of Al₂O₃, (c) 85 nm of dry thermal SiO₂ and (d) on 270 nm wet thermal SiO₂ at a drain voltage of 1V. The devices were numbered to distinguish them.

Figure 7a shows the value of A_{CI} for devices fabricated in parallel but exfoliated on different substrates. Even if there is an error bar associated with the two sets of extractions, there is a clear difference between the two substrates. The average value is 0.079 for Al₂O₃-air and 0.04 for SiO₂-air. The fact that the parameter is different is a reflection of the effect of the substrate on the material itself. Even if the original fitting was made for monolayer MoS₂, while these flakes are in the 6-8 layers

range, the results are still close. The value from the reference is almost 0.075 and 0.036 for Al₂O₃-air and SiO₂-air respectively.

Even if this is seen with A_{CI} the results are different for N_{CI}. The unintentional impurity concentration extracted for the SiO₂-air devices is $\cong 4.3 \times 10^{12} \text{ cm}^{-2}$, while the one extracted for the Al₂O₃-air devices is $\cong 5.5 \times 10^{13} \text{ cm}^{-2}$. Considering that the flakes were exfoliated from the same bulk materials the difference is related to the different substrates. This effect might be related to the different growth techniques used for the two substrates. The Al₂O₃ substrates might be affected by fixed charges, which can act similarly to charged impurity centres for thin 2D-semiconductors. For this reason the mobility of the devices fabricated on Al₂O₃ are slightly lower than the mobility values extracted from devices fabricated on SiO₂ (not shown).

The same extraction was repeated for the Kite, The Triangle and the Trapezium. With respect of the previous set of samples the dielectric is the same (SiO₂-air), while the difference is only related to the thickness (from 7 to 3 layers). The values for A_{CI} are reported in Figure 7. The average value at room temperature is 0.065. Even if this is slightly higher than the value reported it is important to consider that the top surface of the devices is exposed to air, which effectively change the top environment of the device.

Lastly, Figure 7a shows also the parameter extracted from the 9-layers Nb-doped sample. The average value at room temperature is 0.15. With respect of the last samples considered not only this sample is slightly thicker, but also highly doped. The high doping might be the main reason of this behaviour, due to different charge screening from the surrounding dielectric environment. In order to understand if this

value is related to thickness, substrate or doping concentration more experiments might be needed. Finally, Figure 7b shows the relationship between A_{CI} and the dielectric constant as reported in literature and as extracted here experimentally. Overall, there is a good agreement considering that the model was developed for monolayer MoS₂, which due to the high contact resistance are difficult to realize experimentally. Nevertheless, the effect from different substrates is clear even if thin MoS₂ is considered instead of the monolayer.

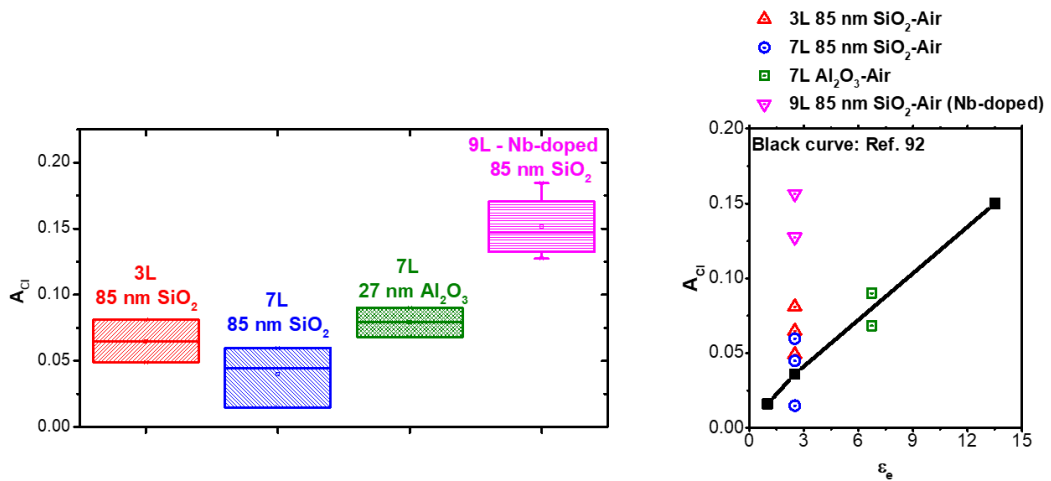


Figure 7: (a) Value of the parameter A_{CI} with respect of different dielectric environment, MoS₂ thickness and doping. (b) Comparison of the parameter A_{CI} varying the dielectric with respect of the theoretical reference.

These data consider the mobility in the low-field regime, when the mobility is highly dependent on the screening of impurity concentration by the dielectric environment. Another effect that can help in the choice of the optimal dielectric environment is the degradation of mobility at high field. The mobility degradation model reported for MoS₂ due to high vertical electric field depends on an empirical mobility model developed for Si MOSFETs.^{200, 201} It considers the mobility

degradation observed at the HfO₂-semiconductor interface,²⁰² which was attributed to remote phonon scattering:

$$\mu_{rps} = \frac{\mu_{rps0}}{\left(\frac{F_{\perp}}{10^6 V/cm}\right)^{\gamma_1} \left(\frac{T}{300K}\right)^{\gamma_2}} \quad (4)$$

where μ_{rps0} , γ_1 and γ_2 are fitting parameters and F_{\perp} is the actual vertical field. T is the temperature. Considering a fixed temperature of 300 K and different substrates it is possible to extract the dependency of γ_1 with respect of the dielectric environment.

Figure 8a shows the mobility extracted experimentally from the devices introduced before. The degradation starts in the range $2-4 \times 10^7$ V/m, consistent with previous experiments.²⁰³ The degradation part of the curve is fitted by Equation 4 and it clearly matches with the experiments. The resulting fitting parameters are μ_{rps0} and γ_1 . The former is a fitting parameter that depends on the mobility value at the beginning of the high-field degradation, then it can depend on other factors, as unintentional impurity concentration. The latter depends instead on the rate at which the mobility decreases at high field. Even if the mobility is limited by other factors (so μ_{rps0} is different), the mobility degradation rate is a function of the dielectric, because of surface roughness and optical phonon scattering. Figure 8b shows the dependency of γ_1 with respect of the gate dielectric (the data at for HfO₂ ($\epsilon \sim 19$) refer to ref. ^{30, 200, 204}, while the red data are from ref. ²⁰³). The dashed line was added to help the eye. Considering the data extracted from this work and published results from literature, the relation γ_1 - ϵ looks clearer and shows a minimum value between 6 and 11. A lower value of γ_1 means a lower degradation effect at high electric field. This optimal range

was also found by experimental and theoretical calculations. Back-gated MoS₂ FET showed higher mobility using AlN as a dielectric ($\epsilon \sim 8$) and all-nitride environment FETs, using h-BN and AlN showed the best performance.²⁰³ DFT calculations showed a similar trend.¹¹¹ In particular, mobility tends to increase from low k material to the optimal range 8-11 because of screening of charged impurities. At higher k values mobility decreases because of the smaller surface optical phonon energies, and so increase scattering.

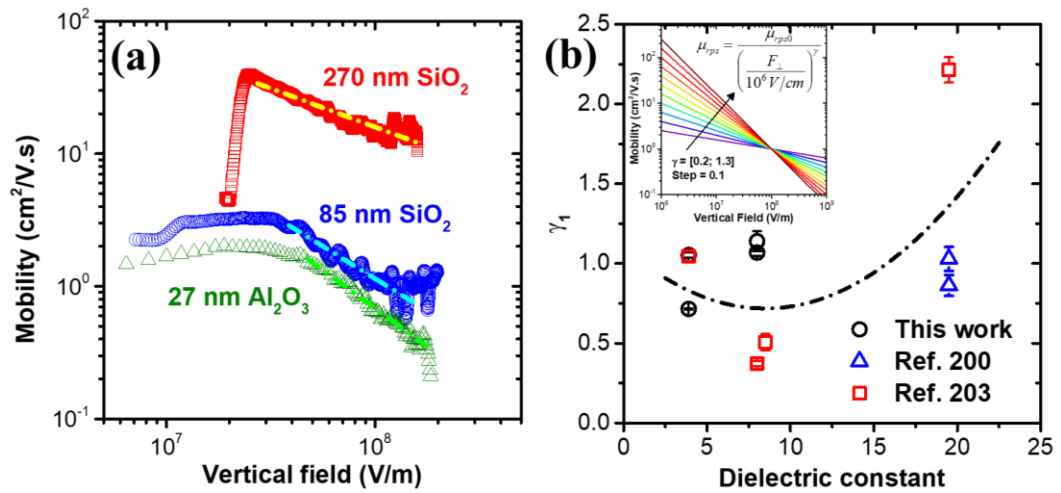


Figure 8: (a) Mobility extracted from experimental devices considering different substrates. The dotted line refers to the fitting with Equation 4. (b) Trend of γ_1 with respect of the dielectric constant of the gate dielectric. Inset: mobility degradation at high vertical field for increasing value of γ_1 .

3.5 DISCUSSION

Overall, there is an enormous difference between industry constraints and TMDs. As known, in order to properly extract the characteristics of semiconductors in general it is important to keep low the levels of impurities. Specifically because of their low thickness, the effects of contaminants can be particularly critical for thin 2D-Semiconductors.²⁰⁵ Indeed, it was shown how different dielectric environment can

affect the mobility of the material, due to the lower effects of long-range Coulomb interaction. The results showed here for MoS₂ are most likely valid for other type of TMDs or maybe similar 2D materials. In the case of this study the electron mobility at low carrier concentration was limited by the high impurity concentration, which masks the potential phonon limited mobility of MoS₂. At higher carrier concentration the effects of impurity might be less effective, and mobility degradation can come from surface roughness²⁰⁶ or remote phonon scattering.²⁰⁷

Often are also reported field-effect devices with “unknown doping concentration”,²⁰⁸ which can be probably related to impurities acting as dopants. A more detailed quantitatively analysis by ICMPS showed that the concentration of several elements were above 10¹³ cm⁻², for both geological and synthetic MoS₂.⁹⁰ A similar study conducted on WSe₂ showed lower impurity concentration,¹⁹² closer to the upper limit required by Si-based IC technology. Still, the intrinsic electronic properties of the material were strongly influenced by unintentional impurities.

One solution might be the introduction of a suitable dielectric environment capable of screening such impurities. As seen, the variation of the dielectric environment has a certain impact on the parameters extracted, confirming the theoretical model developed for monolayer MoS₂. Nevertheless, is still unclear how much this will affect the mobility due to the inability to test pure materials at present.

Also, even if it is important to compare TMDs with Silicon-based devices to benchmark their behaviour and potential, the comparison is not truly fair. Silicon is a mature semiconductor material, where unintentional impurities have been controlled to levels < 5×10¹⁰ cm⁻³, and the effect of substitutional doping and strain are well understood both theoretically and experimentally. Several groups are working on

doping techniques and simulation studies on how strain affects TMDs. These two techniques are normally used in industry for Silicon in order to obtain a low contact resistance and higher mobility, and stable doping and controlled strain are yet to be achieved for TMD based semiconductors. Generally, the immaturity of 2D-Semiconductor is due to the early stage of their research. Air stability, contact resistance and impurities, are some of the key challenges for the real application of these material, but with a large-area growth of higher quality material, most of these challenges can be opportunely studied and overcome as it happened at the early years of Silicon.

3.6 CONCLUSIONS

In this work, back-gated flakes of MoS₂ were electrically characterised for the main purpose of understanding the effect of impurity concentration and dielectric environment on the extracted field-effect mobility. The performance of the devices in terms of on/off ratio, drive current and mobility values extracted are comparable to other publications for back-gated MoS₂ MOSFETs. Through a fitting process of the field-effect mobility, impurity concentration was extracted for different devices, considering variation of dielectric environment, thickness and doping concentration. It was found that the unintentional impurity concentration is so high that it can be the limiting factor of electron mobility of the flakes studied to date. The impurity concentration was later confirmed with SIMS analysis in several TMD crystals. One solution might rely on the use of low-k dielectric, but the material system might be right now too immature to show this behaviour experimentally.

Chapter 4: CONTACT RESISTANCE STUDY OF HIGHLY DOPED P-TYPE MoS₂

This chapter is adapted from the following conference:

Mirabelli, G.; Duffy, R.; Hurley, P. K.; Monaghan, S.; Cherkaoui, K.; Schmidt, M.; Sheehan, B.; Povey, I. M.; McCarthy, M.; Nagle, R.; Bell, A., Mo-Based Transition-Metal-Dichalcogenide Junctionless Field-Effect-Transistors. Meeting Abstracts 2016, MA2016-01 (26), 1289-1289.

4.1 INTRODUCTION

Contact resistance is one of the major bottlenecks of TMD-based devices and for this material to be competitive with other semiconductors an analysis as well as possible solutions are necessary. The first part of the chapter deals with the electrical characterization of MoS₂ samples with high p-type levels of intentional impurities, $\sim 3 \times 10^{19} \text{ cm}^{-3}$ measured by Hall effect.²⁰⁹ These results will be compared with a wide range of doping and process optimization techniques used to improve the metal-TMD interface to achieve a low contact resistance. The second section of the chapter describes the use of TCAD modelling to extract basic electrical properties to understand which device architecture can be more useful for ultra-scaled devices.

4.2 EXPERIMENTAL

Mechanical exfoliation with scotch tape was used to obtain thin flakes from an intentionally p-type doped MoS₂ crystal. The flakes were transferred onto a substrate of 85 nm of SiO₂ and a highly p-type doped Si handle wafer. Ti/Au or Ni/Au (5/45 nm) metal contact pads and electrodes were defined by electron-beam lithography, followed by metal evaporation and a lift off process. 20 kV beam exposures were performed with a Raith e-beam lithography tool. For electrical characterization, the B1500 Keysight device parameter analyser was used. The morphologies of the TMD sample surfaces were investigated using a FEI Quanta 650 SEM in high-vacuum.

4.3 DEVICE FABRICATION

Figure 1a shows a SEM image of one of the devices studied in this work. Figure 1b shows the Atomic Force microscopy image of the device in Figure 1a. The

white line defines the region from where the thickness is extracted. The inset of Figure 1b shows the thickness extracted (~17 nm).

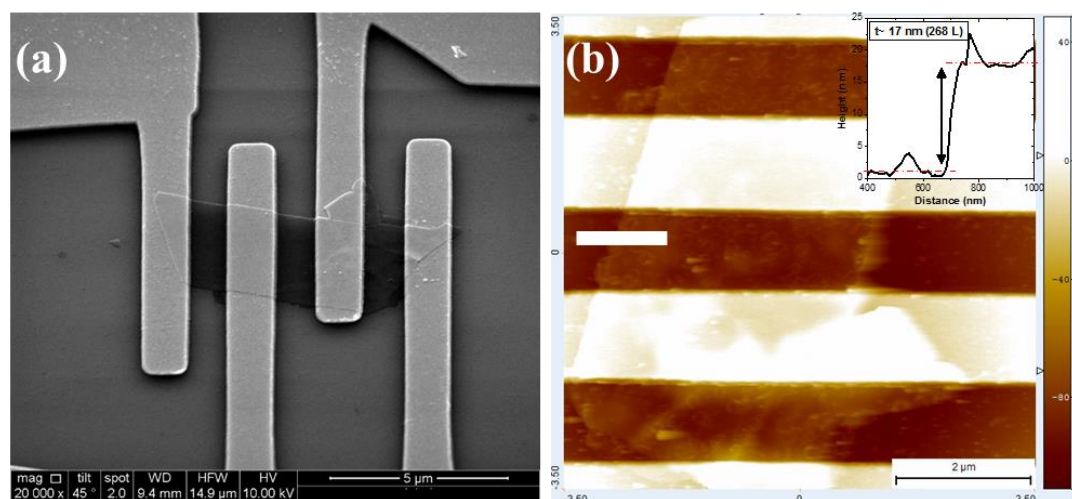


Figure 1: (a) SEM image of a typical contacted flake. (b) Representative AFM image of the same flake in (a). The white bar denotes where the cross-section was taken from. Inset: cross-section of the flake with its thickness (~17 nm).

4.4 ELECTRICAL CHARACTERISATION

Figure 2a shows a schematic of the four-point probe setup used in this work. A constant current is forced through the two most outer electrodes and the voltage drop across the inner electrodes is measured. Considering this voltage drop, it is possible to measure the real resistance of the semiconductor, without the effect on the contact resistance. Measuring the inner electrodes in a two-point probe setup, it is possible to extract the contact resistance as well. Figure 2b shows an example of this kind of measurements. A constant current of 1 nA is set between the outer electrodes and the voltage drop between the two inner electrodes is measured. This is then divided by the constant current to obtain the resistance of the semiconductor (“4-point-probes” in the plot). A two-probe measurement is repeated to obtain the total resistance of both the semiconductor and the contacts (“2-probes” in the plot). The difference between the total resistance and the semiconductor resistance will give the contact

resistance (“ R_C ”). Figure 2c shows the transfer characteristic of the device measured in Figure 2b with and without the effect of contact resistance.

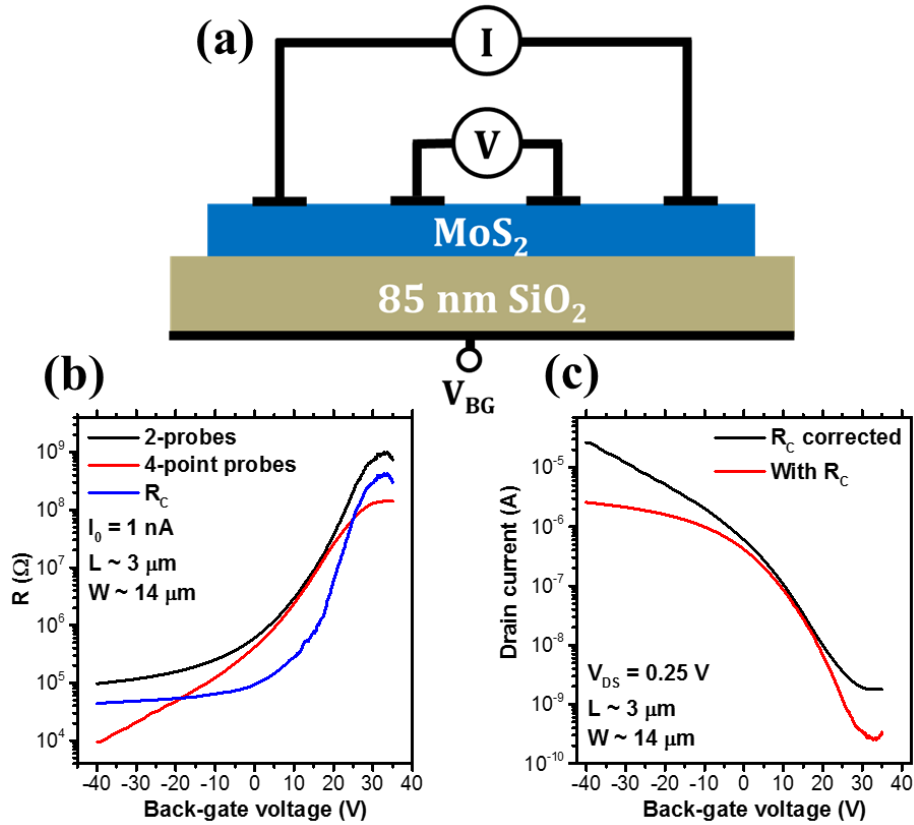


Figure 2: (a) Schematic of the device architecture used in this work. The external metal contacts are used to force a current in the device. Considering then the voltage drop across the two inner contacts, the resistance of the contact is extracted. (b) Example of 2-probe measurements (across the two inner pads), 4-point probe measurements and the extracted contact resistance. (c) Transfer characteristic of the same device from 2-point probe measurement (with R_C) and without the effect of R_C .

4.5 DOPING EXTRACTION

An important characteristic of the devices measured so far is their high doping concentration, as widely said, but it is necessary to have an idea of the actual doping concentration. Because of this, most of the transfer characteristic do not have a clear OFF region. In order to have a completely turn off the transistor it is necessary that the thickness of the channel is less than its maximum depletion width:

$$W_{DM} = 2 \sqrt{\frac{\epsilon k_B T \ln\left(\frac{N_A}{n_i}\right)}{q^2 N_A}} \quad (1)$$

if the flake is thicker than W_{DM} there will be a shunt current (I_{SHUNT}), which is equal to:

$$I_{SHUNT} = \mu_p \frac{W}{L} V_{DS} q N_A (t - W_{DM}) \quad (2)$$

considering these two equations a doping concentration of $\sim 3.4 \times 10^{19} \text{ cm}^{-3}$ was extracted from each transfer characteristic. This same doping level was similarly extracted in previous work²¹⁰ and from Hall measurements (Figure 3b).¹⁹⁷ The mobility extracted from the transfer characteristic is $\sim 7 \text{ cm}^2/\text{V}\cdot\text{s}$ after R_C correction from both Ti/Au and Ni/Au devices, which is again consistent with Hall measurements. This is another validation of the reliability of the contact resistance data extracted.

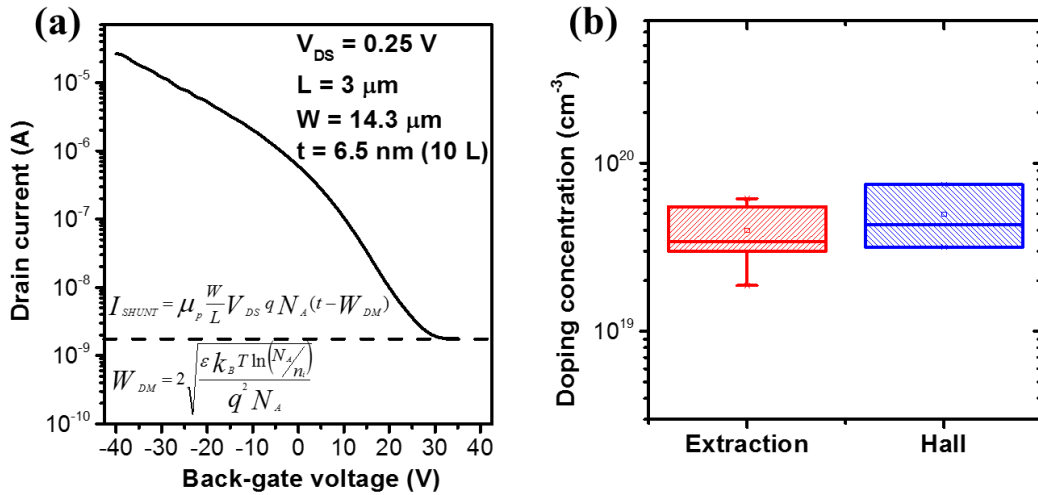


Figure 3: (a) Transfer characteristics of the 6.5 nm thick device showing the shunt current level, the equation for the shunt current and the equation for the maximum depletion width. (b) Average doping concentration from the extraction process using the transfer characteristics and the Hall measurements.

4.6 DISCUSSION

Figure 4 show the contact resistance versus MoS₂ thickness extracted from each device (Blue scatter data) compared with literature. Most of the data refer to Ni/Au metal contacts, while one of them was fabricated with Ti/Au contact. Although there is a slight difference in thickness it is clear that Ni is a far better contact than Ti. This can be related to a higher work-function of Ni. Nonetheless, it is clear that a doped contact reduces drastically the contact resistance with respect of the “as exfoliated” results introduced in chapter 1, where the contact was not optimised.¹²¹⁻¹³¹ These data clearly show the problem related to the metal-MoS₂ interface. Not only the contact resistance values are usually higher than what required by the IRDS, but also the data are characterized by a wide spread. All the other data present in the plot refer to works where the contacts was improved in a certain of ways. It is clear that all the treated contacts are well below the un-treated ones. These works were divided for clarity in three sections: contact optimization, process optimization and annealing step.

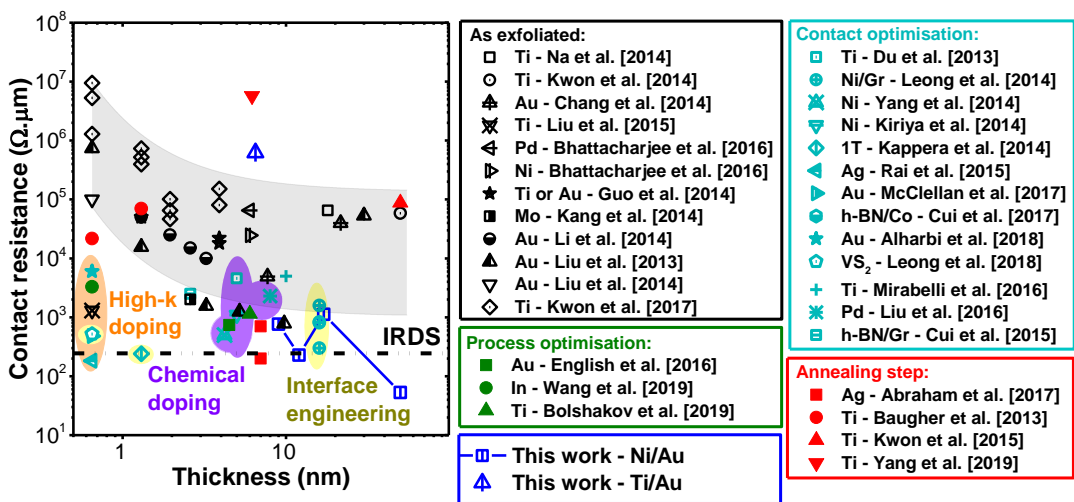


Figure 4: Contact resistance versus thickness of MoS₂ considering Ti/Au and Ni/Au contacts (Blue). The data are compared with other techniques to reduce contact resistance: high-*k* doping, chemical doping and interface engineering.

Contact optimization refers to those work where the interface metal-TMD is changed considering a buffer layer (interface engineering) or a certain doping technique (substitutional, chemical or high- k doping). Leong et al.²¹¹ and Cui et al.²¹², improved the contact resistance of MoS₂ by adding a layer of Ni/Graphene or h-BN. The additional spacer improves the effective contact resistance as it interacts with MoS₂, reducing its work function, and it disrupts the metal-TMD interaction that causes Fermi level pinning. Kappera et al.²¹³, instead changed the MoS₂ 2H-phase (semiconductive) to a 1T-phase (metallic) below the contact regions. Similarly, Leong et al.²¹⁴ used VS₂ (TMD with metallic phase) between MoS₂ and the metal contact to effectively improve the contact behavior. Another way to optimize the contact is by doping, as widely known already for 3D-semiconductors. A common technique is high- k doping. Theoretical and experimental works have shown that a doping can be mediated in MoS₂ by interfacial-oxygen-vacancies at the high- k /MoS₂ interface,²¹⁵ considering HfO₂ and Al₂O₃ on both exfoliated flakes²¹⁶ and CVD-grown monolayer MoS₂.^{217, 218} Another solution relies on the chemical doping, by which the TMD is generally immersed in a chemical solution that acts as a charge transfer donor/acceptor. Both p-²¹⁹ and n-type²²⁰⁻²²² doping were demonstrated. Similar results were obtained by substitutional doping,¹⁹⁸ in which the dopant is introduced during growth.

Process optimization refers to published works which aimed to improve or modify the fabrication process to reduce the contact resistance of the device. English et al.²²³ demonstrated the beneficial effects of Ultra-High Vacuum (UHV) instead of High-Vacuum (HV) during metal deposition because of a cleaner metal-MoS₂ interface. A similar result was confirmed by atomic resolution imaging using In as metal contact, which didn't have any reaction with MoS₂ and resulted in a sharp interface.²²⁴ A cleaner contact and a lower contact resistance was also achieved by O₂

plasma exposure at the contact, which can remove photoresist residues from the TMD surface, responsible for the Fermi level pinning at the contact.²²⁵

As a final point, “annealing step” in Figure 3 refers to work that incorporated an annealing step in order to reduce the impact of contact resistance. The annealing techniques used are different: vacuum,²²⁶ microwave,²²⁷ laser²²⁸ and forming gas anneal.²²⁹ Particularly low are the results from Abraham et al.,²²⁹ where the metal contact used for MoS₂ is silver. Previous works have shown that silver is a dopant for MoS₂ and can be diffused by an annealing step.^{230, 231} Therefore, the low contact resistance can be related to a dopant diffusion and activation below the contact region, forming a device similar to a classic MOSFET, with doped source and drain region. In addition, annealing step were also shown to be beneficial to reduce hysteresis²³² or density of interface traps.²³³ Nonetheless, although promising, the results are highly variable so a more systematic study considering different metals and thickness is necessary.

It is clear from Figure 4 that the contact resistance of the highly p-type doped MoS₂ samples analysed in this chapter are among the lowest values reported and very close to the IRDS requirements. In particular the data are similar to other doping techniques, confirming the utility and the necessity of a reliable doping method for 2D-semiconductors.

Figure 5a shows the transfer characteristic of each device studied in this work. The effect of contact resistance was eliminated considering the 4-point probe method as explained before. It is possible to notice a clear increment in the I_{ON}/I_{OFF} ratio considering thinner flakes. Figure 5b shows instead the transfer characteristic for different V_{DS} of a thinner MoS₂ Nb-doped flake (two probes, without using the 4-

probe method). Although it was not possible to remove the contribution of the contact it is clear that the I_{ON}/I_{OFF} ratio increments with decreasing thickness as expected, therefore behaving as a junctionless transistor.

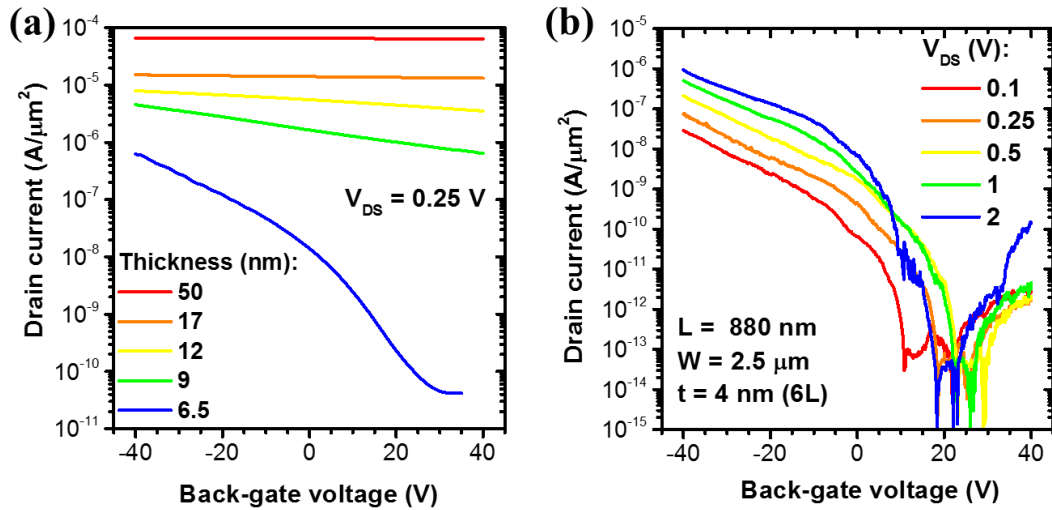


Figure 5: (a) Transfer characteristics of each device studied in this work. There is a clear dependence of the I_{ON}/I_{OFF} ratio with thickness because of the high doping concentration and the inability to completely deplete the channel. (b) Transfer characteristic of a thinner Nb-doped MoS₂, showing much higher defective behaviour.

To further compare the behaviour of MoS₂ p-type doped FETs it is necessary to consider the output characteristics of thinner flakes as well. Figure 6a and 6b compares the I_{DS} - V_{DS} curves for different back-gate voltages of the 12 nm and 5 nm thick MoS₂ devices respectively. While the curves in Figure 6a are linear, the curves in Figure 6b have more of an exponential behaviour, which means that the carrier transport mechanism is different. There are three main mechanisms that dominate carrier transports at the contacts. If a small Schottky barrier is present, then thermionic emission dominates the transport, and the I_{DS} - V_{DS} curve can be modelled with the Richardson-Schottky equation:

$$I_D \propto A \times T^2 \exp \left[\frac{-\phi_B + \sqrt{q^3 V_D / 4\pi\epsilon_0\epsilon_r d}}{k_b T} \right] \quad (3)$$

where V_D is the drain voltage, T is the temperature, ϕ_B is the Schottky barrier, q is the elementary charge, k_B is the Boltzmann constant, d is the width of the barrier, ϵ_0 and ϵ_r are the absolute dielectric constant and the dielectric constant of the semiconductor, respectively. Therefore, the plot of $\ln(I_D)$ against $V_D^{1/2}$ is expected to have a linear dependency. Instead, in case of a high and wide barrier the transport is described by the Fowler-Nordheim tunnelling:

$$I_D \propto V_D^2 \exp \left[\frac{-4d\sqrt{2m\phi_B^3}}{3\hbar q V_D} \right] \quad (4)$$

where m is the carrier effective mass and \hbar is the Plank constant. In this case $\ln(I_D/V_D^2)$ versus $1/V_D$ is expected to have a linear behaviour with a negative slope. If the barrier is instead thin enough for direct tunnelling, the curve is expected to have a logarithmic growth considering $\ln(I_D/V_D^2)$ versus $1/V_D$. Therefore a linear positive trend considering $\ln(I_D/V_D^2)$ versus $\ln(1/V_D)$.

Figure 6c shows the output characteristic of the 12 nm thick MoS₂ plotted as $\ln(I_D/V_D^2)$ versus $1/V_D$. Since they clearly show linear behaviour we can conclude that, as expected, this device is dominated by the resistance of the semiconductor and direct tunnelling model dominates at the contact. Instead Figure 6d shows the output characteristic of the 4 nm thick MoS₂ plotted as $\ln(I_D)$ versus $V_D^{1/2}$. Due to its linear behaviour, it is clear that a Schottky barrier is present and thermionic emission dominates the transport.

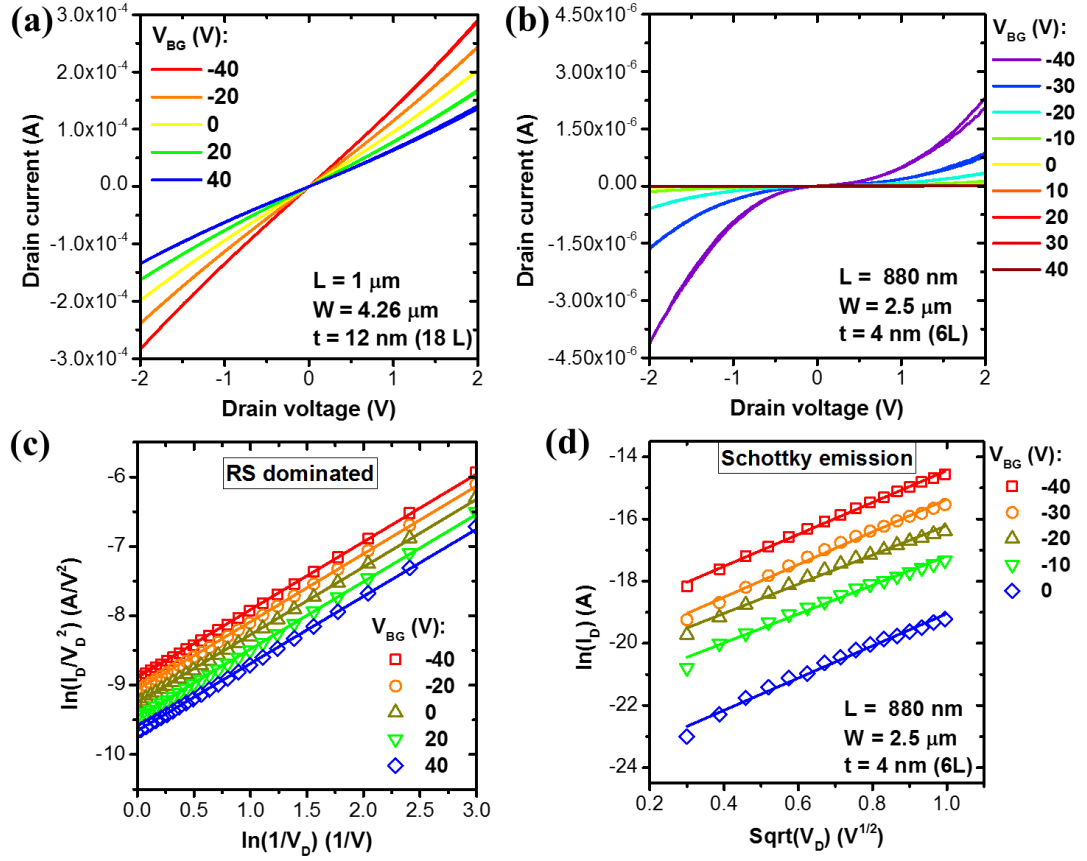


Figure 6: Output characteristics of the (a) 12 nm thick device and (b) 4 nm thick device. The output characteristic of the 12 nm thick device can be modelled considering direct tunnelling, which means that the behaviour is dominated by the resistance of the semiconductor (RS). Instead, the 4 nm thick sample can be modelled considering the Richardson-Schottky equation, pointing to a Schottky emission behaviour.

This same analysis was applied by Liu et al.²¹⁹ studying the contact behaviour of chemically doped MoS₂ transistors. In that case, a doped multilayer MoS₂ was dominated by Fowler-Nordheim tunnelling at small gate bias and direct tunnelling at higher gate bias. For the case of the 12 nm thick device we only see direct tunnelling, as there is almost no gate action, due to the high doping and thickness of the device. Instead, considering the 4 nm thick device, the behaviour is always fitted with a Schottky emission model because of the barrier present at the contacts.

Therefore, although there is a noticeable improvement of the contact behaviour for highly doped MoS₂, still there are some difficulties to appreciate this for thinner

devices. This can be related to the cleanliness of the contact. As said before, contact studies on MoS₂ devices have shown an O₂ plasma exposure of the contact area can remove unwanted PMMA residues. The AFM image in Figure 1b shows what are potentially photoresist residues on the MoS₂ surface and at the MoS₂-metal interface. In our work, thick devices don't seem to be affected by these residues, but thinner devices might be more sensitive. The higher sensitivity can be related to the effective contact area of the device, since the barrier height and width is set by the band alignment and doping level. When the MoS₂ thickness is higher than the maximum depletion width the effective contact area is the full metal area, as it can be accessed from below the contact in the quasi neutral region of the MoS₂. In the case of the fully depleted sample the contact area approximates to the product between the width of the device and the thickness of the MoS₂.

4.7 CONCLUSIONS

In conclusions, without any treatment of the metal-MoS₂ interface, device performances are usually poor and characterised by high variability. Among other techniques, high doping can be a solution in order to drastically reduce the contact resistance at the source/drain region. However, other process techniques, such as annealing treatment, surface cleaning, or chemical doping, are necessary in order to maintain a good contact behaviour at low thickness.

Chapter 5: EFFECTS OF ANNEALING TEMPERATURE AND AMBIENT ON METAL- PTSE₂ INTERFACE

This chapter is adapted from the following publications and conferences:

Mirabelli, G.; Walsh, L. A.; Gity, F.; Bhattacharjee, S.; Cullen, C. P.; Ó Coileáin, C.; Monaghan, S.; McEvoy, N.; Nagle, R.; Hurley, P. K.; Duffy, R., Effects of Annealing Temperature and Ambient on Metal/PtSe₂ Contact Alloy Formation. ACS Omega 2019, 4 (17), 17487-17493

Walsh, L. A.; **Mirabelli, G.;** Cullen, C. P.; Gity, F.; O’Coileain, C.; Monaghan, S.; Schmidt, M.; Nagle, R.; McEvoy, N.; Duffy, R.; Duesberg, G.; Hurley, P. K., Investigating contact resistance to PtSe₂ using forming gas annealing, WODIM, Berlin, 2018;

Mirabelli, G.; Walsh, L. A.; Gity, F.; Bhattacharjee, S.; Cullen, C. P.; Ó Coileáin, C.; Monaghan, S.; McEvoy, N.; Nagle, R.; Hurley, P. K.; Duffy, R., Effects of annealing temperature and ambient on metal-PtSe₂ contact alloy formation”, European Material Research Society, Nice, France, 2019;

5.1 INTRODUCTION

Although promising, the integration of TMDs with other semiconductors is still limited due to (1) the lack of low temperature and wafer-scale uniform growth processes and (2) due to the rather large Schottky barrier that usually characterizes the metal/TMD interface, which limits the device behaviour and masking their full potential.

The lowest values of contact resistance are usually related to high- k induced doping or interface engineering.²¹¹⁻²¹⁴ Another possible solution still mostly unexplored is the use of an opportune annealing step to modify the metal/TMD interface. Annealing is a common process step in the modern semiconductor industry. Laser annealing is used for Si and Ge to achieve highly doped and abrupt junctions.²³⁴ Additionally, annealing in forming gas has been used to reduce the density of fixed oxide charges and interface states at the Al₂O₃/InGaAs interface.²³⁵ Similarly, for 2D-semiconductors several publications have shown how different annealing steps can improve the performances of TMD-based devices. Vacuum annealing has been shown to reduce the concentration of surface contaminants.^{236, 237} Furthermore, annealing in an inert environment or forming gas can be beneficial in terms of reducing the density of interface states at the MoS₂-oxide interface.²³³ Annealing steps have also been shown to be valuable for the TMD/metal interface. Forming gas annealing (FGA) on graphene/MoS₂ contacts was shown to improve the contact resistance of the material system.²³⁸ Other annealing techniques, such as vacuum annealing,²²⁶ microwave annealing²²⁷ or short-term pulsed annealing,²²⁸ were also reported to be advantageous for the metal/MoS₂ interface. Nonetheless, the values are still far from the requirement of the IRDS roadmap, and the reaction metal-TMD upon annealing as well as the optimal annealing temperature range and ambient is still unclear.

In this chapter large area grown thin films of PtSe₂ are characterised considering different post-growth thermal treatments and their effects on the metal/TMD interface. PtSe₂ has attracted increasing interest over the last few years. Interestingly, it shows semi-metallic characteristics in its bulk form, while experiments have shown the opening of a bandgap for thicknesses lower than 3 nm.^{239, 240} Therefore, PtSe₂ has gained attention due to its potential application in electronics,²⁴¹ optoelectronics²⁴² and sensors.²⁴³ PtSe₂ is grown by thermally assisted conversion (TAC) which does not require a high thermal budget (max temperature of 400 °C). This makes the growth compatible with back-end-of-line processing and integration in modern technologies, as it respects the typical thermal budgets of the CMOS Industry (~450 °C).⁵¹⁻⁵³ This is in sharp contrast with TMD films grown by chemical vapour deposition, chemical vapor transport or molecular beam epitaxy.^{31, 32, 34, 244} The growth is not homogenous, and it is characterized mainly by triangular crystals that merge together after a sufficient growth time.^{35, 36, 38} Above this, the thermal budget of these processes is usually high to obtain a reaction of the pre-deposited film with the chalcogen, limiting their integration in modern CMOS technology.

The PtSe₂ was grown at 400 °C over a large area. Ti/Au and Ni/Au were used as metal contacts and circular transfer length method (c-TLM) structures were used to electrically characterize the metal/PtSe₂ interface and the PtSe₂ material itself. The samples were then annealed for 1 hour in a forming gas ambient (5/95% H₂/N₂) at different annealing temperatures: 150 °C, 250 °C and 350 °C. The same experiment was repeated in an inert environment (0/100% H₂/N₂). The electrical properties of the material were studied after each annealing step. The TMD-metal interface and alloy formation were studied and characterized by a combination of X-ray photoelectron

spectroscopy (XPS), Raman spectroscopy, energy-dispersive X-ray spectroscopy (EDX) and cross-sectional transmission electron microscopy (XTEM).

5.2 EXPERIMENTAL

All PtSe₂ samples were grown over large area using a TAC process.^{49, 50} Pt metal is evaporated onto a SiO₂/Si substrate. This was then converted in a furnace with a Se pressure of ~1 mbar at 400°C. The specifics of the growth are discussed in detail elsewhere.⁵⁰

Since the PtSe₂ samples come from the same growth run and are highly consistent, applying a similar FGA step allows the effect of the process on the material itself and the metal-TMD interface to be decoupled. c-TLM metal contacts were patterned using standard photolithography followed by e-beam evaporation of the metal and a lift-off process. For these devices the targeted thicknesses were 10/90 nm for both Ti/Au and Ni/Au at a background pressure of ~10⁻⁵ mbar. For the XPS samples the targeted thicknesses were 3 nm for both Ti and Ni. No Au was used in the XPS samples as it does not interface with the PtSe₂ film and the added metal thickness would exceed the photoelectron escape depth (of ~ 5nm). After an initial characterization each sample was cleaved into 3 pieces to maintain consistency. Forming gas anneals were performed at 150 °C, 250 °C and 350 °C for 1 hr using 5% H₂/ 95% N₂. The same annealing conditions were applied again in an inert environment (0% H₂/ 100% N₂).

XPS characterization was performed using monochromated Al K α X-rays from an Omicron XM1000 MkII X-ray source and Omicron EA125 hemispherical analyzer with ± 0.05 eV resolution. A take-off angle of 45°, acceptance angle of 8°, and pass energy of 15 eV were employed during spectral acquisition. The binding

energy scale was referenced to the adventitious carbon species in the C 1s core level (285.8 eV). Spectra were deconvolved using AAnalyzer,²⁴⁵ a curve fitting software.

For structural analysis, cross-section samples were obtained by using the Dual Beam Helios Nanolab 600i system from FEI, using a Ga ion beam. Layers of the protective material were used consisting of electron beam deposited C, Pt, and ion beam deposited C. Lamellas were thinned and polished at 30 kV 100 pA and 5 kV 47 pA, respectively. XTEM imaging was carried out using a JEOL 2100 HRTEM, operated at 200 kV in the bright field mode using a Gatan Double Tilt holder. EDX mapping was carried out using a Thermo Fisher scientific Titan Themis operated of 300kV in STEM mode using the Bruker superX Silicon Drift detector.

5.3 EXPERIMENTAL RESULTS

Figure 1 shows the process flow adopted to study the reaction of PtSe₂ after each annealing step. First, PtSe₂ (with an initial thickness of 1 nm) was grown on 4 different samples in a single growth run for high consistency. c-TLM structures were defined and the samples were then measured electrically. The presence of PtSe₂ was confirmed by Raman analysis.²⁴⁶

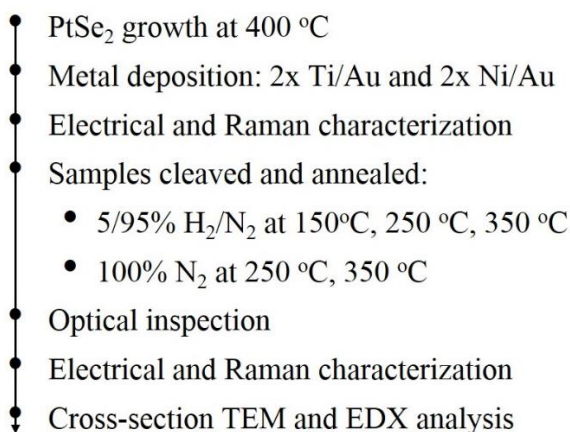


Figure 1: Experimental steps taken during this work.

Figures 2a and 2d show the optical microscope images of the contacted PtSe₂ with Ti and Ni contacts respectively before any annealing and no visible differences are present between the two samples. The samples then underwent different annealing steps. No obvious differences were found for the samples annealed in forming gas at 150 °C, as the temperature might have been too low to start any reactions. After annealing at 250 °C in forming or inert environment the Ti/Au sample did not show any appreciable differences from optical inspection (Figure 2b and c). On the contrary, the Ni/Au sample annealed at 250 °C in forming gas displayed what looks like an “alloy region” around the metal contacts (Figure 2e). This alloy region is less pronounced for the annealing at the same temperature in the inert environment (Figure 2f). It is noted that the reaction taking place between Ni and PtSe₂ is accelerated by the presence of hydrogen during the annealing. The 350 °C anneal in forming gas (pictures not shown), as later confirmed by electrical and Raman characterizations, resulted in a degradation of the PtSe₂. Considering that PtSe₂ is grown at a temperature of 400 °C, a forming gas anneal at 350 °C may be too harsh an environment for this

material, which highlights the importance of understanding the process window for optimal annealing temperature and its effects on the material properties.

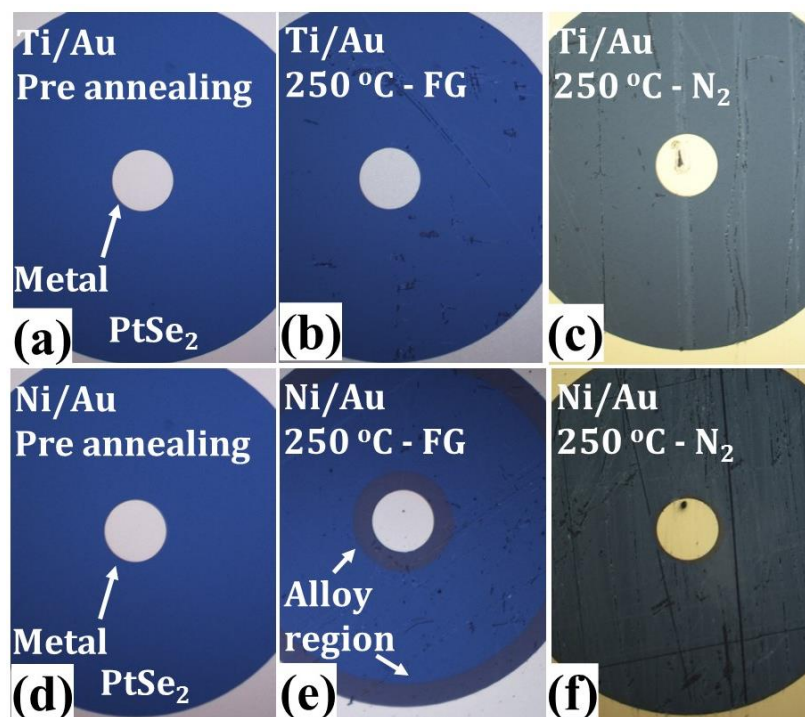


Figure 2: Optical microscope pictures of the larger c-TLM of PtSe₂ before annealing contacted with (a) Ti/Au and (b) Ni/Au. Same optical pictures repeated after annealing in forming gas (FG) and inert ambient at 250 °C for (b, c) Ti/Au and (e, f) Ni/Au respectively. The darker gold ring in (e) clearly shows the alloy region.

Figure 3 shows the electrical characterization carried out on each sample. Figure 3a shows representative current-voltage measurements on the Ni/Au samples considering a spacing of 43.5 μm . Although no appreciable differences are visible from optical inspection after a forming gas anneal at 150°C, the current decreases with respect to the pre-annealed case. On the contrary, considering the same forming gas environment but a temperature of 250 °C the current increases, indicating that a reaction or process occurred which reduced the PtSe₂ resistivity and/or metal-PtSe₂ contact resistance. Considering the results in Figure 3c, the PtSe₂ for the Ti/Au contacts, the forming gas anneal does not influence the PtSe₂ sheet resistance. These

combined results indicate that in the case of the Ni/PtSe₂ sample the forming gas anneal is reducing the resistance of the metal-PtSe₂ contact. Because the Ni diffusion/reaction with PtSe₂ changed the spacing of the structure, the results at 250 °C in forming gas were corrected, changing the value of the spacing of each structure with the actual channel length. The anneal at 250 °C in an inert environment and the anneal at 150 °C in forming gas resulted in a lower current. These two anneal conditions seem to provide similar results. Although one was done at a lower temperature, the presence of forming gas seems to have accelerated the reactions that took place. It is also important to consider that the 250 °C in the inert environment also resulted in an alloy region, although not as pronounced as the case in forming gas. On the contrary no alloy regions were found for the sample annealed at 150 °C in forming gas.

Figure 3b shows the total resistance versus spacing for the Ni-Au contacted PtSe₂ at each annealing step. It is clear that each annealing is affecting the electrical behavior of the device. Nonetheless, this analysis is problematic for the Ni/Au samples. Due to the presence of the alloy region, the fitting process is less reliable since the spacing of the structures change with the annealing condition. Future work may include linear TLMs with smaller dimensions for a more accurate parameter extraction. Figure 3c shows the same analysis for the Ti/Au sample for each annealing condition. No appreciable differences are present, and the trend remains quite similar, meaning that the film itself, as well as the PtSe₂-Ti interface, are not affected by any annealing steps.

Figure 3d shows the sheet resistance extracted from each measurement. The sheet resistance can be extracted from the Ti/Au measurements considering the c-TLM

theory.²⁴⁷ However, for the Ni/Au samples the total resistance was considered as the resistance of the PtSe₂ owing to the low contact resistance. The results for the Ti/Au contacts confirm what is seen in Figure 3b: the annealing temperature and conditions are not changing the metal-PtSe₂ interface or the PtSe₂ material itself. On the contrary, a much higher variation is seen for the Ni/Au samples, which can be related to the reaction between Ni and PtSe₂. Consider that, although obvious “alloy regions” are present from optical inspection it is possible that the Ni diffuses much further into the PtSe₂, than what is possible to see with an optical microscope.

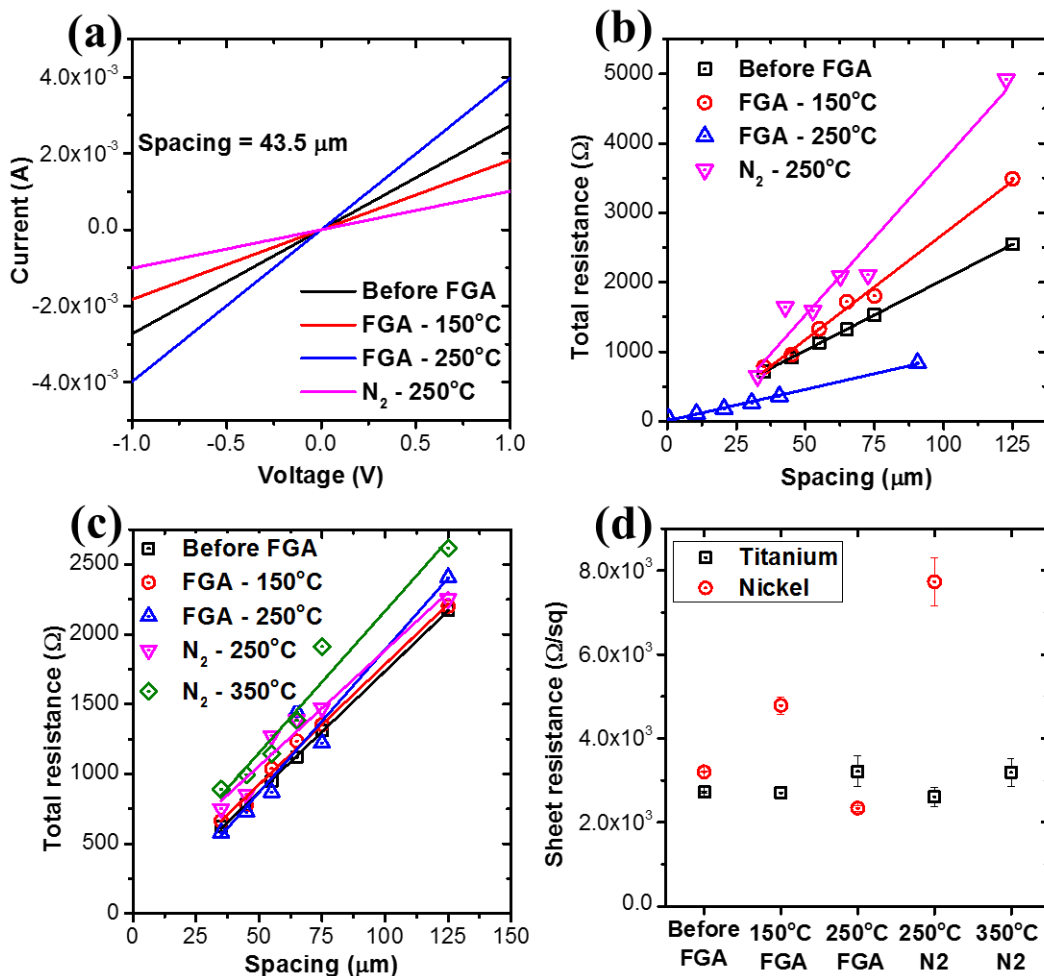


Figure 3: (a) Current-voltage measurements on the Ni/Au samples after each annealing step. (b) Total resistance versus spacing for the (b) Ni/Au and (c) Ti/Au contacted PtSe₂. (d) Extracted sheet resistance after each annealing step.

A Raman spectroscopy was then performed to confirm the integrity of the PtSe₂ and to probe the “alloy region” seen in the Ni/Au samples. The results are summarised in Table 1. In particular, the Raman signal was collected on the bare PtSe₂ and near the metal contact. For the Ti/Au sample the signal of PtSe₂ is always present, except for the 350 °C annealing in forming gas, which resulted in degradation of the PtSe₂ film. Similarly, for the Ni/Au sample a clear PtSe₂ signal is present up to 250 °C, in both forming and inert gas environment in the bare PtSe₂ regions (far from the metal contact). For the samples that showed an “alloy region” no PtSe₂ signal is present close to the metal contact, suggesting metal interdiffusion and alloying.

Table 1: Summary of the Raman analysis on the PtSe₂ samples after each annealing condition.

Annealing condition	Raman peaks of PtSe ₂	
	Ti/Au	Ni/Au
150 °C 5/95% H ₂ /N ₂	Present	Present
250 °C 5/95% H ₂ /N ₂	Present	Present, except in diffusion ring
350 °C 5/95% H ₂ /N ₂	Absent	Absent
250 °C 100% N ₂	Present	Present
350 °C 100% N ₂	Present	Absent

Figure 4 shows representative TEM images of the Ni/Au contacted PtSe₂ samples annealed at 250 °C in forming gas and in an inert environment. Figure 4a and 4b compare the PtSe₂ structure inside and outside of the alloy region, respectively. It is noted that the layered structure is present outside the alloy region, while it is not inside it. Similarly, Figure 4c and d show the PtSe₂ below the metal contact and outside of it, respectively. Again, the layered structure is not present below the metal contact

but is preserved outside of it. These representative images confirm the hypothesis. The diffusion ring seen from optical images is a result of Ni interdiffusing and alloying with the PtSe₂. This compound is not characterized by the same layered structure of PtSe₂, but it has the form of a 3D alloy. Also, although the alloy region around the contact is not present in the sample annealed at 250 °C in an inert environment, a similar reaction has taken place below the metal contact. Therefore, it can be concluded that the presence of hydrogen accelerates the reaction, and the Ni can react more readily with PtSe₂ away from the metal itself.

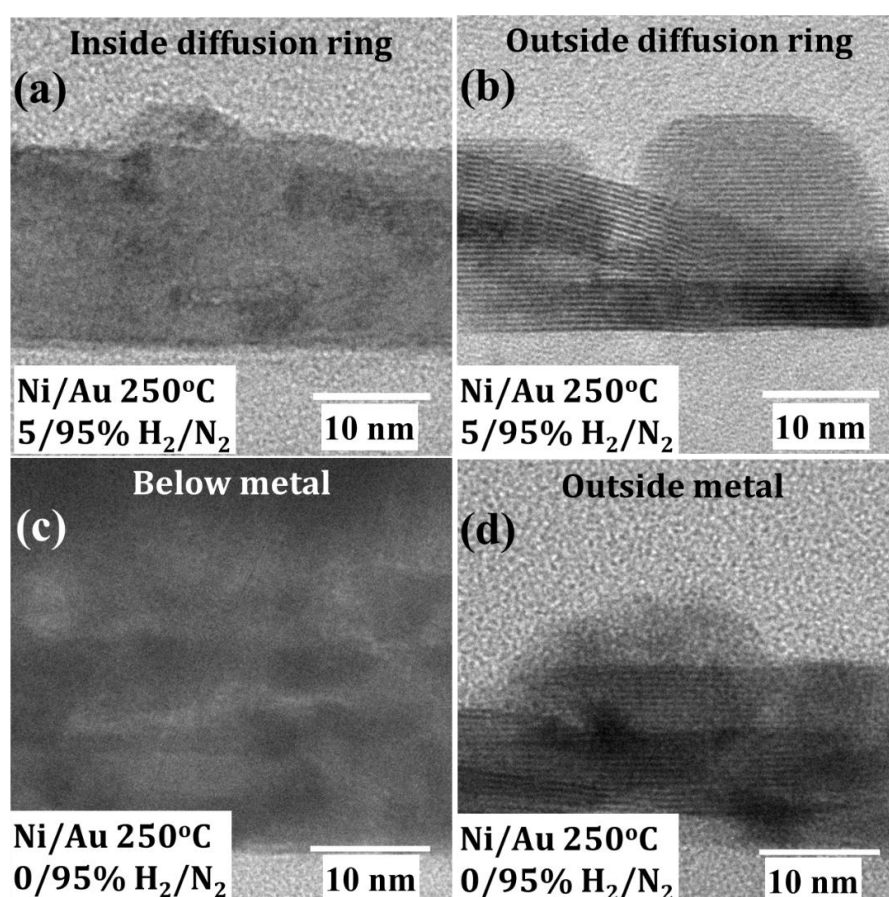


Figure 4: Representative cross-section TEM images of the PtSe₂ contacted with Ni/Au. (a) and (b) show the PtSe₂ after annealing in forming gas at 250 °C inside and outside the diffusion ring respectively. (c) and (d) show the PtSe₂ after annealing in inert environment at 250 °C below the metal contact and outside the metal contact respectively.

In order to explore the nature of the interdiffusional alloying observed an XPS was performed using near-identical samples. Figure 5 shows XPS spectra of the Pt 4*f* and Se 3*d* core levels of PtSe₂ before and after metal deposition, with no further annealing. No Au was used here as Au does not interface with the PtSe₂. The Pt 4*f* spectra for bare PtSe₂ (Figure 5a) shows the presence of two chemical states, both represented by a doublet, one related to PtSe₂ (72.15 eV) and another due to surface oxidation (PtO_x at 71.1 eV). The Se 3*d* spectra of the same sample (Figure 5c) show PtSe₂ and SeO_x features (53.55 eV and 54.25 eV, respectively), with the additional contribution of the Pt 5*p*_{3/2} (52.6 eV), which overlaps with the Se 3*d*.

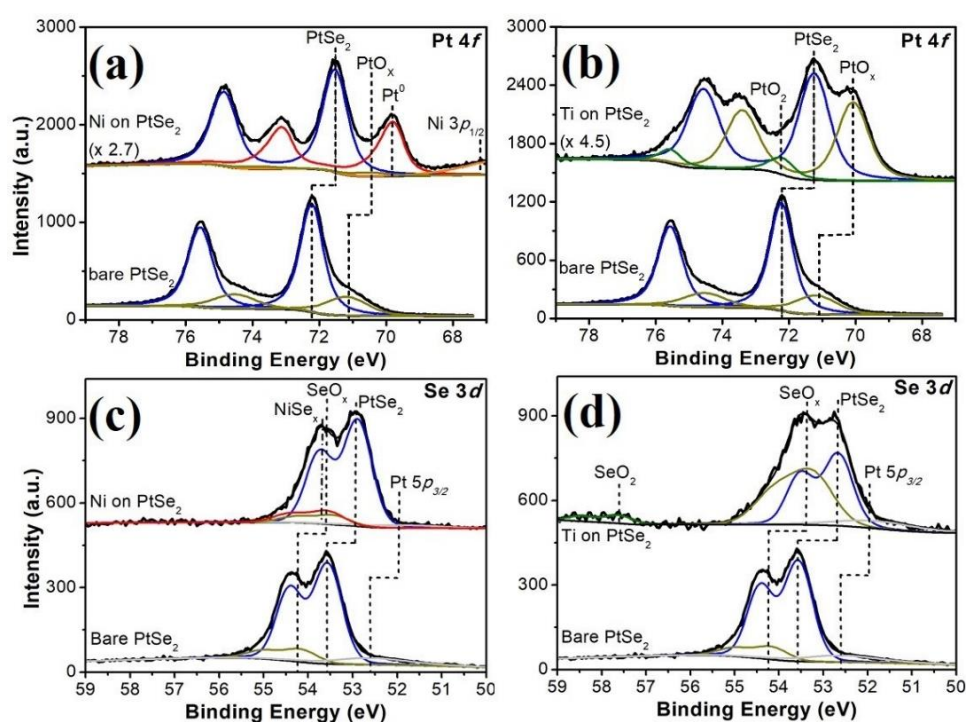


Figure 5: XPS spectra of (a), (b) Pt 4*f* and (c), (d) Se 3*d* core levels for PtSe₂ before and after Ni or Ti deposition.

Upon Ni deposition a significant change in the peak shape of the Pt 4*f* is observed, with the emergence of a feature at low binding energy (BE). This peak is at lower BE than PtO_x, consistent with metallic Pt (Pt₀). The Se 3*d* spectrum shows a

subtler change with broadening to higher BE, attributed to the possible formation of a Ni-Se compound (NiSe_x). The Ni 2*p* spectra are difficult to interpret due to the presence of several satellite features. Although a shift to higher BE is observed compared to a reference Ni film, which could be due to Ni oxidation or the reaction between Ni and another high electronegativity element such as Se. Taken together this suggests the reduction of PtSe₂ by Ni, resulting in NiSe_x formation, and Pt metal.

In the case of Ti, a much more subtle change in chemical state is observed. After Ti deposition, the PtO_x peak increases significantly and is accompanied by a higher BE feature consistent with PtO₂. The Se 3*d* also shows a significant increase in oxidation with an increase in SeO_x and the appearance of a higher BE SeO₂ peak. The Ti 2*p* spectra (not shown) show the complete conversion of Ti to TiO₂, which is expected due to the oxygen-gettering nature of Ti. The presence of excess oxygen in the TiO₂ film in turn oxidizes the underlying PtSe₂.

Lastly, to confirm the presence of Ni in the reacted region, EDX was conducted on the TEM cross-section lamellas prepared with the Ni/Au contacted devices before and after annealing at 250 °C in both forming gas and inert environment at 250 °C. Figure 6 shows the compositional analysis performed via scanning transmission electron microscopy (STEM) based energy dispersive x-ray spectroscopy (EDX). Figure 6a and 6f shows the high-angle annular dark-field images (HAADF) of the region under study, which is at the edge of the metal contact. Figure 6 b-d and g-j show the spectra for Au, Pt and Se. No significant interdiffusion is observed for these elements after annealing, and the mapping results are fairly similar. Considering that Au and Pt have a similar atomic weight, what would seem to be diffusion of Pt in Au is actually just an artefact from the EDX. This is not an issue as the focus is on the

behaviour of Ni with PtSe₂. Figures 6e and 6j show clear Ni diffusion upon annealing. Before annealing the Ni spectra is clearly confined between the PtSe₂ and the Au region. While after N₂ annealing, significant diffusion of Ni into the Au and PtSe₂ regions is observed. This is consistent with the diffusion seen in the optical images of c-TLM structures (Figure 2).

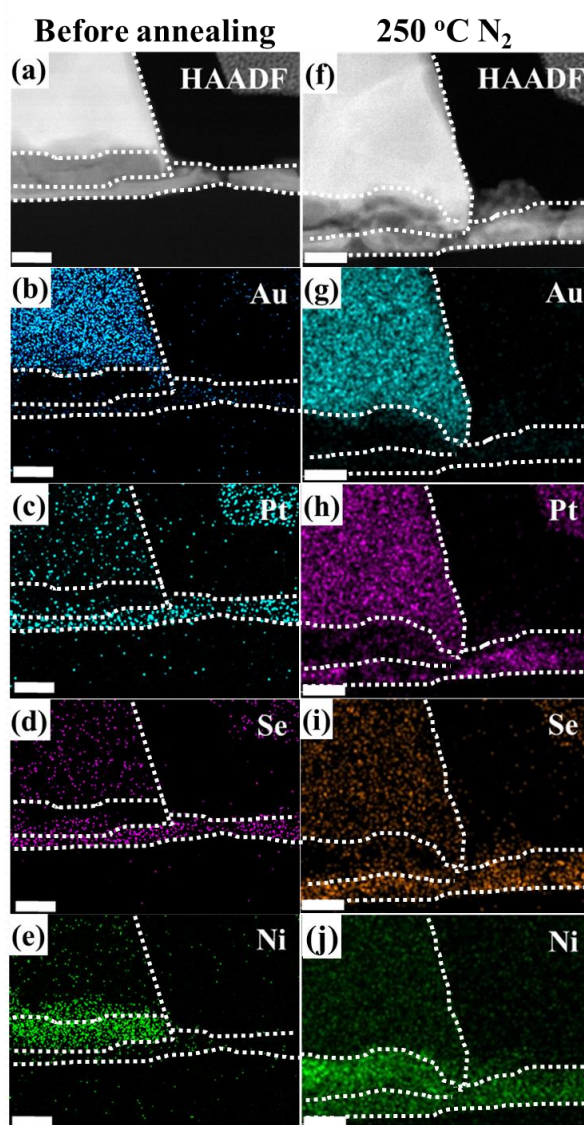


Figure 6: Compositional analysis performed via STEM based EDX on Ni-Au contacted PtSe₂ lamellas before and after annealing at 250 °C in N₂. (a) and (f) shows the HAADF image of the region under study before and after annealing respectively. b-e and g-l refer to the Au, Pt, Se and Ni signal, before and annealing respectively. Scale bar is 25 nm. The dotted lines are added around the Au, Ni and PtSe₂ regions to guide the eye.

5.4 DISCUSSION

The interaction between top contacts and TMDs is significantly different to contacts on conventional semiconductors due to the Van der Waals nature of the TMD surface. DFT simulations predict that due to the lack of surface covalent bonds for most deposited metals a van der Waals gap exists between the TMD surface and the metal contact.²⁴⁸ This van der Waals gap acts as a tunnel barrier for carrier injection into the TMD channel, in addition to the Schottky barrier between the metal and TMD,¹²⁶ increasing total contact resistance.⁵⁰

A study by Das et al.¹³⁵ showed that the Schottky barriers between metals and MoS₂ are not consistent with the energy difference between the metal work function and the TMD Fermi level. They showed that even metals which would be expected to act as *p*-type contacts (i.e. Ni and Pt) instead exhibited electron injection consistent with *n*-type contacts. This was ascribed to Fermi level pinning in the MoS₂ close to the conduction band minimum at the metal/MoS₂ interface.¹⁴²

Previous XPS studies on MoS₂ and WSe₂ considering a range of various metals²⁴⁹⁻²⁵² have shown that similar reactions between the as-deposited metal and a TMD are possible. Nonetheless, an interface reaction does not necessarily result in a lower contact resistance because of the defective nature of exfoliated TMD flakes. However, a complete transformation of the TMD below the contact might mitigate the effect of contact resistance. Kappera et al.²¹³ demonstrated low contact resistance in a MoS₂ FET varying the phase of MoS₂ below the contact from semiconductive (2H) to metallic (1T). Similarly, here we showed a Ni-PtSe₂ alloy at the contact and PtSe₂ in the channel region. However, in this work, a contact resistance analysis was not possible. The PtSe₂ under study had a thickness of ~6-10 nm, and in this thickness

range the PtSe₂ behaves as a semimetal, therefore it is not contact-resistance limited. Once the PtSe₂ growth processes are tuned further to achieve few-layer (<3L) films a more detailed contact resistance study could be performed. Also, the annealing temperature and ambient need to be optimised in order to control the diffusion/reaction of Ni.

A behaviour similar to Ni and PtSe₂ has also been observed for Ag/MoS₂.²²⁹ In that work, the samples were annealed between 250 °C and 350 °C in a rapid thermal annealing furnace for 300 s and the contact resistances values decreased after the thermal treatment, due to Ag diffusion and doping below the contact regions. Although Ag does not react with MoS₂ at room temperature,²⁵³ Souder and Brodie^{230, 231} showed that Ag diffused in bulk MoS₂ after annealing at 400-600 °C for 5 min, estimating a concentration of approximately 10¹⁹ cm⁻³.

It is unclear if the Ni is acting as a dopant for PtSe₂, however, the metal-TMD reaction could be of great interest to improve the contact resistance of TMD-based devices.

5.5 CONCLUSIONS

In this study, the Ti-PtSe₂ and Ni-PtSe₂ interfaces were explored, along with the impact of post-metallisation anneals in forming gas and inert ambient. Electrical and chemical characterization show that Ti is unreactive after annealing, even at relatively high temperature, while Ni readily reacts with PtSe₂ to form NiSe_x and reduced PtSe_x-Pt-metal. The reaction is enhanced with high temperatures or a hydrogen rich environment, which can cause the Ni to diffuse laterally into the PtSe₂.

The metal/PtSe₂ alloying is a possible solution for reducing contact resistance in few-layer devices based on PtSe₂ and other TMD materials.

Chapter 6: TCAD MODELLING AND ANALYSIS OF MoS₂

This chapter is adapted from the following publications and conferences:

Mirabelli, G.; Gity, F.; Monaghan, S.; Hurley, P. K.; Duffy, R. In Impact of impurities, interface traps and contacts on MoS₂ MOSFETs: Modelling and experiments, 2017 47th European Solid-State Device Research Conference (ESSDERC), 11-14 Sept. 2017; 2017; pp 288-291.

Mirabelli, G.; Zhao, P.; Bolshakov, P.; McGeough, C.; Gity, F.; Monaghan, S.; Hughes, G.; Hinkle, C. L.; Wallace, R. M.; Young, C.; Hurley, P. K.; Duffy, R., Study of interface defects in top-gated MoS₂ FETs: experiments and physics based simulations, IEEE Semiconductor Interface Specialist Conference (SISC), San Diego (CA), 2017.

6.1 INTRODUCTION

Device modelling is a key capability for the semiconductor industry, allowing process optimization and insight into the physics of novel architectures and materials difficult to access experimentally. Despite much innovative experimental work, device modelling capabilities for field effect devices based on Transition Metal Dichalcogenide channel materials are at an early stage of development. Properly formulated physics-based models would give a substantial improvement for time- and cost-effective development of TMD devices. Nevertheless, a TCAD model for Transition-Metal-Dichalcogenides, or for 2D-materials in general, is still missing. To date few publications showed the effective use of TCAD modelling for the understanding of 2D-semiconductors.^{167, 168, 254, 255} The immaturity of the material system itself causes a certain device-to-device variation, which makes even more difficult the development of a solid TCAD model. Even if the TCAD models on which these studies are based on might not be definitive, the simulations allowed a clear interpretation of the device physics, which would not be otherwise possible.

6.2 TCAD MODELLING FOR NEW MATERIAL SYSTEMS

The first step to start a TCAD analysis of any material is to load its “parameter file”. This file contains all the necessary basic properties, such as: as bandgap, dielectric constant, band structure, mobility of electrons and holes, electron affinity, which are necessary to opportunely solve the drift-diffusion equations in the device. These parameters are widely known for Silicon, for example, since it is a well mature material system. On the contrary, new material systems as TMDs, graphene or GeSn

are not yet defined. For new material systems a deep literature search is needed to have a complete and accurate parameter set.

The second part is the study of the electrical behaviour of the device. In this case, physical models need to be defined in order to match the physics of the device under test with the experimental data. Considering Silicon as example again, there are several models in order to consider the temperature dependence of its bandgap. Or the Shockley-Read-Hall generation/recombination parameters can be made dependent on the doping concentration. All these physical effects and models are not present for 2D-materials and due to the immaturity of the material system these effects are still unknown. In the case of the above-mentioned examples of bandgap and Shockley-Read-Hall generation/recombination parameters, they will be considered constant. Nonetheless, particular attention was paid to the mobility of MoS₂. This parameter is often extracted and characterised in literature, so the TCAD software was used in order to implement these effects in the software and study the impact on the electrical performance. An important question to consider is if models defined previously for 3D-semiconductors work as well for 2D-semiconductors. A simple tuning of the fitting parameters of a mobility model might not be enough, but this will be seen in the later paragraphs.

When both the material, physical and electrical models are defined, the material needs to be connected with other semiconductors (e.g.: pn junctions), oxides (e.g.: FET), or metals (e.g.: metal contacts). These interfaces are mostly defective and characterised by interface traps or Schottky barriers, which needs to be tuned in order to finally match the device behaviour. The structure of this chapter follows this trend, as schematically depicted in Figure 1. First the material properties of MoS₂ will be

defined considering both theoretical and experimental studies. Then, a mobility model dependent on unintentional impurities and electric field will be studied. Finally, the developed model will be used to study the defects introduced by the oxide-semiconductor and metal-semiconductor interfaces to improve the modelling capabilities for MoS₂ field-effect devices.

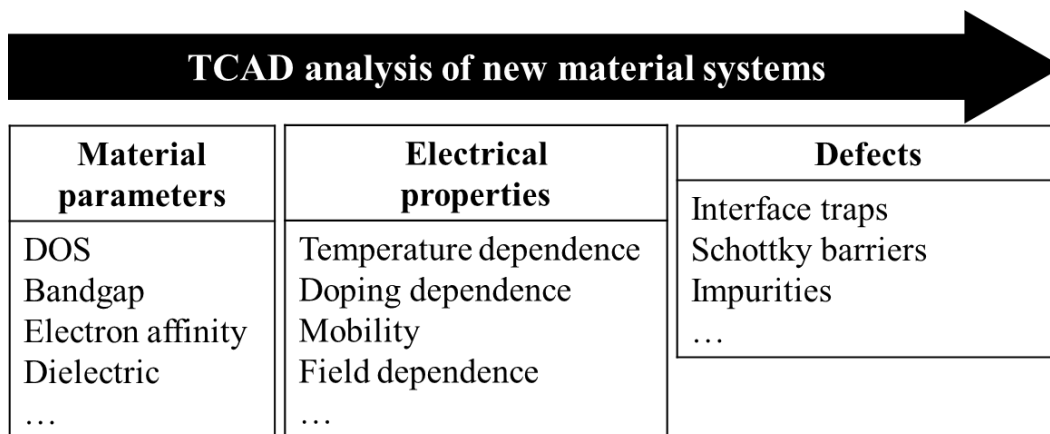


Figure 1: General schematic showing the steps to undertake in order to develop an accurate TCAD model and analysis for new material systems: define the material parameters, the electrical properties, and finally introduce defects/imperfections.

6.3 BASIC MATERIAL PARAMETERS

Figure 2a shows the variation of the carrier density versus Fermi energy for a single layer of MoS₂ and a good agreement is achieved with other studies.^{256, 257} Figure 2b, 2c and 2d shows the bandgap¹³, electron affinity²⁵⁸⁻²⁶¹, and effective mass variation²⁶²⁻²⁶⁵ of MoS₂, respectively. In these three plots the solid lines show the values that were used in the model. Other parameters are the in-plane dielectric constant²⁶⁶ and the carrier lifetime.²⁶⁷ In addition, to model the transport the drift-diffusion equations including Fermi distributions are solved, as discussed in chapter 1.^{200, 268} With the exception of the carrier density-Fermi Energy relationships

that is calculated by the TCAD software, the remaining parameters are input of the model and depend on previous theoretical studies or experimental findings.

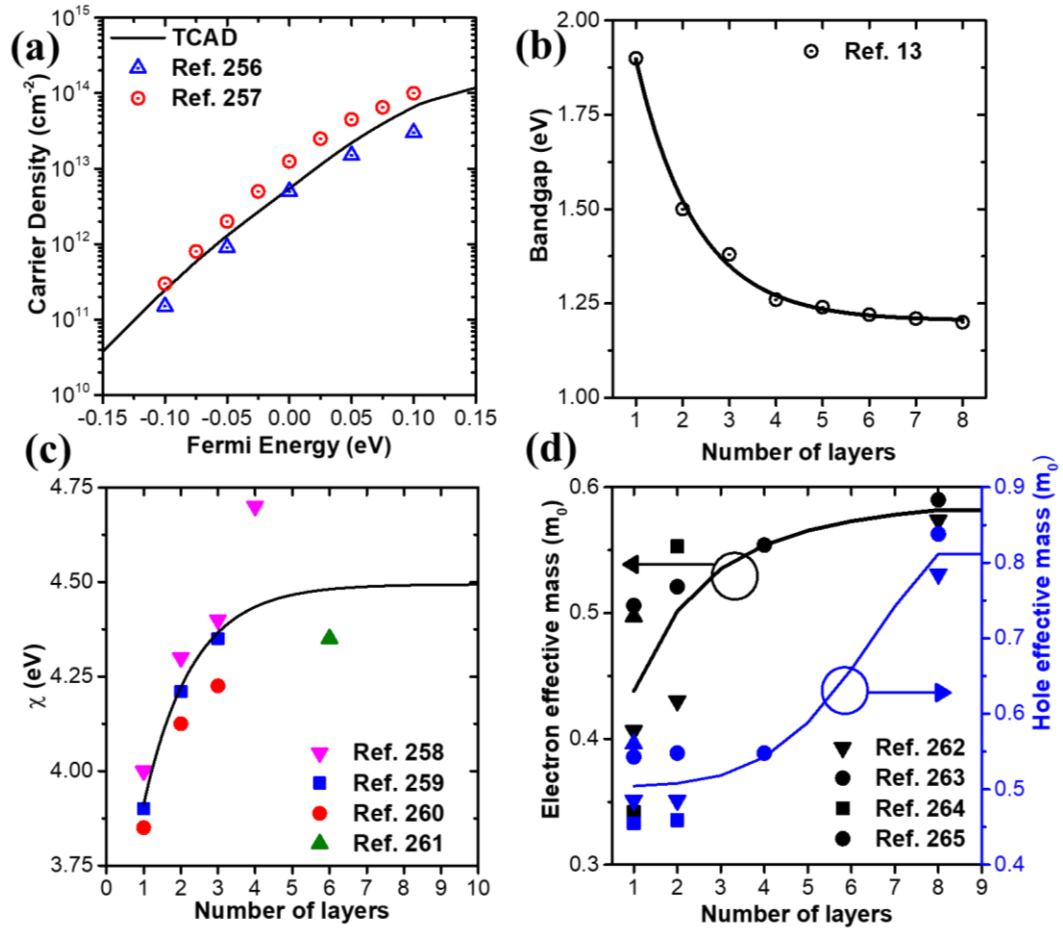


Figure 2: (a) Carrier concentration variation with respect of Fermi energy of monolayer MoS₂ introduced in Sentaurus compared with literature. (b) bandgap, (c) electron affinity and (d) electron/hole effective masses introduced in Sentaurus. Every parameter is thickness dependent, considering either theoretical calculations or experimental results.

Figure 3 shows a typical device structure implemented in Sentaurus device. The structure is generally set considering the experimental device under consideration.

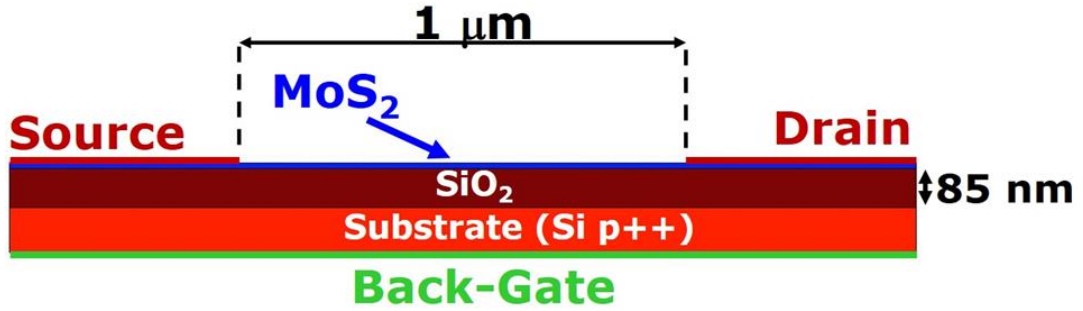


Figure 3: Schematic of a typical back-gated device structure implemented in Sentaurus device

6.4 MOBILITY MODEL

6.4.1 Low carrier density

The electron mobility in the low carrier concentration regime is highly dependent on the impurity concentration present in the material. This was reported to be one of the major scattering mechanisms in single layer MoS₂.²⁶⁹ On this regard, Ma and Jena⁹² calculated the mobility of single-layer MoS₂ in the relaxation-time approximation of the Boltzmann transport equation, considering the dependency of the dielectric environment and impurity density. This kind of scattering is similar to the one caused by a high doping concentration, since active dopants are charged scattering centres. The only difference is that doping will change the carrier concentration as well. The Arora model was used to take into account this dependency:²⁷⁰

$$\mu_{\text{dop}} = \mu_{\text{min}} + \frac{\mu_{\text{d}}}{1 + ((N_{\text{A},0} + N_{\text{D},0})/N_0)^{A^*}} \quad (1)$$

where μ_{dop} is the mobility dependent on Coulomb impurities, $N_{\text{A},0}$ is the acceptor concentration, $N_{\text{D},0}$ is the donor concentration and A^* , μ_{min} and μ_{d} are fitting

parameters. Figure 4 shows the theoretical model and the TCAD model implemented in Sentaurus. Even if this model was developed for silicon, varying the fitting parameters it is possible to obtain the same behaviour for monolayer MoS₂. Clearly mobility is highly limited by the impurity density in the material, as said before. It is also important to notice the mobility dependency on the dielectric environment, since a high-k environment will heavily affect it. This is important especially for FET applications. If one chooses a high-k dielectric to boost gate control, there is a clear drawback in terms of mobility.

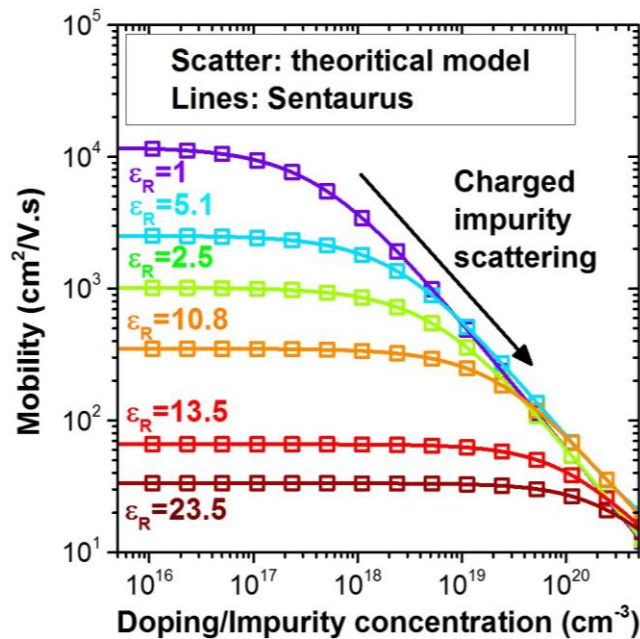


Figure 4: (a) Mobility versus impurity concentration considering different parameters implemented using the Arora mobility model. The theoretical model is based on DFT calculations for MoS₂,⁹² while the lines are the results obtained with the TCAD model.

Table 1 reports the value of each fitting parameter considering each curve in Figure 3. The maximum mobility is obtained for a dielectric environment of 1 (suspended MoS₂), around 10⁴ cm²/V.s. This value is rather higher than the

experimental values usually reported. Nonetheless, it can be related to both an immaturity of the material system and a possible overestimation of the theoretical mobility.

Table 1: Fitting parameters for the Arora model to match the theoretical model of MoS₂.

ϵ_R	N_0 [cm ⁻³]	A	μ_d [cm ² /V.s]	μ_{min} [cm ² /V.s]
1	4.39×10^{17}	0.97	11803.22	0
2.5	6.03×10^{18}	0.98	1015.07	0.27
5.1	2.78×10^{18}	0.99	2518.34	5.84
10.8	2.67×10^{19}	1.01	347.74	2.43
13.5	1.38×10^{20}	1.10	62.00	4.05
23.5	3.36×10^{20}	1.14	30.30	3.09

6.4.2 High vertical electric field

Another cause of mobility degradation is related to high vertical field. MoS₂ has shown a high critical electric field of 1.15×10^5 V.cm⁻¹.²⁷¹ However, a strong vertical electric field will shift the charges close to the charged defects associated with the gate dielectric, increasing the scattering rate for carriers degrading the mobility. The data reported in the previous chapter are not useful to evaluate this contribution because of the low electric field applied on the back gate. Nevertheless, a model that takes into account the mobility degradation due to high vertical electric field was reported in literature.²⁰⁰ Therefore, the results from this report will be used as benchmark to tune the TCAD model. The vertical electrical field degradation model depends on an empirical mobility model developed for Si MOSFETs,²⁰¹ similarly to

the model introduced with Sentaurus Device. It considers the mobility degradation observed at the HfO₂-semiconductor interface,²⁰² which was attributed to remote phonon scattering:

$$\mu_{rps} = \frac{\mu_{rps0}}{\left(\frac{F_{\perp}}{10^6 V/cm}\right)^{\gamma_1} \left(\frac{T}{300K}\right)^{\gamma_2}} \quad (9)$$

where μ_{rps0} , γ_1 and γ_2 are fitting parameters and F_{\perp} is the actual vertical field. T is the temperature. This model was validated against experimental results (with T= 300 K), as shown in chapter 3.3.2. Figure 5a shows the extraction of γ_1 from experimental data and the relationship with the dielectric constant. Figure 5b show the numerical calculation of Equation 9 and the impact of γ_1 on the mobility degradation. The mobility degradation rate increases for increasing values of γ_1 , therefore low values can be beneficial to avoid low mobility values at high vertical field.

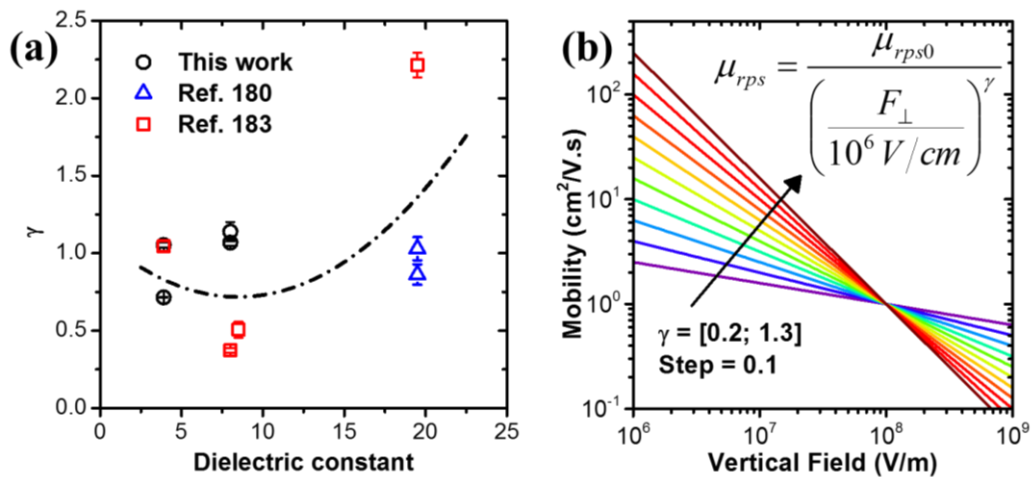


Figure 5: Model for high vertical electric field proposed in literature²⁰⁰ and Sentaurus results using the remote phonon scattering model.

6.5 APPLICATION OF THE DEVELOPED MODEL

In the next sections the developed model will be used to understand and quantify the two typical limitations of FET based MoS₂ devices: the MoS₂-metal interface and the MoS₂-oxide interface. Although a fairly good agreement between simulations and experiments is obtained it is important to remember that both the developed model and the material itself are immature. More work from both the theoretical and experimental side will be needed in order to develop a complete TCAD model and extract precise material parameters. Nonetheless, the following analyses give a fair understanding of the main mechanisms limiting the experimental devices, which can be used not only to understand the physics behind a certain behaviour, but are also useful to steer possible experimental plans.

6.5.1 MoS₂-metal: contact barriers

As shown in chapter 1, the metal-TMD interface often results in high Schottky barriers. Figure 6a shows high energy XPS measurements conducted on MoS₂ crystals considering different metals. Even if the workfunction of the metals ranges considerably, the Fermi level at the metal-MoS₂ interface pin at approximately the same energy, $\cong 0.2$ eV below the conduction band. The value that will be later used to match the experimental results of the device “Trapezium” (Chapter 3) is 0.17 eV, which is close to experimental values.¹⁴²

Figure 6b shows the effect of the barrier on the simulated transfer characteristic of a typical back-gated single layer MoS₂, with doping concentration of 10^{17} cm⁻³. It is easy to notice that a decrease in the Schottky barrier would result in a great improvement of the overall behaviour of the device. Also shown is the case of using the Fermi-level pinning model. Considering a value of pinning of 0.2 and a work

function of 4.33 eV (Titanium), the result is similar to using a Schottky barrier of 0.6 eV (from Equations 5 and 6 of Chapter 1). That is because considering the said parameters, the equivalent barrier at the contact using the Fermi-level pinning model is ~ 0.6 .

Therefore, for the sake of modelling the contacts, Schottky barriers will be considered as a variable for each device under consideration. The Fermi-level pinning model sets a fixed barrier height considering the pinning level, work function of the metal, electron affinity of the semiconductor and charge neutral energy level. Nonetheless, due to the variability of 2D-semiconductors, the actual barrier could differ from this value.

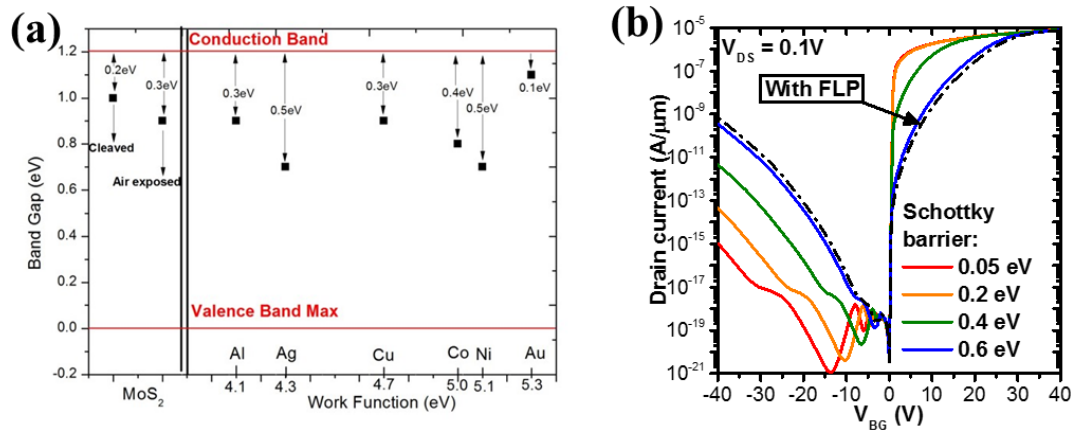


Figure 6: (a) High energy XPS measurements conducted on MoS₂ crystals with different metals. (b) Simulated transfer characteristics varying the Schottky barrier at the source and drain contacts. The structure of the simulated device is as reported in Figure 2: 1L of MoS₂ with 1 μm of channel length.

6.5.2 MoS₂-oxide: interface traps

6.5.2.1 Back-gated MoS₂

The subthreshold behaviour of the device is dependent on interface traps located at the oxide/MoS₂ interface. To model the subthreshold slope of the experimental transfer characteristic, acceptor like interface states are introduced close

to the MoS₂ conduction band edge. In particular, the device under consideration is the device “Trapezium”. The electrical characteristics of this device were reported in Chapter 3. In order to match the subthreshold behaviour of the Trapezium, four trap energies are introduced, with energy levels at $E_{t1}=1.25kT$, $E_{t2}=2.5kT$, $E_{t3}=5kT$ and $E_{t4}=10kT$ from the conduction band and with concentration of 8×10^{11} , 3×10^{11} , 2.5×10^{11} and 1×10^{11} cm⁻², respectively (Figure 7a). Thanks to the software it is possible to selectively choose which interface traps are active. Figure 7b shows how the transfer characteristic of the device would look like if there were no interface traps, if only the traps close to the conduction band were active (E_{t1} and E_{t2}) and if only the traps close to the mid-gap were active (E_{t3} and E_{t4}).

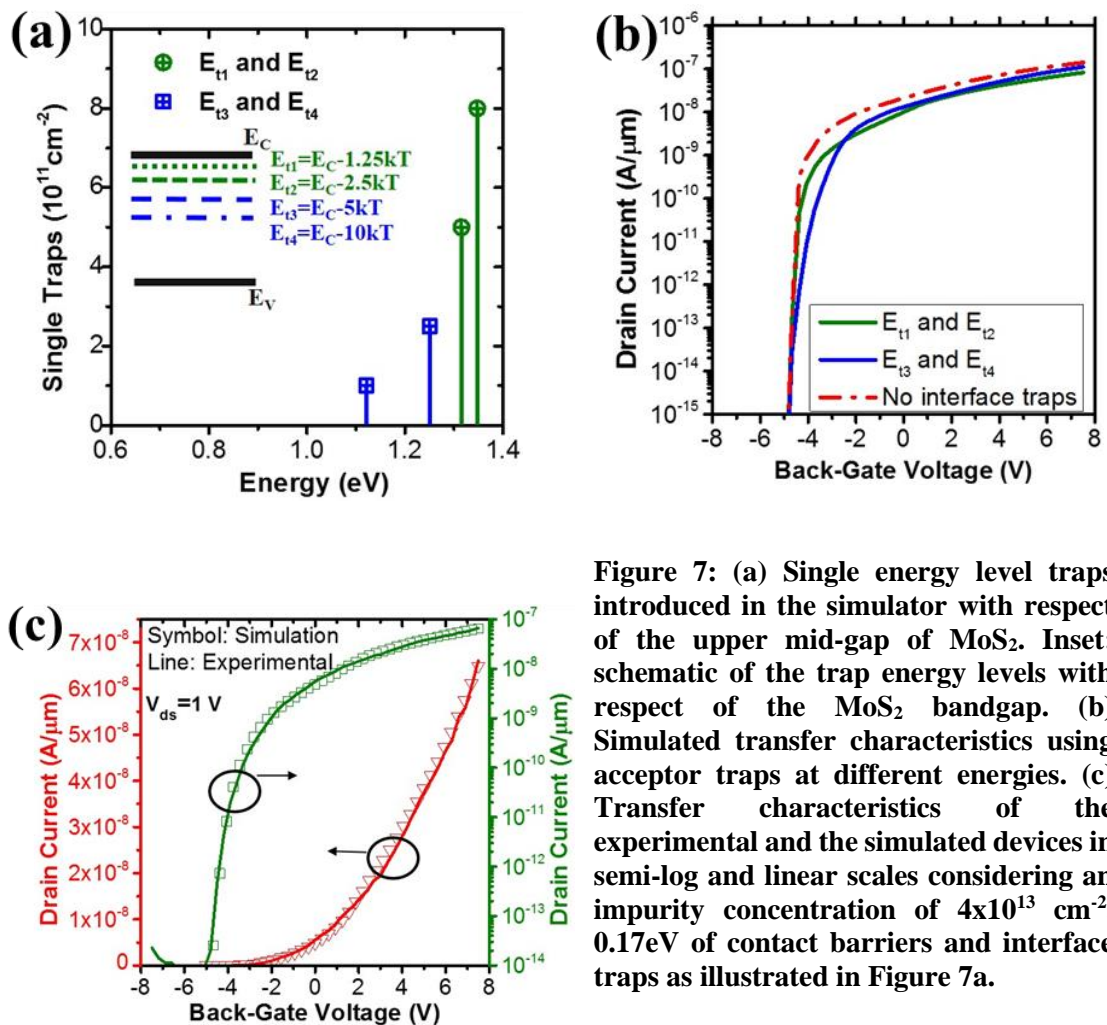


Figure 7: (a) Single energy level traps introduced in the simulator with respect of the upper mid-gap of MoS₂. Inset: schematic of the trap energy levels with respect of the MoS₂ bandgap. (b) Simulated transfer characteristics using acceptor traps at different energies. (c) Transfer characteristics of the experimental and the simulated devices in semi-log and linear scales considering an impurity concentration of 4×10^{13} cm⁻², 0.17eV of contact barriers and interface traps as illustrated in Figure 7a.

Figure 7c compares the experimental and the simulated data, with an impurity concentration of $4 \times 10^{13} \text{ cm}^{-2}$, contact barrier of 0.17 eV and the interface traps as shown in Figure 7a. It is important to consider that in this case the interface traps are varied after modelling the contact (Schottky barrier at the drain/source contact) and mobility (impurity concentration equal to the one extracted from the mobility, as shown in Chapter 3). Therefore, an error in the contact or mobility modelling will result in an added uncertainty to the extracted density of interface traps. However, these results are still relevant in order to approximately quantify the effect of each non-ideality. For a better understanding of each defect ad-hoc test-structures are needed, as TLMs for contact studies or MOSCAP for the study of the MoS₂/oxide interface.

6.5.2.2 Top-gated MoS₂

In relation to the interfacial properties, recent results based on impedance spectroscopy analysis of MOS²⁷² and MOSFET^{273, 274} structures indicate the presence of electrically active defects at the MoS₂/Al₂O₃ and MoS₂/HfO₂ interface. Considering previous reports,^{273, 274} ac physics based simulations were used, in conjunction with experimental MoS₂ MOSFETs characteristics, as a metrology approach to profile the density and energy of electrically active defects at the MoS₂/HfO₂ interface. The physics-based ac simulations, in conjunction with the experimental data, provides more insight into the density, energy level and carrier capture cross section values of electrically active defects at the MoS₂/oxide interface properties in thin channel MOS₂ MOSFETs.

Figure 8a shows the optical picture of the device under consideration. Ti/Au contacts are deposited under High Vacuum using photolithography and lift-off. HfO₂ was deposited by Atomic Layer deposition after an UV-O₃ treatment.²⁷⁵ Cr/Au was deposited as the metal gate.

Figure 8b shows the structure implemented in the Synopsys Sentaurus TCAD Device simulator. The dimensions are set to match the experimental device²⁷⁴ (Figure 8a). The dielectric constant and bandgap of MoS₂ are set as explained at the beginning of this chapter, while the charged impurity concentration, required for carrier mobility modelling, is taken from fitting of various back-gated MoS₂ MOSFETs as explained in the previous chapter. The n-type doping is determined as $1.25 \times 10^{19} \text{ cm}^{-3}$. The actual carrier concentration in the flake following exfoliation might be lower, but positive fixed charges in the HfO₂ can provide effective electrostatic doping to the thin MoS₂ channel. The dielectric constant (k) of the ALD HfO₂ is determined to be 13 based on the experimental C-V accumulation capacitance and a HfO₂ thickness of 13 nm derived from cross-sectional transmission electron microscopy measurements.^{273, 274} An alternative approach is to take HfO₂ with k=17 and consider a van der Waals gap of 0.3 nm (k=1) at the MoS₂/HfO₂ interface.²⁷⁶ The Ti/MoS₂ Schottky barrier height set as 0.12 eV considering previous studies¹⁴² and high energy XPS measurements.

Figure 9b shows the experimental and simulated transfer characteristics. The curves are in excellent agreement, except for gate voltages higher than -1V, likely related to the modelling of the contacts, which is not the primary aim of this work. In order to match the simulated and experimental behaviour, acceptor traps were added at the MoS₂/HfO₂ interface (Fig. 9a). A constant trap energy in the upper mid-gap of MoS₂ was introduced, with concentration of $3.5 \times 10^{12} \text{ cm}^{-2} \text{ eV}^{-1}$. In addition, three

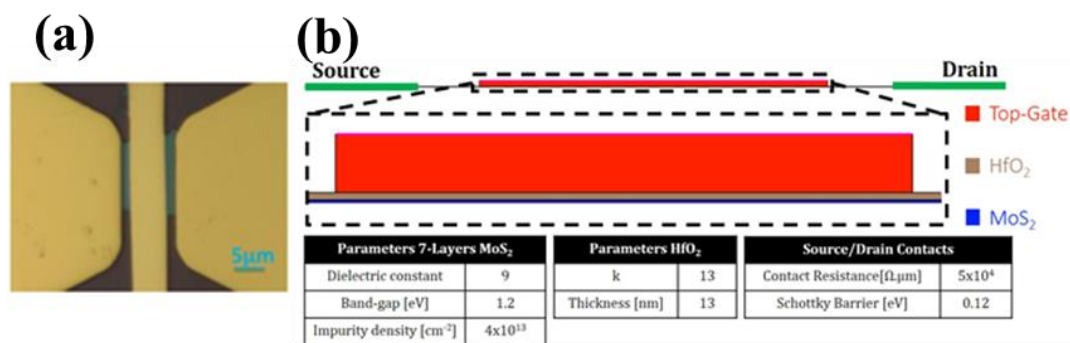


Figure 8: (a) Optical view of the top-gated MoS₂ flake.^{273, 274} Ti/Au contacts are deposited under High Vacuum using photolithography and lift-off. HfO₂ was deposited by Atomic Layer deposition. Cr/Au was deposited as the metal gate. (b) Schematic of the structure implemented in the Sentaurus physics-based device simulator. The tables show the parameters selected for MoS₂, HfO₂ and the Ti/MoS₂ contacts.

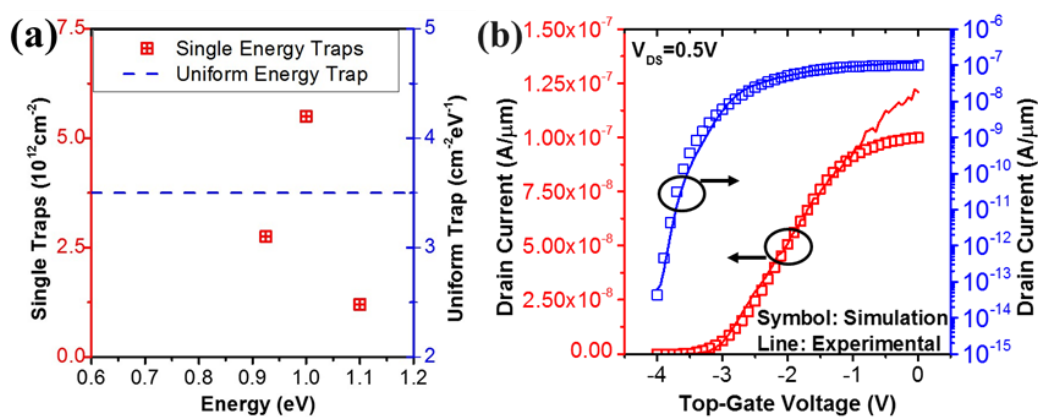


Figure 9: (a) Trap distribution with respect to the valence band edge of MoS₂. The traps span from the mid-gap (0.6 eV) to the lowest energy in the MoS₂ conduction band. (b) Transfer characteristics of the experimental and the simulated devices in log (blue) and linear (red) scales. The fit of the simulated response to the experimental transfer characteristic is obtained using the interface trap distribution shown in Figure 6a.

single energy level traps are added, at energies 0.925, 1.0 and 1.1 eV, with concentrations of 2.75×10^{12} , 5.5×10^{12} and $1.2 \times 10^{12} \text{cm}^{-2}$ respectively. The corresponding fitting is close to the experimental density of interface traps (D_{it}).^{273, 274} With the D_{it} energy and density obtained from the DC device characteristics, these

same parameters were employed to determine if they can reproduce the observed experimental multi-frequency gate-to-channel C-V response. One of the advantages of the physics-based ac simulations model is the ability to selectively turn “on and off” the frequency dispersion of each trap, by selecting low ($<10^{-24}$ cm²) trap cross-sections. Unfortunately, 2D-materials in general were not deeply studied through CV analysis, therefore a value for trap cross-section is not present yet. Therefore, the cross-section will be used as a variable.

Figures 10a and 10b shows the effect of the single energy traps located at 0.925 and 1.0 eV respectively at different cross-sections at a frequency of 1 kHz. The cross-section range were set in order to see the most variation of the CV curve related to the particular trap. Both shows a similar signature because of the single energy level. The main difference between the two is the position of the peak with respect of the gate voltage.

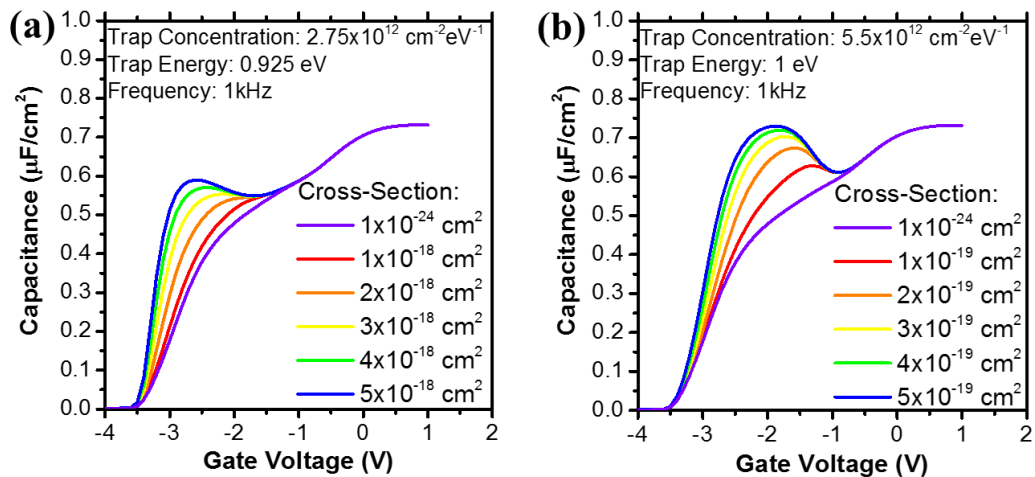


Figure 10: CV simulations of the single energy level trap located at (a) 0.925 eV and (b) 1 eV. Cross-section is used as a variable in a range when the effect of the trap is clear.

Figure 11a shows the experimental CV result. By comparison, it is possible to understand which of the trap levels introduced before (Figure 8a) is the responsible of the experimental CV response. As is clear from comparing Figure 10a and 10b with the experimental response in Figure 11a, the trap located at 1 eV is too close to the conduction band to give a CV response similar to the experimental one. Similarly, the trap located at 1.1 eV can be ruled out.

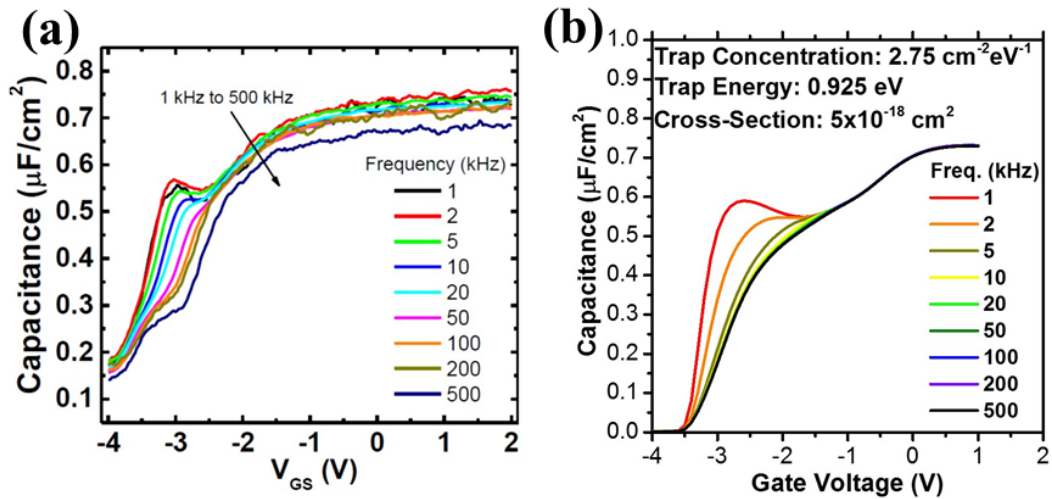


Figure 11: (a) Experimental²⁷⁴ and (b) simulated CV response. The simulated CV response consider the trap at energy 0.925 eV, with concentration $2.75 \times 10^{12} \text{ cm}^{-2}$ and a cross-section value of $5 \times 10^{-18} \text{ cm}^2$.

Therefore, the simulations indicate that the single energy trap located at 0.925 eV is the responsible of the experimental CV behavior. This energy level is consistent with previous reports, in which CV analysis of thick MoS₂ was conducted by Therman method.²⁷² In particular, the energy range of Sulphur vacancies, the most common defect in exfoliated MoS₂, is usually 0.9-1 eV. Of course, it is possible to notice that there is still a certain difference between the experimental and the simulated CV, as the experimental behavior is most certainly due to a combination of several traps.

Nevertheless, considering more traps can be difficult, because of the higher number of variables and the sensitivity of the CV response on the trap cross-section.

Lastly, it is possible to evaluate the effect of the uniform trap, which was not evaluated so far. Figure 12 shows the CV responses varying the cross-section of the uniform trap, considering also the single energy level traps at 0.925 eV. From Figure 12a to 12c the cross-section of the uniform trap increases from $5 \times 10^{-18} \text{ cm}^2$, to $5 \times 10^{-17} \text{ cm}^2$ and to 10^{-15} cm^2 . An increase in the trap section results in a major dispersion towards more negative gate voltages. This results in an even similar response with respect of the experimental results. Nevertheless, as said before, experimental values of trap sections are not yet present in literature. Even if the software is useful to understand which is the approximate energy related to the trap responsible of the CV response, considering more than one trap might lead to wrong conclusions as there might be too many variables to take into account. On top of that, CV responses are highly sensitive to trap cross-sections.

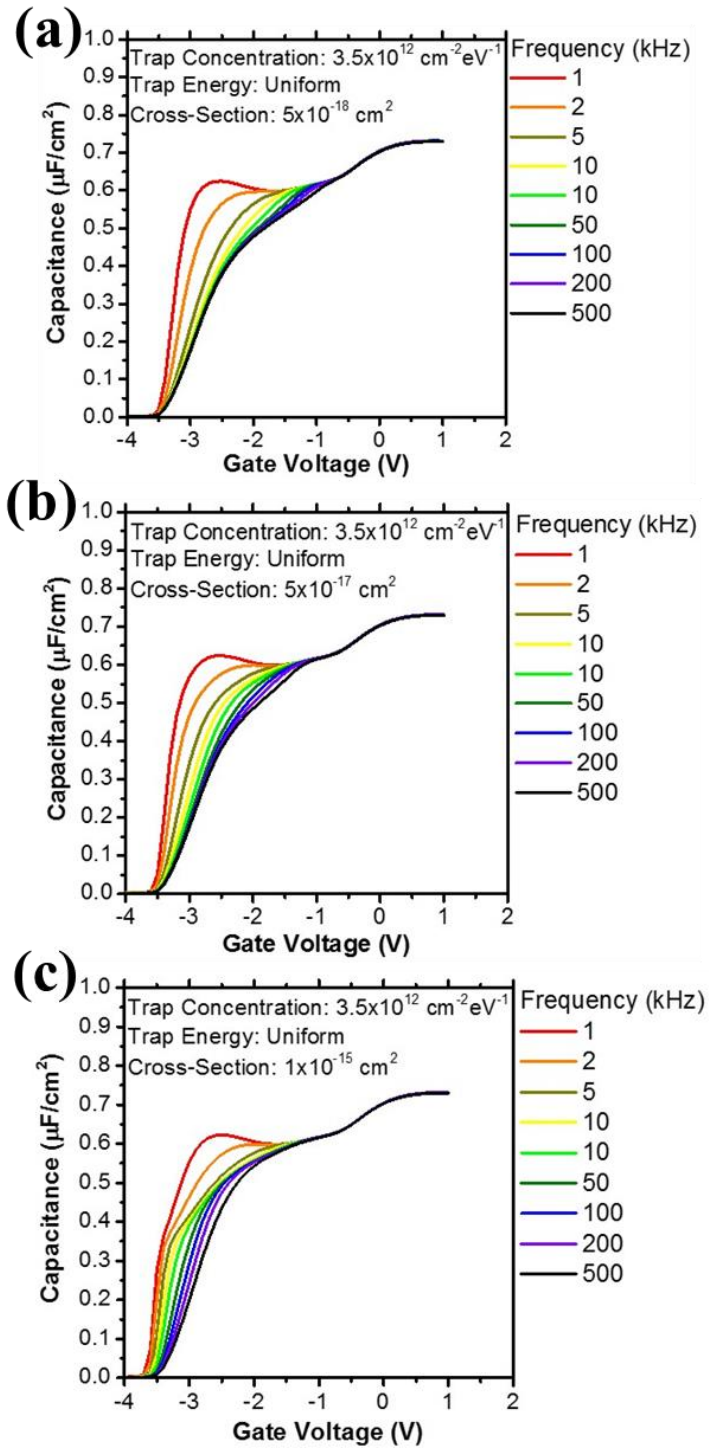


Figure 12: Simulated CV response of the single energy level traps at 0.925 eV in addition to the uniform trap, which cross-section: (a) $5 \times 10^{-18} \text{ cm}^2$, (b) $5 \times 10^{-17} \text{ cm}^2$ and (c) 10^{-15} cm^2 .

6.6 CONCLUSIONS

In conclusion MoS₂ FETs were electrically characterized from which continuum-based models and parameter sets were developed. It has been shown that the experimentally extracted field-effect mobility values are strongly dependent on the high impurity concentration present in the material, which limit its true potential. Furthermore, with the combination of CV analysis and TCAD simulations the CV response of a top-gate MoS₂ FET was explained considering a single energy level trap, related to sulphur vacancies. Very good agreement between the model and the experimental results has been achieved. Even if promising results are shown to date, the true TMD device performance is still masked by imperfections, which can be tackled by purifying and optimizing the growth and device processing conditions to reduce impurities and improve TMD stoichiometry.

Chapter 7: THE LAYERED STRUCTURE CONCEPT

This chapter is adapted from the following publications and conferences:

Mirabelli, G.; Hurley, P. K.; Duffy, R., Physics-based modelling of MoS₂: the layered structure concept, SISPAD, Austin (TX), 2018.

Mirabelli, G.; Hurley, P. K.; Duffy, R., Physics-based modelling of MoS₂: the layered structure concept. Semiconductor Science and Technology 2019, 34 (5), 055015.

7.1 INTRODUCTION

Previous publications investigating continuum-based modelling in MoS₂ have accounted for the 2-Dimensional structure based on highly asymmetric mobility in-plane and out-of-plane, while maintaining a homogenous structure. In this work, instead of using a continuous slab of semiconductor, as previously reported, we introduce in a TCAD tool the “layered structure”, which takes into account both in-plane drift and diffusion currents and a tunneling process through the Van-der-Waals gap (VdW-gap) between the layers of the 2D-semiconductor. This type of layered-modelling with a TCAD tool is still missing in the state of the art, even if the layered structure is a fundamental feature of TMDs or any other 2D-material and modelling might benefit from its introduction. For this study of transport in 2D-semiconductors the continuum-based Synopsys Sentaurus Device software was used.¹⁴⁶

The analysis is calibrated using previous experimental findings based on vertical transport through MoS₂. The results show that 2D-semiconductors can be modelled by a TCAD tool and the layered structure can be particularly important when a few layers of material are considered, as the layered characteristics of the material have a greater impact with reducing 2D film thickness.

Figure 1a shows a representative TEM image of 3-layers of MoS₂ taken in the channel region of a back-gated MoS₂ MOSFET, where it is possible to notice the characteristic layered structure of the semiconductor. The structure is represented schematically in Figure 1b in order to emphasize the division between each MoS₂ layer. This same layered representation is used in the TCAD (Figure 1c) where the layers of semiconductors are alternated by VdW-gaps. The green stripes are the MoS₂ layers, while the light-blue layers are the VdW-gaps. The Van-der-Waals gaps are set

between the layers of the MoS₂ only, and not between the MoS₂ and the oxide or the MoS₂ and the contact. These effects are outside the scope of this work which is the carrier transport in the MoS₂ layers.

The thickness of the MoS₂ and the gap layers in Figure 1c is set initially to 0.32 nm and 0.29 nm respectively, close to the values that are usually visible by TEM analysis or calculated by X-ray diffraction.²⁷⁸ However, the effective electrical thicknesses might be different. Previous studies have shown that there exists an overlap of the wave functions and an exchange interaction between nearby MoS₂.²⁷⁹ During the analysis the thickness of one layer of MoS₂ and one VdW-gap will be constant and equal to 0.61 nm, which is the known thickness of monolayer MoS₂. Nevertheless, the effective electrical thickness of the two sub-components will change as it is a variable that needs to be benchmarked against experimental data.

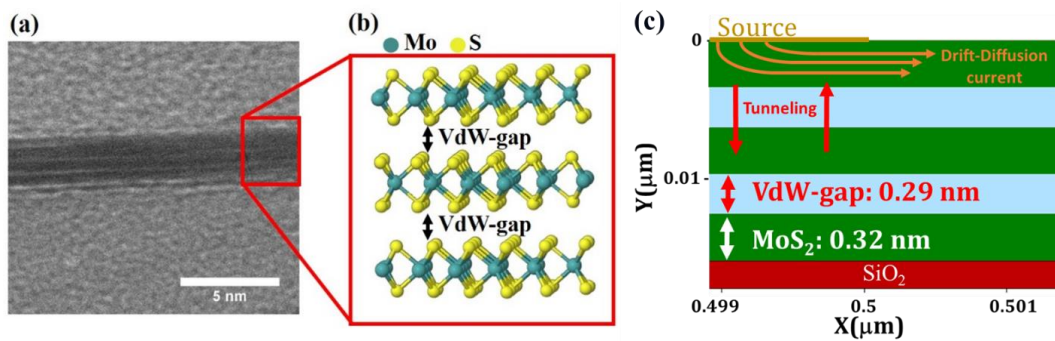


Figure 1: (a) Representative TEM image showing the layered structure of MoS₂. (b) Representation of the structure of MoS₂ showing the Van-der Waals gaps between the layers.²⁷⁷ (c) Schematic of the layered structure implemented in the Sentaurus physics based device simulator.

In general there will be two kind of currents: (1) parallel current in the MoS₂ layers, which is modelled by the drift-diffusion equations, and (2) perpendicular

transport in between layers due to direct tunneling through the gaps, which act as tunneling barriers.

Figure 2b shows the conduction band energy of 5 layers of MoS₂ considering a uniform (red) and a layered structure (black). For the layered structure, it is clear that, to have conduction from the top to the bottom of the device, tunneling through the VdW gaps is necessary. Note that the VdW-gaps are aligned with the vacuum level, while the workfunction of the MoS₂ layers are equal to 4eV at this thickness, as evaluated experimentally. Similarly, Figure 2c shows the electrostatic potential variation in 5 layers of MoS₂. Due to the presence of the VdW gaps, the variation for the layered structure is not linear with distance, as in the uniform structure, but exhibits two distinct gradients of potential for the MoS₂ region and the VdW region, based on their respective dielectric constant.

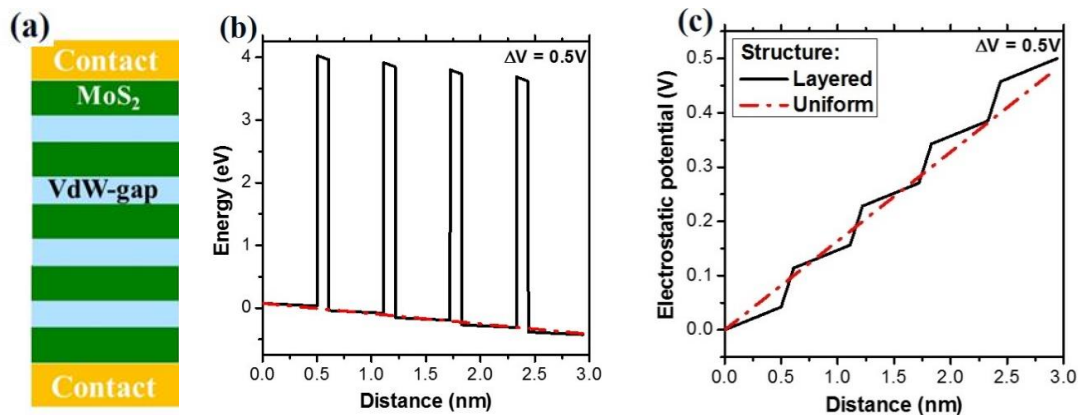


Figure 2: (a) Device structure considered. (b) Conduction band energy and (c) electrostatic potential variation in the layered and uniform structure, with a voltage of 0.5V applied across the device. For these simulations the VdW-gap is 0.11 nm and the MoS₂ thickness is 0.5 nm. The dielectric constant of MoS₂ is equal to 3.

The dielectric constant of each VdW gap was set to 1. The dielectric constant of MoS₂ was experimentally measured and the values for different thicknesses are

known.²⁶⁶ For samples thicker than 10 nm, which is the case of the experiments that will be considered in this work, the value is initially 10.5. Nevertheless, as will be later explained, it will be considered as a variable since for previous calculations MoS₂ was considered as a uniform semiconductor. Other basic parameters are set considering reported theoretical and experimental results.

7.2 METHODOLOGY DEVELOPMENT

The methodology adopted in this work is to first model the vertical transport through the layered MoS₂, and to use this to subsequently model transport of a back gated MoS₂ MOSFET structure. In relation to the Figure 1b, the vertical transport will be determined by direct tunneling process through the VdW gaps. The model implemented for direct tunneling in Sentaurus is determined by: the barrier height to tunneling (see Figure 2b), the tunneling effective mass of the electron in the VdW gap, and the potential difference between the two MoS₂ layers.²⁸⁰ The potential difference between two consecutive layers will be determined by the vertical dielectric constant assumed for the single layer of MoS₂. As we assume the VdW gap is vacuum, the barrier to electron tunneling is set at 4eV. Consequently, the parameters to be determined are the dielectric constant of the MoS₂ and the effective electron mass during tunneling. To obtain these values we calibrate the model against published experimental data for vertical transport through MoS₂.^{281, 282}

In the experimental work which will be used to calibrate the tunneling model,²⁸² MoS₂ was exfoliated on a gold metal pad and SiO₂ or HSQ was patterned by lithography on top of the flake as an isolation layer. The top metal was Ni/Au. In this way it was possible to consider only the perpendicular conduction in MoS₂. Based on an analysis of the experimental data assuming the MoS₂ as a homogeneous

semiconductor a Schottky barrier of 0.3 eV at the contact was determined for the Au/MoS₂ contact, while the effective perpendicular mass was evaluated to be 0.18 m₀. Both these values will be considered in our simulations as well.

The TCAD software solves the drift-diffusion equations in both the parallel and perpendicular direction (along the x- and y-axis respectively of Figure 1c). The parallel mobility will be set according to experimental findings as we will explain in a later section. For the modelling of the perpendicular transport, the aim is that this conduction component is limited by tunneling through the VdW-gaps. To achieve this, the perpendicular electron mobility is increased to a point where it no longer affects the conduction.

Figure 3a reports the experimental and simulated perpendicular drain current at 3V as a function of the total thickness of the MoS₂. The figure shows 3 curves where the individual layer thickness of the MoS₂ is varied (and the VdW-gap thickness accordingly). The results at 3V, with a MoS₂ individual layer thickness between 0.5 and 0.55 nm are in reasonable agreement with experiments. The data from Zhu et al.²⁸¹ at 1V were also considered, which show less agreement with the simulations. One reason might be the different top contact used for the devices, Ti instead of Ni, which is known to form a layer of TiO₂ at the MoS₂ interface.

Figure 3b shows the current density considering a variation of the Schottky barrier at the contact from 0.15eV to 0.45eV. The value of 0.3eV is the barrier height used for Figure 2a. A variation in the barrier causes the current density to move almost rigidly along the y-axis. At a voltage of 3V the barrier has little effect on the simulations because the voltage is considerably higher than the Schottky barrier.

Figure 3c shows the variation in the current density when modifying the dielectric constant of MoS₂, from 3 to 20. The value of 10.5 is the one used initially. The variation in dielectric constant has a significant effect, and a reasonable fitting is obtained with a dielectric of 3, which is consistent with previous theoretical studies.²⁸³ A variation in the dielectric constant will change the partition of the electric field in the device. A lower dielectric in the MoS₂ will increase the potential drop between consecutive MoS₂ layers, which increases the direct tunneling current. Based on this analysis, while not fully optimized, the following section takes a perpendicular dielectric constant of the MoS₂ as 3, the thickness for the MoS₂ layer will be 0.5 nm, with a 0.11 nm VdW-gap.

Figure 3d shows the vertical current from two experimental devices with different layers of MoS₂, in comparison with the TCAD model. It is noted that while the parameter tuning process was performed at a fixed voltage (3V) there is a good agreement with the experimental data across the full voltage range and for the two value of MoS₂ thickness.

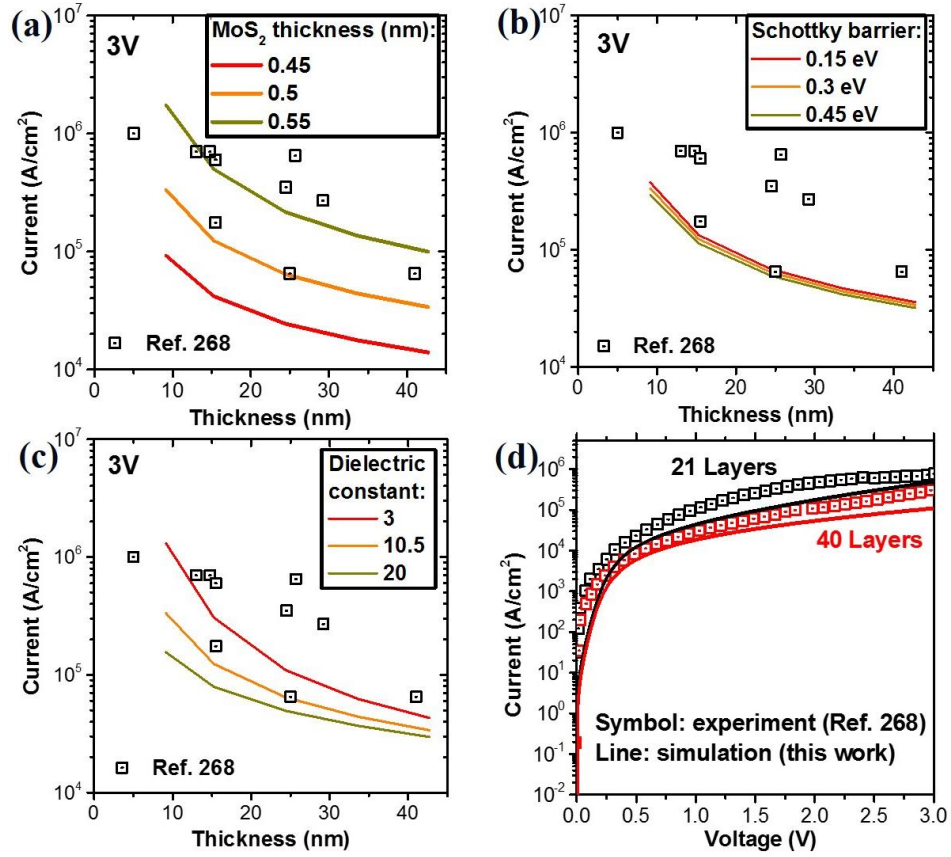


Figure 3: Current density at 3V for different thickness considering a variation of: (a) MoS₂ thickness, (b) Schottky barrier and (c) perpendicular dielectric constant of MoS₂. Unless specified, a dielectric constant of 10.5 and a thickness of 0.5 nm were used for the MoS₂, with a Schottky barrier of 0.3eV. (d) Comparison of the simulated and experimental vertical current for two different thicknesses reported by Zhang et al.²⁸².

Generally, the differences between simulations and experiments can be related to the immaturity of the material itself, which can cause experimental error in the extraction of the Schottky barrier or the dielectric of MoS₂. The Schottky barrier can differ from the value of 0.3eV for different samples due to different thickness,¹²⁶ impurities and defects, which are highly present in TMDs in general. As reported by McDonnell et al.¹⁴³, a defect density of 0.3%, common in TMDs, can be sufficient to dominate the contact resistance and it can also cause device-to-device variation. Furthermore, the dielectric constant of MoS₂ might differ from the experimental

extracted value as it is not only dependent on the number of layers, but first-principle calculations showed a certain dependency on the perpendicular electric field as well.

7.3 APPLICATION OF THE DEVELOPED MODEL: BACK-GATED MoS₂

Using the parameters for the vertical MoS₂ transport obtained in the previous paragraph, the implications of the layered MoS₂ structure to the characteristics of a back-gated MoS₂ MOSFET are considered in this section. For the purpose of this study, which is comparative study between the homogeneous and the layered MoS₂ structure, additional effects such as interface traps or Schottky contacts are not considered. The simulated device is discussed in Figure 4a, the channel length is equal to 0.5 μm , and the device is back-gated with 20 nm of SiO₂. The thickness of MoS₂ was chosen as 8 layers and a uniform *n*-type doping concentration of 10^{17} cm^{-3} was chosen.¹⁹⁷ A constant anisotropic mobility model is used (bias independent). The in-plane parallel mobility depends on previous experimental results (Figure 4b),²⁸⁴ while the out-of-plane conduction is as described in the previous section. This back-gated structure is typical of many MoS₂ FET devices reported in literature. The device characteristics are compared for the case of the layered structure, with the parameters derived from the previous sections, and for the case of a homogeneous MoS₂ film. While the parallel mobility will be the same between the two models, for the homogeneous MoS₂ case we take a perpendicular mobility of 0.5 $\text{cm}^2/\text{V}\cdot\text{s}$. This is increased from the value of 0.2 $\text{cm}^2/\text{V}\cdot\text{s}$ considered in a previous work.¹⁶⁸ The increase in the perpendicular mobility of 0.5 $\text{cm}^2/\text{V}\cdot\text{s}$ was implemented so that the current level of the two structure is similar to facilitate a qualitative comparison.

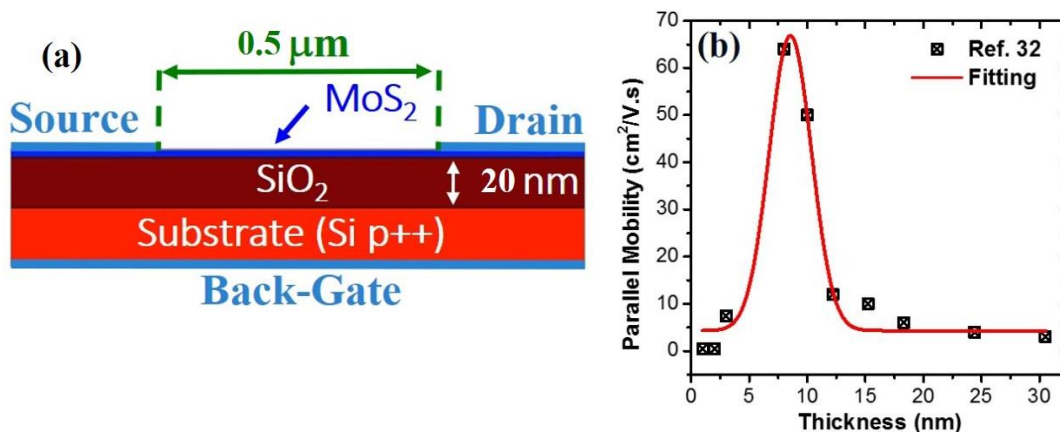


Figure 4: (a) Schematic of the device structure implemented in Sentaurus device. (b) Layer dependent parallel mobility used for both structures.²⁸⁴

Figure 5a and 5b show the transfer characteristic varying drain voltage for the uniform and the layered structure respectively. The first obvious difference is the current density considering the same applied voltages. The layered structure shows a current almost an order of magnitude higher. Nevertheless, the transition from off to on in the layered structure is much gradual around 0.5-1.0 V. In order to clarify both these points Figure 5 c-h show the current density in the whole device, increasing the drain voltage from 0.5 to 3V at a back-gate voltage of 5V.

Considering first the variation of the current density at any fixed drain voltage it is clear that the current density is mostly limited to the bottom layers. When a drain voltage is applied the current density will increase closer to the drain contact, passing through the whole structure. This is true for both structures, and the increase in drain voltage creates a “path” from the bottom of the semiconductor to the drain contact. From the contour plots at the highest drain voltage for both structures, Figure 5e and 5h, it is clear that below the tip of the drain contact the current density increases. As a result, the difference between the two transfer characteristics is related to how the current vertically passes through the structure. The uniform structure depends on the

perpendicular mobility, while for the layered one depends on direct tunneling through the VdW-gaps. Even if the first option might generate results that are in agreement with experimental data the transport process in a real MoS₂ is likely different. Due to a discrete structure formed by separate layers it is unlikely that the process can be simply described by a perpendicular mobility with a drift-diffusion transport model. Also, especially for thin devices the assumption of a perpendicular mobility does not have a physical meaning by definition, since the film thickness will be less than the mean free path between collisions. Therefore, the presence of the VdW-gaps provides a more accurate description of the transport in a real MoS₂ film, or 2D-semiconductor in general.

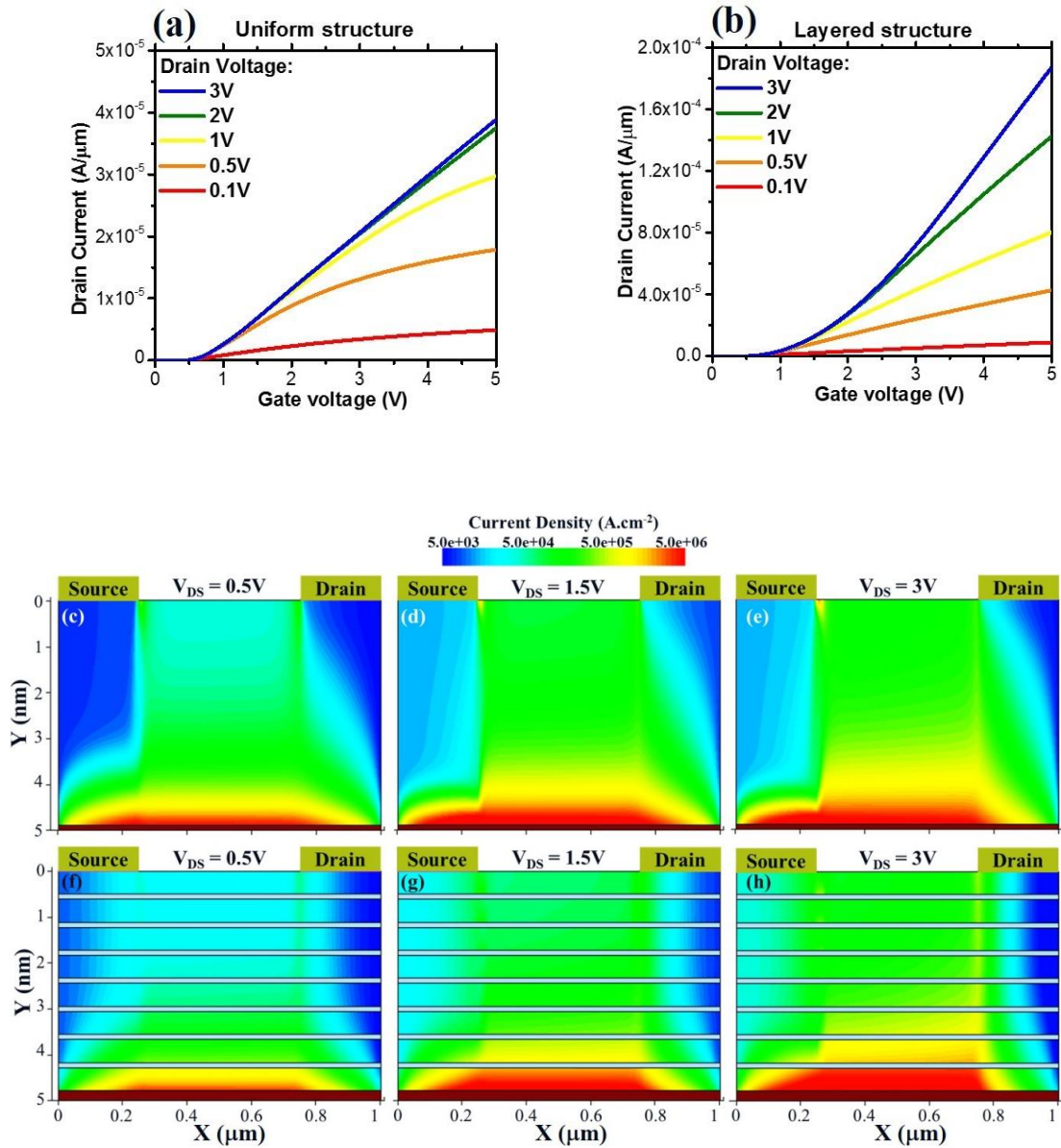


Figure 5: Transfer characteristic for the (a) uniform and (b) layered structure varying the drain voltage from 0.1 to 3V. Current density contour plot varying the drain voltage from 0.5 to 3V for the (c-e) uniform and (f-h) layered structure. Gate voltage is 5V ($V_{GS}-V_T \cong 3V$).

7.4 METHODOLOGY IMPROVEMENT

Although the model developed in the previous paragraphs is valid, a possible improvement is related to the tunnelling model used for the vertical tunnelling through the VdW-gaps. As said, the model used is the Schenk model,²⁸⁰ which is a “local

model". This means that only tunnelling of carriers at the interface can participate to the tunnelling current. Another choice is to use a non-local model. In this case the software creates a non-local mesh around the interface and will consider the tunnelling current from each mesh point created. In the MoS₂ case, this means that the tunnelling current will come from the all semiconductive layer, not only from the VdW-gap/MoS₂ interface.

The advantage of the model is also related to the fact that the vertical tunnelling mass and the conduction mass can be defined separately. The conduction mass can be set considering theoretical studies, as shown before in Chapter 6.3, while the vertical mass is a new parameter that can be tuned to match the experimental values. Other parameters as Schottky barrier and MoS₂ dielectric constant will be initially considered as 0.3 eV and 3 respectively considering the results from the previous fitting (Chapter 7.2) and tuned further if needed.

Figure 6a show the fitting of the experimental data considering a variation of thickness for the MoS₂ layer from 0.25 to 0.5 nm. Because the model considers the whole MoS₂ layer as tunnelling region, the current is generally larger at the same thickness with respect of the local model. Interestingly, considering the trend, a thickness between 0.3 and 0.4 nm is close to fit the experimental data. The other parameter to consider is the effective vertical mass, which trend is reported in Figure 6b, where a thickness of 0.32 nm for the MoS₂ was considered. The experimental data are well fitted considering a thickness for the MoS₂ of 0.32 nm and vertical mass of 0.2 m_0 . The value of 0.32 nm for the MoS₂ is the same as the sulphur-to-sulphur distance, while the 0.2 m_0 is very close to the value 0.18 m_0 extracted

experimentally.²⁸¹ It was not necessary to change the dielectric constant or the Schottky barrier from their initial values of 3 and 0.3 eV, respectively.

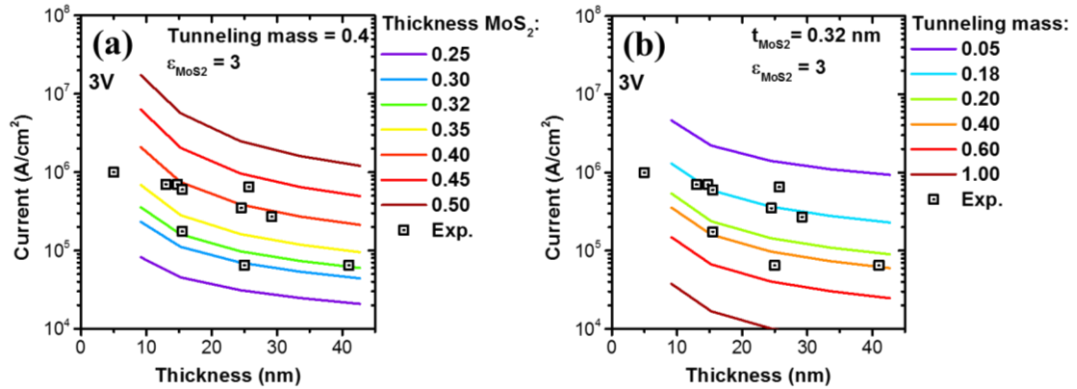


Figure 6: Current density at 3V for different thickness considering a variation of: (a) MoS₂ thickness with a fixed tunneling mass of 0.4, and (b) tunneling mass with a fixed thickness for the MoS₂ layer of 0.32 nm.

7.5 JUNCTIONLESS AND INVERSION-MODE TRANSISTORS

Considering the developed model is now possible to answer important questions regarding the potential application of MoS₂ in scaled devices for future electronics, focusing on two main architectures, the junctionless transistor (JNT)^{181, 265} and the classic inversion mode transistor (IM).

JNTs are characterised by uniform high doping throughout the channel and have been demonstrated in polysilicon, germanium, GaAs and indium-tin-oxide (ITO).²⁸⁵⁻²⁸⁸ One of the main advantages is its very simple architecture. Due to the uniform doping it is not necessary to define doped contact regions, which simplify the associated processing. In addition, the electric field perpendicular to the current flow for the device around the threshold voltage is lower than a corresponding inversion-mode or accumulation-mode transistors. This is advantageous as carrier mobility degrades with the perpendicular electric field.²⁸⁹

Therefore, it is very important to compare inversion and junctionless transistor architecture to understand which device architecture is most suited for TMD-based devices. Currently, due to the immaturity of the material system, systematic experiments comparing an inversion-mode with a junctionless transistor architecture would be very complicated, because a consistent growth technique, a reliable doping method and a good semiconductor oxide-TMD interface are needed. Although promising results have been shown in literature, the research is still at an early stage. On this matter, TCAD simulations are a useful tool in order to assess the device performance in a timely manner. However, it is also important to consider that the material parameters on which the TCAD model is based on come from theoretical studies which might not be accurate and are sometimes not consistent between each other. For example, the effective mass calculated by advanced calculations and shown before (Chapter 6, Figure 2d) show a certain variation between the different references, which will in turn introduce a certain error in the TCAD model as well. Although these results will inevitably be affected by these small uncertainties, they can be considered as a first step towards the understanding of 2D-FET at scaled dimensions.

Hence, a series of TCAD simulations are carried out considering 3 layers of MoS₂. The reason of choosing this thickness is because experimental data have shown a better mobility and contact resistance with respect to thinner devices. Therefore, in terms of scaled devices it is likely that 3-5 layers of MoS₂ might be preferred to 1-2 layers.

Figure 7 show the architecture schematics that will be considered. As said, one is the classic “Inversion Mode” (IM) transistor, where the channel is undoped and the contact regions are highly doped. This structure is similar to what shown by Kappera et al.²¹³ The second one is the JNT architecture, in which the doping concentration is uniformly distributed. The doping will vary between 6×10^{18} and $4 \times 10^{19} \text{ cm}^{-3}$. This structure is similar to those works where MoS_2 was doped by high- k , chemically or by substitutional doping, as the doping interested the whole channel. Both these architectures will be considered in a single-gate (SG) and double-gate (DG) configuration. Due to the low thickness of the channel the DG mode can be considered close to a gate-all-around architecture. The density of states, energy gap and all the parameters for the MoS_2 are detailed in Chapter 6.3. The equivalent oxide thickness (EOT) is 1 nm. The parameters varied are the spacer length (from 3 to 7 nm) and the gate length (8 to 20 nm).¹⁰⁹ The ITRS roadmap was used as guideline to set these

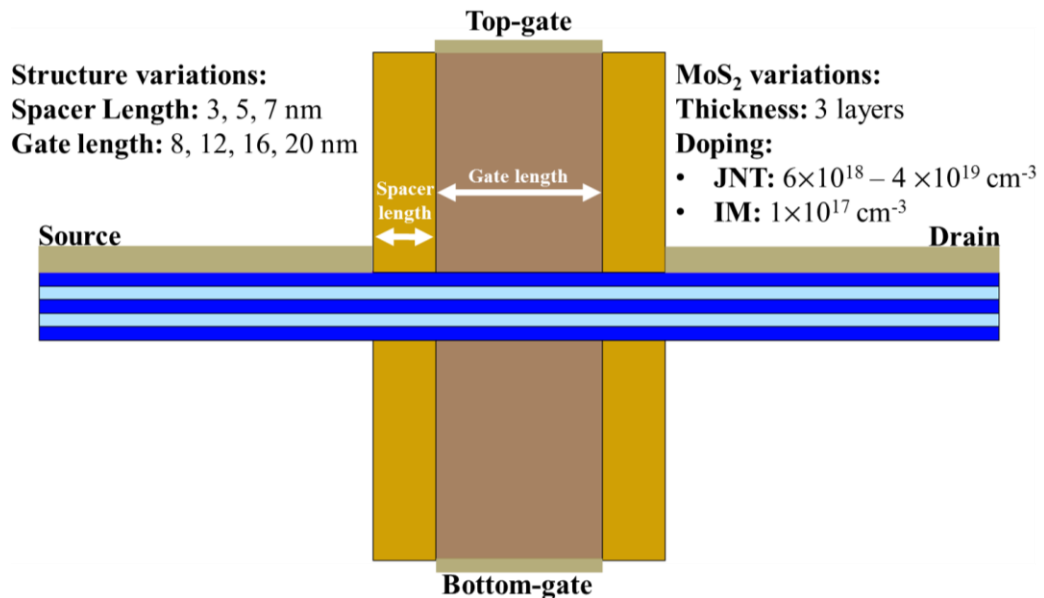


Figure 7: Double gate device structure considered for the TCAD simulations. For the IM architecture the source and drain regions will be considered metallic, while the channel will be uniformly doped for the JNT structure.
 values.¹⁰⁹

Figure 8 shows the mobility model adopted for the simulations. The Arora model²⁷⁰ was tuned considering mobility values in the low and high doping regime. It was assumed a mobility of $100 \text{ cm}^2/\text{V.s}$ in the case of low doping ($<10^{17} \text{ cm}^{-3}$). This upper limit in the low-doping regime was set considering recent studies where these mobility values were extracted from nominally undoped MoS_2 crystals with optimised contacts.²²⁵ The mobility at high doping concentration was set considering the experimental values from Chapter 4. Even if these data refer to p-type mobility, the p- and n-type mobility are very close considering heavily doped semiconductors

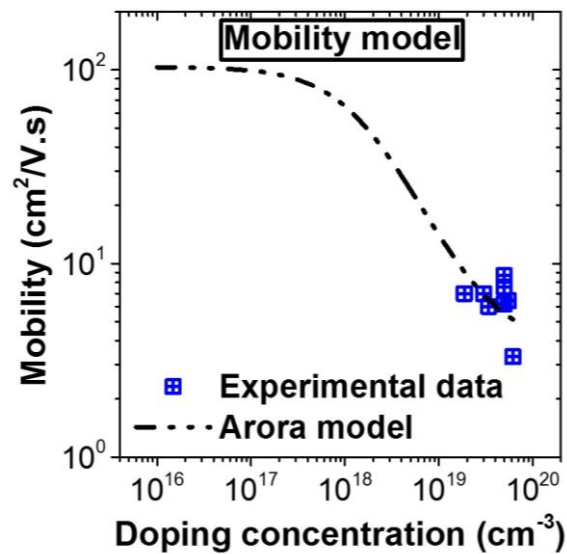


Figure 8: Mobility model used for the electrical simulations. The Arora model was tuned assuming a mobility value of $\sim 100 \text{ cm}^2/\text{V.s}$ for a doping concentration of 10^{17} cm^{-3} and the experimental data from Chapter 4 for the high-doping region.

Figure 9a and 9b compare the subthreshold slope (SS) and the drain-induced barrier lowering (DIBL) for the IM and JNT architectures. In both cases the values are very close considering a SG mode. Below 12 nm the SS values exceeds the requirement of the IRDS roadmap for both the JNT and the IM architecture. The DIBL is slightly less for a SG-JNT architecture, although in both cases the values are lower with respect of the ITRS requirements. Instead, considering a DG mode, the JNT

architecture can respect the IRDS standard at a channel length of 8 nm, while the IM architecture is slightly over 65 mV/dec. Although the DIBL values are similar, the ones related to the JNT architecture are lower.

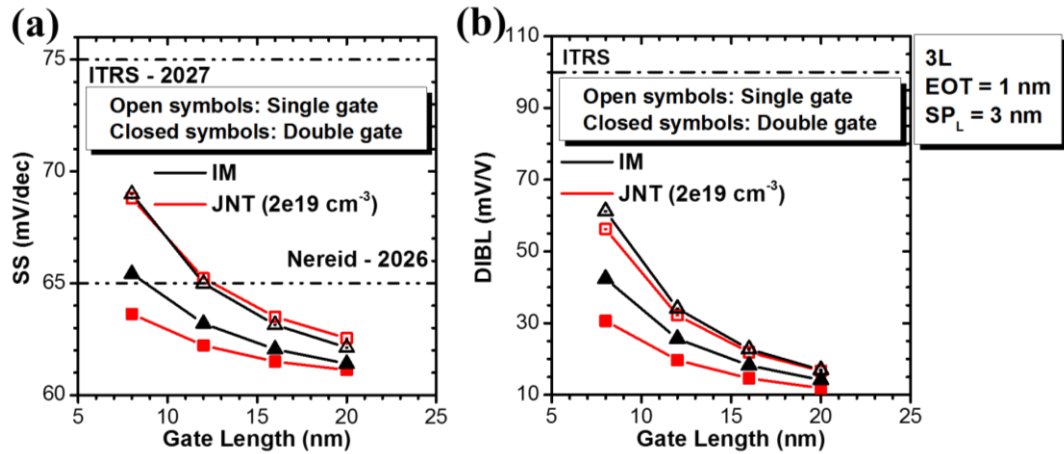


Figure 9: Comparison of JNT and IM in a single and double gate architecture considering (a) subthreshold slope and (b) DIBL. Same legend applied to both plots.

A second important parameter is the I_{ON} of the device. Usually, considering the target application the I_{OFF} is fixed at a certain value and the I_{ON} is the value of current at $V_{GS}=V_{DS}=V_{DD}$, where V_{DD} is the operating voltage. In this case the DG mode is chosen. Figure 10a shows the I_{ON} current versus gate length for the IM and JNT architectures. For the JNT data two doping concentrations are considered: 6×10^{18} and $4 \times 10^{19} \text{ cm}^{-3}$. For a higher doping concentration, the I_{ON} decreases. As said, the mobility model chosen for the JNT architecture is a doping-dependent mobility model. A lower doping will guarantee a higher mobility and so better I_{ON} . For the same reason the IM values are always higher. For a doping concentration of 10^{17} cm^{-3} the mobility is $\sim 100 \text{ cm}^2/\text{V}\cdot\text{s}$.

Figure 10b compare the JNT and the IM architecture at a channel length of 8 nm and spacer length of 3 nm. The dashed lines are the values of I_{ON} from the IRDS

roadmap: 420-470 $\mu\text{A}/\mu\text{m}$ at an I_{OFF} of 10^{-8} $\text{A}/\mu\text{m}$ at a V_{DD} of 0.7 or 0.65 V. Considering this, the green box shows the region where this condition is respected. Due to the higher mobility of the IM architecture the I_{ON} current is higher with respect of the JNT architecture (doping = 2×10^{19} cm^{-3}). The V_{DD} is varied from 0.7 to 0.6 V. Nonetheless, the IRDS condition is respected in a very small window.

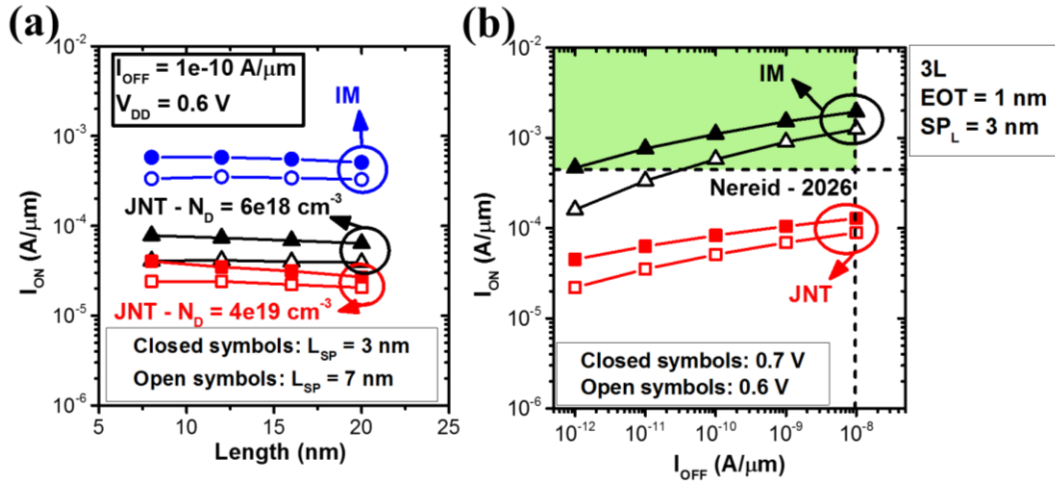


Figure 10: (a) I_{ON} scaling versus length at $V_{\text{DD}} = 0.6$ V for an I_{OFF} of 1×10^{-10} $\text{A}/\mu\text{m}$ and varying the spacer length between 3 and 7 nm. The IM architecture can drive a current almost one order of magnitude higher with respect of the JNT architecture. (b) I_{ON} versus I_{OFF} comparison at a V_{DD} of 0.6 and 0.7 V for the IM and JNT architecture at a channel length of 8 nm. The green box shows the $I_{\text{ON}}/I_{\text{OFF}}$ region where the condition set by the IRDS is respected.

7.6 DISCUSSION

In order to improve the drive current and satisfy the I_{ON} requirements at short channel lengths is necessary to increase the mobility of the material. In particular, comparing the IM and JNT architectures, the IM mode shows a higher current because of the lower doping and so higher mobility, which might make them the preferable architecture. Nonetheless, the mobility of highly doped 2D-semiconductors might still be increased by other factors. A solution previously adopted for 3D-semiconductors and currently in use in the semiconductor industry is stress engineering.²⁹⁰ Although previous theoretical studies have shown that strain can induce a higher mobility in

MoS₂ or similar TMDs,^{111, 291, 292} it is important to consider that a higher mobility is connected with a lower effective mass, which in turn might deteriorate the I_{OFF} or the SS of the device. A similar problem might be solved by the opportune deposition of high-*k* on TMD. Both theoretical and experimental studies have shown how the effect of a high-*k* can modify the properties of MoS₂, improving mobility, as discussed in more detail in Chapter 4 and 6, and reducing contact resistance and variability.⁹²

The double-gate architectures modelled in the previous paragraph present both very interesting characteristics in terms of SS and DIBL, which makes MoS₂ (or other 2D-semiconductors) a good candidate for scaled devices. The FinFET architecture currently in use might have reached the end for high performance devices after the 5 nm node²⁹³ and the most common substitutes considered nowadays to match the requirements for advanced technology nodes are the nanosheet²⁹⁴ or nanowire²⁹⁵ transistors. Nanowires appear as an interesting choice because of the better control with respect of the FinFET architecture. However, they suffer more from scattering and quantization effects due to their small diameter.¹⁶⁰ Both theoretical and experimental studies have shown that nanosheets can outperform nanowire-based FETs.^{165, 294, 296} Although 2D-semiconductors are as well affected by quantization effects, they can still maintain considerable performances even at low dimensions, which can make them possible candidates for future electronics. Physical compact models identified WS₂ as a promising candidate to meet the 3 nm node requirements, outperforming Si FinFET in term of electrostatic and energy performances.²⁹⁷ In addition, due to their intrinsic 2D-nature, MoS₂ FET were shown to have ~50% lower parasitic capacitance with respect of Si FinFET.²⁹⁸ This advantage can be useful in order to reduce further the spacer, contact and channel lengths for higher integration, or relax these dimensions for improved performances.

7.7 CONCLUSIONS

With a combination of experimental findings and theoretical results a physics-based layered structure model was developed for MoS₂. Considering previous reports on the perpendicular conduction in MoS₂ devices, a layered structure that considers both the semiconducting layers of MoS₂ and the Van-der-Waals gaps in between them was developed and optimized for the first time in a TCAD software. The model was then used to shed light on the current distribution in a back-gated MoS₂-based FET and on the scaling behavior of inversion-mode and junctionless FETs. The junctionless transistor architecture, is comparable to the more common inversion-mode architecture in terms of DIBL or SS. However, the high doping required for the junctionless architecture causes a lower mobility, deteriorating the I_{ON} of the device compared to the inversion mode structure. Stress engineering or high-k deposition might be necessary in order to utilize this junctionless architecture.

Chapter 8: CONCLUSIONS AND FUTURE PERSPECTIVES

The properties and characteristics of 2D-Semiconductors make them very interesting for applications in future electronics. However, certain issues need to be resolved and solutions need to be found.

Air sensitivity is a major problem for certain 2D-semiconductors. Five different TMDs were studied over a period of 30 days and MoS₂ resulted to be the most stable among them. On the contrary HfSe₂ is highly unstable. After one day from exfoliation the surface is characterized by Se-rich blisters and an oxidized surface. The high reactivity of this material poses severe challenges on its use in future applications. In order to use more air-sensitive TMDs in future applications, their degradation needs to be contained. Chemical functionalisation or passivation methods can be interesting solutions, but they need to be optimised to protect the surface from exposure.

Due to the immaturity of the material growth, the mobility of 2D-semiconductors is limited by impurities. Both numerical and SIMS analysis showed a high concentration of a wide range of impurities in exfoliated crystals, which highly degraded the mobility and the electrical performance of TMD-based FETs. This might be solved by more sophisticated growth techniques, as CVD or ALD. In addition, due to the low thickness of the materials, the dielectric environment plays an important role on their electrical performances.

In terms of FET-applications, contact resistance is probably the most important bottleneck to date. In the case of MoS₂, it was shown that high-doping concentration can be an optimum way to reduce contact resistance. The results are comparable with both the roadmap for semiconductors (IRDS) and with literature. In the case of PtSe₂, forming gas annealing was shown to cause a reaction between the metal and the PtSe₂. The 3D-alloy formed can be important for contact resistance optimization. An optimum contact behavior can be achieved by the opportune combination of both these techniques. However, a reliable doping technique needs to be developed for TMDs. Substitutional doping might be introduced only during the growth of the material, therefore chemical or high-k doping might be optimal solutions. In addition, certain pair metal-TMDs might be used to form a TMD-metal 3D-alloy.

Finally, TCAD modelling is an important tool to further study and understand the behavior of new material systems. The model was improved introducing VdW-gaps in the structures and tuning the vertical transport with experimental results. The TCAD model was then used to study the behavior of MoS₂-based scaled FETs. Future studies can focus on the optimization of the model by more advanced tools, as quantum Monte Carlo or density functional theory simulations, as well as a proper tuning of more accurate material parameters.

References

1. Brinkman, W. F.; Haggan, D. E.; Troutman, W. W., A history of the invention of the transistor and where it will lead us. *IEEE Journal of Solid-State Circuits* **1997**, *32* (12), 1858-1865.
2. Moore, G. E., Cramming more components onto integrated circuits. *Proceedings of the IEEE* **1998**, *86* (1), 82-85.
3. Dennard, R. H.; Gaensslen, F. H.; Rideout, V. L.; Bassous, E.; LeBlanc, A. R., Design of ion-implanted MOSFET's with very small physical dimensions. *IEEE Journal of Solid-State Circuits* **1974**, *9* (5), 256-268.
4. Schwierz, F., Graphene transistors. *Nature nanotechnology* **2010**, *5* (7), 487.
5. Ferain, I.; Colinge, C. A.; Colinge, J.-P., Multigate transistors as the future of classical metal–oxide–semiconductor field-effect transistors. *Nature* **2011**, *479* (7373), 310.
6. Moore, G. E. In *No exponential is forever: but "Forever" can be delayed!*[semiconductor industry], 2003 IEEE International Solid-State Circuits Conference, 2003. Digest of Technical Papers. ISSCC., IEEE: 2003; pp 20-23.
7. Thompson, S.; Anand, N.; Armstrong, M.; Auth, C.; Arcot, B.; Alavi, M.; Bai, P.; Bielefeld, J.; Bigwood, R.; Brandenburg, J. In *A 90 nm logic technology featuring 50 nm strained silicon channel transistors, 7 layers of Cu interconnects, low k ILD, and 1/spl mu/m/sup 2/SRAM cell*, Digest. International Electron Devices Meeting, IEEE: 2002; pp 61-64.
8. Mistry, K.; Allen, C.; Auth, C.; Beattie, B.; Bergstrom, D.; Bost, M.; Brazier, M.; Buehler, M.; Cappellani, A.; Chau, R. In *A 45nm logic technology with high-k+ metal gate transistors, strained silicon, 9 Cu interconnect layers, 193nm dry patterning, and 100% Pb-free packaging*, 2007 IEEE International Electron Devices Meeting, IEEE: 2007; pp 247-250.
9. Auth, C.; Allen, C.; Blattner, A.; Bergstrom, D.; Brazier, M.; Bost, M.; Buehler, M.; Chikarmane, V.; Ghani, T.; Glassman, T. In *A 22nm high performance and low-power CMOS technology featuring fully-depleted tri-gate transistors, self-aligned contacts and high density MIM capacitors*, 2012 Symposium on VLSI Technology (VLSIT), IEEE: 2012; pp 131-132.
10. Nowak, E. J., Maintaining the benefits of CMOS scaling when scaling bogs down. *IBM Journal of Research and Development* **2002**, *46* (2.3), 169-180.
11. Novoselov, K. S.; Geim, A. K.; Morozov, S. V.; Jiang, D.; Zhang, Y.; Dubonos, S. V.; Grigorieva, I. V.; Firsov, A. A., Electric field effect in atomically thin carbon films. *science* **2004**, *306* (5696), 666-669.
12. Jiang, J.; Chu, J. H.; Banerjee, K. In *CMOS-compatible doped-multilayer-graphene interconnects for next-generation VLSI*, 2018 IEEE International Electron Devices Meeting (IEDM), IEEE: 2018; pp 34.5. 1-34.5. 4.
13. Kuc, A.; Zibouche, N.; Heine, T., Influence of quantum confinement on the electronic structure of the transition metal sulfide TS₂. *Physical Review B* **2011**, *83* (24), 245213.
14. Yazyev, O. V.; Kis, A., MoS₂ and semiconductors in the flatland. *Materials Today* **2015**, *18* (1), 20-30.
15. Chhowalla, M.; Jena, D.; Zhang, H., Two-dimensional semiconductors for transistors. *Nature Reviews Materials* **2016**, *1* (11), 16052.

-
16. Fiori, G.; Bonaccorso, F.; Iannaccone, G.; Palacios, T.; Neumaier, D.; Seabaugh, A.; Banerjee, S. K.; Colombo, L., Electronics based on two-dimensional materials. *Nature nanotechnology* **2014**, *9* (10), 768.
 17. Manzeli, S.; Ovchinnikov, D.; Pasquier, D.; Yazyev, O. V.; Kis, A., 2D transition metal dichalcogenides. *Nature Reviews Materials* **2017**, *2* (8), 17033.
 18. Silva-Guillén, J.; San-Jose, P.; Roldán, R., Electronic Band Structure of Transition Metal Dichalcogenides from Ab Initio and Slater–Koster Tight-Binding Model. *Applied Sciences* **2016**, *6* (10), 284.
 19. Serov, A. Y.; Dorgan, V. E.; English, C. D.; Pop, E. In *Multi-valley high-field transport in 2-dimensional MoS₂ transistors*, 72nd Device Research Conference, IEEE: 2014; pp 183-184.
 20. Beal, A.; Hughes, H.; Liang, W., The reflectivity spectra of some group VA transition metal dichalcogenides. *Journal of physics C: solid state physics* **1975**, *8* (24), 4236.
 21. Wilson, J. A.; Di Salvo, F.; Mahajan, S., Charge-density waves and superlattices in the metallic layered transition metal dichalcogenides. *Advances in Physics* **1975**, *24* (2), 117-201.
 22. Ding, Y.; Wang, Y.; Ni, J.; Shi, L.; Shi, S.; Tang, W., First principles study of structural, vibrational and electronic properties of graphene-like MX₂ (M= Mo, Nb, W, Ta; X= S, Se, Te) monolayers. *Physica B: Condensed Matter* **2011**, *406* (11), 2254-2260.
 23. Mak, K. F.; Lee, C.; Hone, J.; Shan, J.; Heinz, T. F., Atomically thin MoS₂: a new direct-gap semiconductor. *Physical review letters* **2010**, *105* (13), 136805.
 24. Kam, K.; Parkinson, B., Detailed photocurrent spectroscopy of the semiconducting group VIB transition metal dichalcogenides. *The Journal of Physical Chemistry* **1982**, *86* (4), 463-467.
 25. Liu, L.; Kumar, S. B.; Ouyang, Y.; Guo, J., Performance limits of monolayer transition metal dichalcogenide transistors. *IEEE Transactions on Electron Devices* **2011**, *58* (9), 3042-3047.
 26. Gmelin, L., *Gmelin Handbook of inorganic and organometallic chemistry: Sn--Organotin compounds*. Springer Verlag: 1975.
 27. Wang, Q. H.; Kalantar-Zadeh, K.; Kis, A.; Coleman, J. N.; Strano, M. S., Electronics and optoelectronics of two-dimensional transition metal dichalcogenides. *Nature nanotechnology* **2012**, *7* (11), 699.
 28. Ouyang, B.; Lan, G.; Guo, Y.; Mi, Z.; Song, J., Phase engineering of monolayer transition-metal dichalcogenide through coupled electron doping and lattice deformation. *Applied Physics Letters* **2015**, *107* (19), 191903.
 29. Novoselov, K. S.; Jiang, D.; Schedin, F.; Booth, T. J.; Khotkevich, V. V.; Morozov, S. V.; Geim, A. K., Two-dimensional atomic crystals. *Proceedings of the National Academy of Sciences of the United States of America* **2005**, *102* (30), 10451-10453.
 30. Radisavljevic, B.; Radenovic, A.; Brivio, J.; Giacometti, V.; Kis, A., Single-layer MoS₂ transistors. *Nature Nanotechnology* **2011**, *6*, 147.
 31. Hu, D.; Xu, G.; Xing, L.; Yan, X.; Wang, J.; Zheng, J.; Lu, Z.; Wang, P.; Pan, X.; Jiao, L., Two-Dimensional Semiconductors Grown by Chemical Vapor Transport. *Angewandte Chemie International Edition* **2017**, *56* (13), 3611-3615.
 32. Mleczko, M. J.; Xu, R. L.; Okabe, K.; Kuo, H.-H.; Fisher, I. R.; Wong, H. S. P.; Nishi, Y.; Pop, E., High Current Density and Low Thermal Conductivity of Atomically Thin Semimetallic WTe₂. *ACS Nano* **2016**, *10* (8), 7507-7514.

-
33. Walsh, L. A.; Addou, R.; Wallace, R. M.; Hinkle, C. L., *Chapter 22 - Molecular Beam Epitaxy of Transition Metal Dichalcogenides*. Elsevier: 2018; p 515-531.
34. Roy, A.; Movva, H. C. P.; Satpati, B.; Kim, K.; Dey, R.; Rai, A.; Pramanik, T.; Guchhait, S.; Tutuc, E.; Banerjee, S. K., Structural and Electrical Properties of MoTe₂ and MoSe₂ Grown by Molecular Beam Epitaxy. *ACS Applied Materials & Interfaces* **2016**, *8* (11) 7396-7402.
35. Xia, J.; Huang, X.; Liu, L.-Z.; Wang, M.; Wang, L.; Huang, B.; Zhu, D.-D.; Li, J.-J.; Gu, C.-Z.; Meng, X.-M., CVD synthesis of large-area, highly crystalline MoSe₂ atomic layers on diverse substrates and application to photodetectors. *Nanoscale* **2014**, *6* (15), 8949-8955.
36. Schmidt, H.; Wang, S.; Chu, L.; Toh, M.; Kumar, R.; Zhao, W.; Castro Neto, A. H.; Martin, J.; Adam, S.; Özyilmaz, B.; Eda, G., Transport Properties of Monolayer MoS₂ Grown by Chemical Vapor Deposition. *Nano Letters* **2014**, *14* (4), 1909-1913.
37. Elías, A. L.; Perea-López, N.; Castro-Beltrán, A.; Berkdemir, A.; Lv, R.; Feng, S.; Long, A. D.; Hayashi, T.; Kim, Y. A.; Endo, M.; Gutiérrez, H. R.; Pradhan, N. R.; Balicas, L.; Mallouk, T. E.; López-Urías, F.; Terrones, H.; Terrones, M., Controlled Synthesis and Transfer of Large-Area WS₂ Sheets: From Single Layer to Few Layers. *ACS Nano* **2013**, *7* (6), 5235-5242.
38. Kang, K.; Xie, S.; Huang, L.; Han, Y.; Huang, P. Y.; Mak, K. F.; Kim, C.-J.; Muller, D.; Park, J., High-mobility three-atom-thick semiconducting films with wafer-scale homogeneity. *Nature* **2015**, *520*, 656.
39. Bergeron, H.; Sangwan, V. K.; McMorrow, J. J.; Campbell, G. P.; Balla, I.; Liu, X.; Bedzyk, M. J.; Marks, T. J.; Hersam, M. C., Chemical vapor deposition of monolayer MoS₂ directly on ultrathin Al₂O₃ for low-power electronics. *Applied Physics Letters* **2017**, *110* (5), 053101.
40. Valdivia, A.; Tweet, D. J.; Jr., J. F. C., Atomic layer deposition of two dimensional MoS₂ on 150 mm substrates. *Journal of Vacuum Science & Technology A* **2016**, *34* (2), 021515.
41. Browning, R.; Padigi, P.; Solanki, R.; Tweet, D. J.; Schuele, P.; Evans, D., Atomic layer deposition of MoS₂ thin films. *Materials Research Express* **2015**, *2* (3), 035006.
42. Tan, L. K.; Liu, B.; Teng, J. H.; Guo, S.; Low, H. Y.; Loh, K. P., Atomic layer deposition of a MoS₂ film. *Nanoscale* **2014**, *6* (18), 10584-10588.
43. Nandi, D. K.; Sen, U. K.; Choudhury, D.; Mitra, S.; Sarkar, S. K., Atomic Layer Deposited MoS₂ as a Carbon and Binder Free Anode in Li-ion Battery. *Electrochimica Acta* **2014**, *146*, 706-713.
44. Kwon, D. H.; Jin, Z.; Shin, S.; Lee, W.-S.; Min, Y.-S., A comprehensive study on atomic layer deposition of molybdenum sulfide for electrochemical hydrogen evolution. *Nanoscale* **2016**, *8* (13), 7180-7188.
45. Jin, Z.; Shin, S.; Kwon, D. H.; Han, S.-J.; Min, Y.-S., Novel chemical route for atomic layer deposition of MoS₂ thin film on SiO₂/Si substrate. *Nanoscale* **2014**, *6* (23), 14453-14458.
46. Jurca, T.; Moody, M. J.; Henning, A.; Emery, J. D.; Wang, B.; Tan, J. M.; Lohr, T. L.; Lauhon, L. J.; Marks, T. J., Low-Temperature Atomic Layer Deposition of MoS₂ Films. *Angewandte Chemie International Edition* **2017**, *56* (18), 4991-4995.
47. Lee, K.; Gatensby, R.; McEvoy, N.; Hallam, T.; Duesberg, G. S., High-Performance Sensors Based on Molybdenum Disulfide Thin Films. *Advanced Materials* **2013**, *25* (46), 6699-6702.

-
48. Duffy, R.; Foley, P.; Filippone, B.; Mirabelli, G.; O'Connell, D.; Sheehan, B.; Carolan, P.; Schmidt, M.; Cherkaoui, K.; Gatensby, R.; Hallam, T.; Duesberg, G.; Crupi, F.; Nagle, R.; Hurley, P. K., Structural and Electrical Investigation of MoS₂ Thin Films Formed by Thermal Assisted Conversion of Mo Metal. *ECS Journal of Solid State Science and Technology* **2016**, 5 (11), Q3016-Q3020.
49. Yim, C.; Lee, K.; McEvoy, N.; O'Brien, M.; Riazimehr, S.; Berner, N. C.; Cullen, C. P.; Kotakoski, J.; Meyer, J. C.; Lemme, M. C.; Duesberg, G. S., High-Performance Hybrid Electronic Devices from Layered PtSe₂ Films Grown at Low Temperature. *ACS Nano* **2016**, 10 (10), 9550-9558.
50. O'Brien, M.; McEvoy, N.; Motta, C.; Zheng, J.-Y.; Berner, N. C.; Kotakoski, J.; Elibol, K.; Pennycook, T. J.; Meyer, J. C.; Yim, C.; Abid, M.; Hallam, T.; Donegan, J. F.; Sanvito, S.; Duesberg, G. S., Raman characterization of platinum diselenide thin films. *2D Materials* **2016**, 3 (2), 021004.
51. Sedky, S.; Witvrouw, A.; Bender, H.; Baert, K., Experimental determination of the maximum post-process annealing temperature for standard CMOS wafers. *IEEE Transactions on Electron Devices* **2001**, 48 (2), 377-385.
52. Takeuchi, H.; Wung, A.; Xin, S.; Howe, R. T.; Tsu-Jae, K., Thermal budget limits of quarter-micrometer foundry CMOS for post-processing MEMS devices. *IEEE Transactions on Electron Devices* **2005**, 52 (9), 2081-2086.
53. Lee, Y. H. D.; Lipson, M., Back-End Deposited Silicon Photonics for Monolithic Integration on CMOS. *IEEE Journal of Selected Topics in Quantum Electronics* **2013**, 19 (2), 8200207-8200207.
54. Greene, J. E.; Barnett, S. A.; Rockett, A.; Bajor, G., Modeling of dopant incorporation, segregation, and ion/surface interaction effects during semiconductor film growth by molecular beam epitaxy and plasma-based techniques. *Applications of Surface Science* **1985**, 22-23, 520-544.
55. Yue, R.; Barton, A. T.; Zhu, H.; Azcatl, A.; Pena, L. F.; Wang, J.; Peng, X.; Lu, N.; Cheng, L.; Addou, R.; McDonnell, S.; Colombo, L.; Hsu, J. W. P.; Kim, J.; Kim, M. J.; Wallace, R. M.; Hinkle, C. L., HfSe₂ Thin Films: 2D Transition Metal Dichalcogenides Grown by Molecular Beam Epitaxy. *ACS Nano* **2015**, 9 (1), 474-480.
56. Yue, R.; Nie, Y.; Walsh, L. A.; Addou, R.; Liang, C.; Lu, N.; Barton, A. T.; Zhu, H.; Che, Z.; Barrera, D.; Cheng, L.; Cha, P.-R.; Chabal, Y. J.; Hsu, J. W. P.; Kim, J.; Kim, M. J.; Colombo, L.; Wallace, R. M.; Cho, K.; Hinkle, C. L., Nucleation and growth of WSe₂: enabling large grain transition metal dichalcogenides. *2D Materials* **2017**, 4 (4), 045019.
57. Huyghebaert, C.; Schram, T.; Smets, Q.; Agarwal, T. K.; Verreck, D.; Brems, S.; Phommahaxay, A.; Chiappe, D.; Kazzi, S. E.; Rosa, C. L. d. l.; Arutchelvan, G.; Cott, D.; Ludwig, J.; Gaur, A.; Sutar, S.; Leonhardt, A.; Marinov, D.; Lin, D.; Caymax, M.; Asselberghs, I.; Pourtois, G.; Radu, I. P. In *2D materials: roadmap to CMOS integration*, 2018 IEEE International Electron Devices Meeting (IEDM), 1-5 Dec. 2018; 2018; pp 22.1.1-22.1.4.
58. Dumcenco, D.; Ovchinnikov, D.; Marinov, K.; Lazić, P.; Gibertini, M.; Marzari, N.; Sanchez, O. L.; Kung, Y.-C.; Krasnozhan, D.; Chen, M.-W.; Bertolazzi, S.; Gillet, P.; Fontcuberta i Morral, A.; Radenovic, A.; Kis, A., Large-Area Epitaxial Monolayer MoS₂. *ACS Nano* **2015**, 9 (4), 4611-4620.
59. Shin, B. G.; Han, G. H.; Yun, S. J.; Oh, H. M.; Bae, J. J.; Song, Y. J.; Park, C.-Y.; Lee, Y. H., Indirect Bandgap Puddles in Monolayer MoS₂ by Substrate-Induced Local Strain. *Advanced Materials* **2016**, 28 (42), 9378-9384.
60. He, K.; Kumar, N.; Zhao, L.; Wang, Z.; Mak, K. F.; Zhao, H.; Shan, J., Tightly Bound Excitons in Monolayer WSe₂. *Physical Review Letters* **2014**, 113 (2), 026803.

-
61. Mak, K. F.; McGill, K. L.; Park, J.; McEuen, P. L., The valley Hall effect in MoS₂ transistors. *Science* **2014**, *344* (6191), 1489.
62. Fortin, E.; Sears, W. M., Photovoltaic effect and optical absorption in MoS₂. *Journal of Physics and Chemistry of Solids* **1982**, *43* (9), 881-884.
63. Pradhan, S. K.; Xiao, B.; Pradhan, A. K., Enhanced photo-response in p-Si/MoS₂ heterojunction-based solar cells. *Solar Energy Materials and Solar Cells* **2016**, *144*, 117-127.
64. Tsai, M.-L.; Su, S.-H.; Chang, J.-K.; Tsai, D.-S.; Chen, C.-H.; Wu, C.-I.; Li, L.-J.; Chen, L.-J.; He, J.-H., Monolayer MoS₂ Heterojunction Solar Cells. *ACS Nano* **2014**, *8* (8), 8317-8322.
65. Lin, S.; Li, X.; Wang, P.; Xu, Z.; Zhang, S.; Zhong, H.; Wu, Z.; Xu, W.; Chen, H., Interface designed MoS₂/GaAs heterostructure solar cell with sandwich stacked hexagonal boron nitride. *Scientific Reports* **2015**, *5*, 15103.
66. Wang, P.; Lin, S.; Ding, G.; Li, X.; Wu, Z.; Zhang, S.; Xu, Z.; Xu, S.; Lu, Y.; Xu, W.; Zheng, Z., Enhanced monolayer MoS₂/InP heterostructure solar cells by graphene quantum dots. *Applied Physics Letters* **2016**, *108* (16), 163901.
67. Lopez-Sanchez, O.; Alarcon Llado, E.; Koman, V.; Fontcuberta i Morral, A.; Radenovic, A.; Kis, A., Light Generation and Harvesting in a van der Waals Heterostructure. *ACS Nano* **2014**, *8* (3), 3042-3048.
68. Polman, A.; Atwater, H. A., Photonic design principles for ultrahigh-efficiency photovoltaics. *Nature Materials* **2012**, *11*, 174.
69. Zhang, W.; Huang, J.-K.; Chen, C.-H.; Chang, Y.-H.; Cheng, Y.-J.; Li, L.-J., High-Gain Phototransistors Based on a CVD MoS₂ Monolayer. *Advanced Materials* **2013**, *25* (25), 3456-3461.
70. Yin, Z.; Li, H.; Li, H.; Jiang, L.; Shi, Y.; Sun, Y.; Lu, G.; Zhang, Q.; Chen, X.; Zhang, H., Single-Layer MoS₂ Phototransistors. *ACS Nano* **2012**, *6* (1), 74-80.
71. Lopez-Sanchez, O.; Lembke, D.; Kayci, M.; Radenovic, A.; Kis, A., Ultrasensitive photodetectors based on monolayer MoS₂. *Nature Nanotechnology* **2013**, *8*, 497.
72. Chang, Y.-H.; Zhang, W.; Zhu, Y.; Han, Y.; Pu, J.; Chang, J.-K.; Hsu, W.-T.; Huang, J.-K.; Hsu, C.-L.; Chiu, M.-H.; Takenobu, T.; Li, H.; Wu, C.-I.; Chang, W.-H.; Wee, A. T. S.; Li, L.-J., Monolayer MoSe₂ Grown by Chemical Vapor Deposition for Fast Photodetection. *ACS Nano* **2014**, *8* (8), 8582-8590.
73. Abderrahmane, A.; Ko, P. J.; Thu, T. V.; Ishizawa, S.; Takamura, T.; Sandhu, A., High photosensitivity few-layered MoSe₂ back-gated field-effect phototransistors. *Nanotechnology* **2014**, *25* (36), 365202.
74. Perea-López, N.; Elías, A. L.; Berkdemir, A.; Castro-Beltran, A.; Gutiérrez, H. R.; Feng, S.; Lv, R.; Hayashi, T.; López-Urías, F.; Ghosh, S.; Muchharla, B.; Talapatra, S.; Terrones, H.; Terrones, M., Photosensor Device Based on Few-Layered WS₂ Films. *Advanced Functional Materials* **2013**, *23* (44), 5511-5517.
75. Huo, N.; Yang, S.; Wei, Z.; Li, S.-S.; Xia, J.-B.; Li, J., Photoresponsive and Gas Sensing Field-Effect Transistors based on Multilayer WS₂ Nanoflakes. *Scientific Reports* **2014**, *4*, 5209.
76. Zhang, W.; Chiu, M.-H.; Chen, C.-H.; Chen, W.; Li, L.-J.; Wee, A. T. S., Role of Metal Contacts in High-Performance Phototransistors Based on WSe₂ Monolayers. *ACS Nano* **2014**, *8* (8), 8653-8661.
77. Lee, H. S.; Min, S.-W.; Chang, Y.-G.; Park, M. K.; Nam, T.; Kim, H.; Kim, J. H.; Ryu, S.; Im, S., MoS₂ Nanosheet Phototransistors with Thickness-Modulated Optical Energy Gap. *Nano Letters* **2012**, *12* (7), 3695-3700.

-
78. Seabaugh, A., The Tunneling Transistor. *IEEE Spectrum* **2013**, 50 (10), 35-62.
79. Jena, D., Tunneling Transistors Based on Graphene and 2-D Crystals. *Proceedings of the IEEE* **2013**, 101 (7), 1585-1602.
80. Li, M.; Esseni, D.; Snider, G.; Jena, D.; Grace Xing, H., Single particle transport in two-dimensional heterojunction interlayer tunneling field effect transistor. *Journal of Applied Physics* **2014**, 115 (7), 074508.
81. Cao, J.; Logoteta, D.; Özkaya, S.; Biel, B.; Cresti, A.; Pala, M. G.; Esseni, D., Operation and Design of van der Waals Tunnel Transistors: A 3-D Quantum Transport Study. *IEEE Transactions on Electron Devices* **2016**, 63 (11), 4388-4394.
82. Pala, M. G.; Esseni, D., Interface Traps in InAs Nanowire Tunnel-FETs and MOSFETs—Part I: Model Description and Single Trap Analysis in Tunnel-FETs. *IEEE Transactions on Electron Devices* **2013**, 60 (9), 2795-2801.
83. Esseni, D.; Pala, M. G., Interface Traps in InAs Nanowire Tunnel FETs and MOSFETs—Part II: Comparative Analysis and Trap-Induced Variability. *IEEE Transactions on Electron Devices* **2013**, 60 (9), 2802-2807.
84. Li, M. O.; Esseni, D.; Nahas, J. J.; Jena, D.; Xing, H. G., Two-Dimensional Heterojunction Interlayer Tunneling Field Effect Transistors (Thin-TFETs). *IEEE Journal of the Electron Devices Society* **2015**, 3 (3), 200-207.
85. Sarkar, D.; Xie, X.; Liu, W.; Cao, W.; Kang, J.; Gong, Y.; Kraemer, S.; Ajayan, P. M.; Banerjee, K., A subthermionic tunnel field-effect transistor with an atomically thin channel. *Nature* **2015**, 526, 91.
86. NanoElectronics Roadmap for Europe (NEREID, 2018); <https://www.nereid-h2020.eu/roadmap>.
87. Yan, R.; Ourmazd, A.; Lee, K. F., Scaling the Si MOSFET: from bulk to SOI to bulk. *IEEE Transactions on Electron Devices* **1992**, 39 (7), 1704-1710.
88. Schwierz, F.; Pezoldt, J.; Granzner, R., Two-dimensional materials and their prospects in transistor electronics. *Nanoscale* **2015**, 7 (18), 8261-8283.
89. Li, X.; Mullen, J. T.; Jin, Z.; Borysenko, K. M.; Buongiorno Nardelli, M.; Kim, K. W., Intrinsic electrical transport properties of monolayer silicene and MoS₂ from first principles. *Physical Review B* **2013**, 87 (11), 115418.
90. Addou, R.; McDonnell, S.; Barrera, D.; Guo, Z.; Azcatl, A.; Wang, J.; Zhu, H.; Hinkle, C. L.; Quevedo-Lopez, M.; Alshareef, H. N.; Colombo, L.; Hsu, J. W. P.; Wallace, R. M., Impurities and Electronic Property Variations of Natural MoS₂ Crystal Surfaces. *ACS Nano* **2015**, 9 (9), 9124-9133.
91. Rai, A.; Movva, H. C. P.; Roy, A.; Taneja, D.; Chowdhury, S.; Banerjee, S. K., Progress in Contact, Doping and Mobility Engineering of MoS₂: An Atomically Thin 2D Semiconductor. *Crystals* **2018**, 8 (8), 316.
92. Ma, N.; Jena, D., Charge Scattering and Mobility in Atomically Thin Semiconductors. *Physical Review X* **2014**, 4 (1), 011043.
93. Reggiani, S.; Gnani, E.; Gnudi, A.; Rudan, M.; Baccarani, G., Low-Field Electron Mobility Model for Ultrathin-Body SOI and Double-Gate MOSFETs With Extremely Small Silicon Thicknesses. *IEEE Transactions on Electron Devices* **2007**, 54 (9), 2204-2212.
94. Badami, O.; Caruso, E.; Lizzit, D.; Osgnach, P.; Esseni, D.; Palestri, P.; Selmi, L., An Improved Surface Roughness Scattering Model for Bulk, Thin-Body, and Quantum-Well MOSFETs. *IEEE Transactions on Electron Devices* **2016**, 63 (6), 2306-2312.

-
95. Passlack, M.; Droopad, R.; Rajagopalan, K.; Abrokwah, J.; Zurcher, P.; Fejes, P. In *High Mobility III-V Mosfet Technology*, 2006 IEEE Compound Semiconductor Integrated Circuit Symposium, 12-15 Nov. 2006; 2006; pp 39-42.
96. del Alamo, J. A., Nanometre-scale electronics with III–V compound semiconductors. *Nature* **2011**, *479*, 317.
97. Kim, S.; Yokoyama, M.; Taoka, N.; Iida, R.; Lee, S.; Nakane, R.; Urabe, Y.; Miyata, N.; Yasuda, T.; Yamada, H.; Fukuhara, N.; Hata, M.; Takenaka, M.; Takagi, S., High Performance Extremely Thin Body InGaAs-on-Insulator Metal–Oxide–Semiconductor Field-Effect Transistors on Si Substrates with Ni–InGaAs Metal Source/Drain. *Applied Physics Express* **2011**, *4* (11), 114201.
98. MacHale, J.; Meaney, F.; Kennedy, N.; Eaton, L.; Mirabelli, G.; White, M.; Thomas, K.; Pelucchi, E.; Petersen, D. H.; Lin, R.; Petkov, N.; Connolly, J.; Hatem, C.; Gity, F.; Ansari, L.; Long, B.; Duffy, R., Exploring conductivity in ex-situ doped Si thin films as thickness approaches 5 nm. *Journal of Applied Physics* **2019**, *125* (22), 225709.
99. Uchida, K.; Junji, K.; Shin-ichi, T. In *Experimental study on carrier transport mechanisms in double- and single-gate ultrathin-body MOSFETs - Coulomb scattering, volume inversion, and ΔT SOI-induced scattering*, IEEE International Electron Devices Meeting 2003, 8-10 Dec. 2003; 2003; pp 33.5.1-33.5.4.
100. Schmidt, H.; Giustiniano, F.; Eda, G., Electronic transport properties of transition metal dichalcogenide field-effect devices: surface and interface effects. *Chemical Society Reviews* **2015**, *44* (21), 7715-7736.
101. International Roadmap for Devices and Systems (IRDS, 2017); <https://irds.ieee.org/>.
102. Luisier, M.; Lundstrom, M.; Antoniadis, D. A.; Bokor, J. In *Ultimate device scaling: Intrinsic performance comparisons of carbon-based, InGaAs, and Si field-effect transistors for 5 nm gate length*, 2011 International Electron Devices Meeting, 5-7 Dec. 2011; 2011; pp 11.2.1-11.2.4.
103. Sylvia, S. S.; Park, H.; Khayer, M. A.; Alam, K.; Klimeck, G.; Lake, R. K., Material Selection for Minimizing Direct Tunneling in Nanowire Transistors. *IEEE Transactions on Electron Devices* **2012**, *59* (8), 2064-2069.
104. Castellanos-Gomez, A.; Roldán, R.; Cappelluti, E.; Buscema, M.; Guinea, F.; van der Zant, H. S. J.; Steele, G. A., Local Strain Engineering in Atomically Thin MoS₂. *Nano Letters* **2013**, *13* (11), 5361-5366.
105. Lu, N.; Guo, H.; Li, L.; Dai, J.; Wang, L.; Mei, W.-N.; Wu, X.; Zeng, X. C., MoS₂/MX₂ heterobilayers: bandgap engineering via tensile strain or external electrical field. *Nanoscale* **2014**, *6* (5), 2879-2886.
106. O'Regan, T. P.; Hurley, P. K., Calculation of the capacitance-voltage characteristic of GaAs, In_{0.53}Ga_{0.47}As, and InAs metal-oxide-semiconductor structures. *Applied Physics Letters* **2011**, *99* (16), 163502.
107. Wang, K.-C.; Stanev, T. K.; Valencia, D.; Charles, J.; Henning, A.; Sangwan, V. K.; Lahiri, A.; Mejia, D.; Sarangapani, P.; Povolotskyi, M.; Afzalian, A.; Maassen, J.; Klimeck, G.; Hersam, M. C.; Lauhon, L. J.; Stern, N. P.; Kubis, T., Control of interlayer physics in 2H transition metal dichalcogenides. *Journal of Applied Physics* **2017**, *122* (22), 224302.
108. Furchi, M. M.; Polyushkin, D. K.; Pospischil, A.; Mueller, T., Mechanisms of Photoconductivity in Atomically Thin MoS₂. *Nano Letters* **2014**, *14* (11), 6165-6170.
109. ITRS 2.0, <http://www.itrs2.net/>.

-
110. Addou, R.; Colombo, L.; Wallace, R. M., Surface Defects on Natural MoS₂. *ACS Applied Materials & Interfaces* **2015**, *7* (22), 11921-11929.
111. Hosseini, M.; Elahi, M.; Pourfath, M.; Esseni, D., Strain induced mobility modulation in single-layer MoS₂. *Journal of Physics D: Applied Physics* **2015**, *48* (37), 375104.
112. Hauber, A.; Fahy, S., Scattering of carriers by coupled plasmon-phonon modes in bulk polar semiconductors and polar semiconductor heterostructures. *Physical Review B* **2017**, *95* (4), 045210.
113. Hong, J.; Hu, Z.; Probert, M.; Li, K.; Lv, D.; Yang, X.; Gu, L.; Mao, N.; Feng, Q.; Xie, L.; Zhang, J.; Wu, D.; Zhang, Z.; Jin, C.; Ji, W.; Zhang, X.; Yuan, J.; Zhang, Z., Exploring atomic defects in molybdenum disulphide monolayers. *Nature Communications* **2015**, *6*, 6293.
114. Qiu, H.; Xu, T.; Wang, Z.; Ren, W.; Nan, H.; Ni, Z.; Chen, Q.; Yuan, S.; Miao, F.; Song, F.; Long, G.; Shi, Y.; Sun, L.; Wang, J.; Wang, X., Hopping transport through defect-induced localized states in molybdenum disulphide. *Nature Communications* **2013**, *4*, 2642.
115. Zhou, W.; Zou, X.; Najmaei, S.; Liu, Z.; Shi, Y.; Kong, J.; Lou, J.; Ajayan, P. M.; Yakobson, B. I.; Idrobo, J.-C., Intrinsic Structural Defects in Monolayer Molybdenum Disulfide. *Nano Letters* **2013**, *13* (6), 2615-2622.
116. Noh, J.-Y.; Kim, H.; Kim, Y.-S., Stability and electronic structures of native defects in single-layer MoS₂. *Physical Review B* **2014**, *89* (20), 205417.
117. Liu, D.; Guo, Y.; Fang, L.; Robertson, J., Sulfur vacancies in monolayer MoS₂ and its electrical contacts. *Applied Physics Letters* **2013**, *103* (18), 183113.
118. Nan, F.; Nagashio, K.; Toriumi, A., Subthreshold transport in mono- and multilayered MoS₂ FETs. *Applied Physics Express* **2015**, *8* (6), 065203.
119. Fang, N.; Nagashio, K.; Toriumi, A., Experimental detection of active defects in few layers MoS₂ through random telegraphic signals analysis observed in its FET characteristics. *2D Materials* **2016**, *4* (1), 015035.
120. Allain, A.; Kang, J.; Banerjee, K.; Kis, A., Electrical contacts to two-dimensional semiconductors. *Nature Materials* **2015**, *14*, 1195.
121. Na, J.; Shin, M.; Joo, M.-K.; Huh, J.; Jeong Kim, Y.; Jong Choi, H.; Hyung Shim, J.; Kim, G.-T., Separation of interlayer resistance in multilayer MoS₂ field-effect transistors. *Applied Physics Letters* **2014**, *104* (23), 233502.
122. Kwon, H.-J.; Jang, J.; Kim, S.; Subramanian, V.; Grigoropoulos, C. P., Electrical characteristics of multilayer MoS₂ transistors at real operating temperatures with different ambient conditions. *Applied Physics Letters* **2014**, *105* (15), 152105.
123. Chang, H.-Y.; Zhu, W.; Akinwande, D., On the mobility and contact resistance evaluation for transistors based on MoS₂ or two-dimensional semiconducting atomic crystals. *Applied Physics Letters* **2014**, *104* (11), 113504.
124. Liu, W.; Sarkar, D.; Kang, J.; Cao, W.; Banerjee, K., Impact of Contact on the Operation and Performance of Back-Gated Monolayer MoS₂ Field-Effect-Transistors. *ACS Nano* **2015**, *9* (8), 7904-7912.
125. Bhattacharjee, S.; Ganapathi, K. L.; Nath, D. N.; Bhat, N., Surface State Engineering of Metal/MoS₂ Contacts Using Sulfur Treatment for Reduced Contact Resistance and Variability. *IEEE Transactions on Electron Devices* **2016**, *63* (6), 2556-2562.

-
126. Kwon, J.; Lee, J.-Y.; Yu, Y.-J.; Lee, C.-H.; Cui, X.; Hone, J.; Lee, G.-H., Thickness-dependent Schottky barrier height of MoS₂ field-effect transistors. *Nanoscale* **2017**, *9* (18), 6151-6157.
127. Guo, Y.; Han, Y.; Li, J.; Xiang, A.; Wei, X.; Gao, S.; Chen, Q., Study on the Resistance Distribution at the Contact between Molybdenum Disulfide and Metals. *ACS Nano* **2014**, *8* (8), 7771-7779.
128. Kang, J.; Liu, W.; Banerjee, K., High-performance MoS₂ transistors with low-resistance molybdenum contacts. *Applied Physics Letters* **2014**, *104* (9), 093106.
129. Li, S.-L.; Komatsu, K.; Nakaharai, S.; Lin, Y.-F.; Yamamoto, M.; Duan, X.; Tsukagoshi, K., Thickness Scaling Effect on Interfacial Barrier and Electrical Contact to Two-Dimensional MoS₂ Layers. *ACS Nano* **2014**, *8* (12), 12836-12842.
130. Liu, W.; Kang, J.; Cao, W.; Sarkar, D.; Khatami, Y.; Jena, D.; Banerjee, K. In *High-performance few-layer-MoS₂ field-effect-transistor with record low contact-resistance*, 2013 IEEE International Electron Devices Meeting, 9-11 Dec. 2013; 2013; pp 19.4.1-19.4.4.
131. Liu, H.; Si, M.; Deng, Y.; Neal, A. T.; Du, Y.; Najmaei, S.; Ajayan, P. M.; Lou, J.; Ye, P. D., Switching Mechanism in Single-Layer Molybdenum Disulfide Transistors: An Insight into Current Flow across Schottky Barriers. *ACS Nano* **2014**, *8* (1), 1031-1038.
132. Tung, R. T., The physics and chemistry of the Schottky barrier height. *Applied Physics Reviews* **2014**, *1* (1), 011304.
133. Colinge, J. P.; Colinge, C. A., *Physics of Semiconductor Devices*. Springer: 2002.
134. Neudeck, G. W., *The PN junction diode*. Addison-Wesley Longman, Incorporated: 1983.
135. Das, S.; Chen, H.-Y.; Penumatcha, A. V.; Appenzeller, J., High Performance Multilayer MoS₂ Transistors with Scandium Contacts. *Nano Letters* **2013**, *13* (1), 100-105.
136. Robertson, J., Band offsets, Schottky barrier heights, and their effects on electronic devices. *Journal of Vacuum Science & Technology A* **2013**, *31* (5), 050821.
137. Heine, V., Theory of Surface States. *Physical Review* **1965**, *138* (6A), A1689-A1696.
138. Tejedor, C.; Flores, F.; Louis, E., The metal-semiconductor interface: Si (111) and zincblende (110) junctions. *Journal of Physics C: Solid State Physics* **1977**, *10* (12), 2163-2177.
139. Spicer, W. E.; Chye, P. W.; Skeath, P. R.; Su, C. Y.; Lindau, I., New and unified model for Schottky barrier and III-V insulator interface states formation. *Journal of Vacuum Science and Technology* **1979**, *16* (5), 1422-1433.
140. Mead, C. A.; Spitzer, W. G., Fermi Level Position at Metal-Semiconductor Interfaces. *Physical Review* **1964**, *134* (3A), A713-A716.
141. Duke, C. B.; Mailhot, C., A microscopic model of metal-semiconductor contacts. *Journal of Vacuum Science & Technology B: Microelectronics Processing and Phenomena* **1985**, *3* (4), 1170-1177.
142. Kim, C.; Moon, I.; Lee, D.; Choi, M. S.; Ahmed, F.; Nam, S.; Cho, Y.; Shin, H.-J.; Park, S.; Yoo, W. J., Fermi Level Pinning at Electrical Metal Contacts of Monolayer Molybdenum Dichalcogenides. *ACS Nano* **2017**, *11* (2), 1588-1596.
143. McDonnell, S.; Addou, R.; Buie, C.; Wallace, R. M.; Hinkle, C. L., Defect-Dominated Doping and Contact Resistance in MoS₂. *ACS Nano* **2014**, *8* (3), 2880-2888.
144. Neal, A. T.; Liu, H.; Gu, J. J.; Ye, P. D. In *Metal contacts to MoS₂: A two-dimensional semiconductor*, 70th Device Research Conference, 18-20 June 2012; 2012; pp 65-66.

-
145. Liu, H.; Neal, A. T.; Ye, P. D., Channel Length Scaling of MoS₂ MOSFETs. *ACS Nano* **2012**, *6* (10), 8563-8569.
146. Synopsys Inc., CA, USA, Sentaurus Device User Guide (2015).
147. Landauer, R., Spatial Variation of Currents and Fields Due to Localized Scatterers in Metallic Conduction. *IBM Journal of Research and Development* **1957**, *1* (3), 223-231.
148. Keldysh, L. V., Diagram technique for nonequilibrium processes. *Sov. Phys. JETP* **1965**, *20* (4), 1018-1026.
149. Datta, S., Nanoscale device modeling: the Green's function method. *Superlattices and Microstructures* **2000**, *28* (4), 253-278.
150. Stieger, C.; Szabo, A.; Bunjaku, T.; Luisier, M., Ab-initio quantum transport simulation of self-heating in single-layer 2-D materials. *Journal of Applied Physics* **2017**, *122* (4), 045708.
151. Yoon, Y.; Ganapathi, K.; Salahuddin, S., How Good Can Monolayer MoS₂ Transistors Be? *Nano Letters* **2011**, *11* (9), 3768-3773.
152. Gong, K.; Zhang, L.; Liu, D.; Liu, L.; Zhu, Y.; Zhao, Y.; Guo, H., Electric control of spin in monolayer WSe₂ field effect transistors. *Nanotechnology* **2014**, *25* (43), 435201.
153. Lu, H.; Seabaugh, A., Tunnel Field-Effect Transistors: State-of-the-Art. *IEEE Journal of the Electron Devices Society* **2014**, *2* (4), 44-49.
154. Marin, E. G.; Perucchini, M.; Marian, D.; Iannaccone, G.; Fiori, G., Modeling of Electron Devices Based on 2-D Materials. *IEEE Transactions on Electron Devices* **2018**, *65* (10), 4167-4179.
155. Esseni, D.; Palestri, P.; Selmi, L., *Nanoscale MOS Transistors: Semi-Classical Transport and Applications*. Cambridge University Press: Cambridge, 2011.
156. Ferry, D. K., Electron transport in some transition metal di-chalcogenides: MoS₂ and WS₂. *Semiconductor Science and Technology* **2017**, *32* (8), 085003.
157. Gaddemane, G.; Vandenberghe, W. G.; Fischetti, M. V. In *Theoretical study of electron transport in silicene and germanene using full-band Monte Carlo simulations*, 2016 International Conference on Simulation of Semiconductor Processes and Devices (SISPAD), 6-8 Sept. 2016; 2016; pp 353-356.
158. Vasileska, D.; Goodnick, S. M., *Computational Electronics*. Morgan & Claypool Publishers: 2006.
159. Hänsch, W., *The Drift Diffusion Equation and Its Applications in MOSFET Modeling*. Springer Vienna: 1991.
160. Moroz, V.; Lee, S.; Joanne, H.; Munkang, C.; Ma, T.; Jie, L.; Yunqiang, Z.; Xi-Wei, L.; Kawa, J.; Saad, Y. In *Modeling and optimization of group IV and III-V FinFETs and nano-wires*, 2014 IEEE International Electron Devices Meeting, 15-17 Dec. 2014; 2014; pp 7.4.1-7.4.4.
161. Weckx, P.; Ryckaert, J.; Litta, E. D.; Yakimets, D.; Matagne, P.; Schuddinck, P.; Jang, D.; Chehab, B.; Baert, R.; Gupta, M.; Oniki, Y.; Ragnarsson, L.; Horiguchi, N.; Spessot, A.; Verkest, D. In *Novel forksheet device architecture as ultimate logic scaling device towards 2nm*, 2019 IEEE International Electron Devices Meeting (IEDM), 7-11 Dec. 2019; 2019; pp 36.5.1-36.5.4.
162. Ryckaert, J.; Schuddinck, P.; Weckx, P.; Bouche, G.; Vincent, B.; Smith, J.; Sherazi, Y.; Mallik, A.; Mertens, H.; Demuyne, S.; Bao, T. H.; Veloso, A.; Horiguchi, N.; Mocuta, A.; Mocuta, D.; Boemmels, J. In *The Complementary FET (CFET) for CMOS*

scaling beyond N3, 2018 IEEE Symposium on VLSI Technology, 18-22 June 2018; 2018; pp 141-142.

163. Lundstrom, M. S.; Schuelke, R. J., Modeling semiconductor heterojunctions in equilibrium. *Solid-State Electronics* **1982**, *25* (8), 683-691.

164. Lundstrom, M. S.; Schuelke, R. J., Numerical analysis of heterostructure semiconductor devices. *IEEE Transactions on Electron Devices* **1983**, *30* (9), 1151-1159.

165. Feng, P.; Song, S.; Nallapati, G.; Zhu, J.; Bao, J.; Moroz, V.; Choi, M.; Lin, X.; Lu, Q.; Colombeau, B.; Breil, N.; Chudzik, M.; Chidambaram, C., Comparative Analysis of Semiconductor Device Architectures for 5-nm Node and Beyond. *IEEE Electron Device Letters* **2017**, *38* (12), 1657-1660.

166. Ma, T.; Moroz, V.; Borges, R.; Smith, L. In *TCAD: Present state and future challenges*, 2010 International Electron Devices Meeting, 6-8 Dec. 2010; 2010; pp 15.3.1-15.3.4.

167. Knobloch, T.; Rzepa, G.; Illarionov, Y. Y.; Wabl, M.; Schanovsky, F.; Jech, M.; Stampfer, B.; Furchi, M. M.; Müller, T.; Grassler, T. In *Physical modeling of the hysteresis in MOS2 transistors*, 2017 47th European Solid-State Device Research Conference (ESSDERC), 11-14 Sept. 2017; 2017; pp 284-287.

168. Arutchelvan, G.; Lockhart de la Rosa, C. J.; Matagne, P.; Sutar, S.; Radu, I.; Huyghebaert, C.; De Gendt, S.; Heyns, M., From the metal to the channel: a study of carrier injection through the metal/2D MoS₂ interface. *Nanoscale* **2017**, *9* (30), 10869-10879.

169. Kim, J.; Yong, K., Photoelectron spectroscopic analysis of Hf-silicate/SiO₂ / Si stacks deposited by atomic layer chemical vapor deposition. *Journal of Vacuum Science & Technology B: Microelectronics and Nanometer Structures Processing, Measurement, and Phenomena* **2006**, *24* (3), 1147-1150.

170. Briggs, D., Handbook of X-ray Photoelectron Spectroscopy C. D. Wanger, W. M. Riggs, L. E. Davis, J. F. Moulder and G. E. Muilenberg Perkin-Elmer Corp., Physical Electronics Division, Eden Prairie, Minnesota, USA, 1979. 190 pp. \$195. *Surface and Interface Analysis* **1981**, *3* (4), v-v.

171. Liu, Y.; Si, L.; Zhou, X.; Liu, X.; Xu, Y.; Bao, J.; Dai, Z., A selenium-confined microporous carbon cathode for ultrastable lithium–selenium batteries. *Journal of Materials Chemistry A* **2014**, *2* (42), 17735-17739.

172. Zhu, J.; Li, Y. R.; Liu, Z. G., Fabrication and characterization of pulsed laser deposited HfO₂ films for high-k gate dielectric applications. *Journal of Physics D: Applied Physics* **2004**, *37* (20), 2896-2900.

173. Kang, M.; Rathi, S.; Lee, I.; Lim, D.; Wang, J.; Li, L.; Khan, M. A.; Kim, G.-H., Electrical characterization of multilayer HfSe₂ field-effect transistors on SiO₂ substrate. *Applied Physics Letters* **2015**, *106* (14), 143108.

174. Gao, J.; Li, B.; Tan, J.; Chow, P.; Lu, T.-M.; Koratkar, N., Aging of Transition Metal Dichalcogenide Monolayers. *ACS Nano* **2016**, *10* (2), 2628-2635.

175. He, Z.; Wang, X.; Xu, W.; Zhou, Y.; Sheng, Y.; Rong, Y.; Smith, J. M.; Warner, J. H., Revealing Defect-State Photoluminescence in Monolayer WS₂ by Cryogenic Laser Processing. *ACS Nano* **2016**, *10* (6), 5847-5855.

176. Budania, P.; Baine, P.; Montgomery, J.; McGeough, C.; Cafolla, T.; Modreanu, M.; McNeill, D.; Mitchell, N.; Hughes, G.; Hurley, P., Long-term stability of mechanically exfoliated MoS₂ flakes. *MRS Communications* **2017**, *7* (4), 813-818.

-
177. Wood, J. D.; Wells, S. A.; Jariwala, D.; Chen, K.-S.; Cho, E.; Sangwan, V. K.; Liu, X.; Lauhon, L. J.; Marks, T. J.; Hersam, M. C., Effective Passivation of Exfoliated Black Phosphorus Transistors against Ambient Degradation. *Nano Letters* **2014**, *14* (12), 6964-6970.
178. Castellanos-Gomez, A.; Vicarelli, L.; Prada, E.; Island, J. O.; Narasimha-Acharya, K. L.; Blanter, S. I.; Groenendijk, D. J.; Buscema, M.; Steele, G. A.; Alvarez, J. V.; Zandbergen, H. W.; Palacios, J. J.; van der Zant, H. S. J., Isolation and characterization of few-layer black phosphorus. *2D Materials* **2014**, *1* (2), 025001.
179. Koenig, S. P.; Doganov, R. A.; Schmidt, H.; Castro Neto, A. H.; Özyilmaz, B., Electric field effect in ultrathin black phosphorus. *Applied Physics Letters* **2014**, *104* (10), 103106.
180. Kim, J.-S.; Liu, Y.; Zhu, W.; Kim, S.; Wu, D.; Tao, L.; Dodabalapur, A.; Lai, K.; Akinwande, D., Toward air-stable multilayer phosphorene thin-films and transistors. *Scientific Reports* **2015**, *5*, 8989.
181. Liu, H.; Han, N.; Zhao, J., Atomistic insight into the oxidation of monolayer transition metal dichalcogenides: from structures to electronic properties. *RSC Advances* **2015**, *5* (23), 17572-17581.
182. Kc, S.; Longo, R. C.; Wallace, R. M.; Cho, K., Surface oxidation energetics and kinetics on MoS₂ monolayer. *Journal of Applied Physics* **2015**, *117* (13), 135301.
183. Li, Q.; Zhou, Q.; Shi, L.; Chen, Q.; Wang, J., Recent advances in oxidation and degradation mechanisms of ultrathin 2D materials under ambient conditions and their passivation strategies. *Journal of Materials Chemistry A* **2019**, *7* (9), 4291-4312.
184. Martincová, J.; Otyepka, M.; Lazar, P., Is Single Layer MoS₂ Stable in the Air? *Chemistry – A European Journal* **2017**, *23* (53), 13233-13239.
185. Longo, R. C.; Addou, R.; Kc, S.; Noh, J.-Y.; Smyth, C. M.; Barrera, D.; Zhang, C.; Hsu, J. W. P.; Wallace, R. M.; Cho, K., Intrinsic air stability mechanisms of two-dimensional transition metal dichalcogenide surfaces: basal versus edge oxidation. *2D Materials* **2017**, *4* (2), 025050.
186. Li, Y.; Zhou, Z.; Zhang, S.; Chen, Z., MoS₂ Nanoribbons: High Stability and Unusual Electronic and Magnetic Properties. *Journal of the American Chemical Society* **2008**, *130* (49), 16739-16744.
187. Lee, G.-H.; Cui, X.; Kim, Y. D.; Arefe, G.; Zhang, X.; Lee, C.-H.; Ye, F.; Watanabe, K.; Taniguchi, T.; Kim, P.; Hone, J., Highly Stable, Dual-Gated MoS₂ Transistors Encapsulated by Hexagonal Boron Nitride with Gate-Controllable Contact, Resistance, and Threshold Voltage. *ACS Nano* **2015**, *9* (7), 7019-7026.
188. Long, B.; Manning, M.; Burke, M.; Szafraneck, B. N.; Visimberga, G.; Thompson, D.; Greer, J. C.; Povey, I. M.; MacHale, J.; Lejosne, G.; Neumaier, D.; Quinn, A. J., Non-Covalent Functionalization of Graphene Using Self-Assembly of Alkane-Amines. *Advanced Functional Materials* **2012**, *22* (4), 717-725.
189. O'Connell, J.; Collins, G.; McGlacken, G. P.; Duffy, R.; Holmes, J. D., Monolayer Doping of Si with Improved Oxidation Resistance. *ACS Applied Materials & Interfaces* **2016**, *8* (6), 4101-4108.
190. Mleczko, M. J.; Zhang, C.; Lee, H. R.; Kuo, H.-H.; Magyari-Köpe, B.; Moore, R. G.; Shen, Z.-X.; Fisher, I. R.; Nishi, Y.; Pop, E., HfSe₂ and ZrSe₂: Two-dimensional semiconductors with native high- κ oxides. *Science Advances* **2017**, *3* (8), e1700481.
191. Chae, S. H.; Jin, Y.; Kim, T. S.; Chung, D. S.; Na, H.; Nam, H.; Kim, H.; Perello, D. J.; Jeong, H. Y.; Ly, T. H.; Lee, Y. H., Oxidation Effect in Octahedral Hafnium Disulfide Thin Film. *ACS Nano* **2016**, *10* (1), 1309-1316.

-
192. Addou, R.; Wallace, R. M., Surface Analysis of WSe₂ Crystals: Spatial and Electronic Variability. *ACS Applied Materials & Interfaces* **2016**, *8* (39), 26400-26406.
193. Li, H.; Wu, J.; Huang, X.; Lu, G.; Yang, J.; Lu, X.; Xiong, Q.; Zhang, H., Rapid and Reliable Thickness Identification of Two-Dimensional Nanosheets Using Optical Microscopy. *ACS Nano* **2013**, *7* (11), 10344-10353.
194. McDonnell, S. J.; Wallace, R. M., Atomically-thin layered films for device applications based upon 2D TMDC materials. *Thin Solid Films* **2016**, *616*, 482-501.
195. Mirabelli, G.; McGeough, C.; Schmidt, M.; McCarthy, E. K.; Monaghan, S.; Povey, I. M.; McCarthy, M.; Gity, F.; Nagle, R.; Hughes, G.; Cafolla, A.; Hurley, P. K.; Duffy, R., Air sensitivity of MoS₂, MoSe₂, MoTe₂, HfS₂, and HfSe₂. *Journal of Applied Physics* **2016**, *120* (12), 125102.
196. Mori, T.; Ninomiya, N.; Kubo, T.; Uchida, N.; Watanabe, E.; Tsuya, D.; Moriyama, S.; Tanaka, M.; Ando, A., Characterization of Effective Mobility and Its Degradation Mechanism in MoS₂ MOSFETs. *IEEE Transactions on Nanotechnology* **2016**, *15* (4), 651-656.
197. Monaghan, S.; Gity, F.; Duffy, R.; Mirabelli, G.; McCarthy, M.; Cherkaoui, K.; Povey, I. M.; Nagle, R. E.; Hurley, P. K.; Lindemuth, J. R.; Napolitani, E. In *Hall-effect mobility for a selection of natural and synthetic 2D semiconductor crystals*, 2017 Joint International EUROSIOI Workshop and International Conference on Ultimate Integration on Silicon (EUROSIOI-ULIS), 3-5 April 2017; 2017; pp 27-30.
198. Mirabelli, G.; Schmidt, M.; Sheehan, B.; Cherkaoui, K.; Monaghan, S.; Povey, I.; McCarthy, M.; Bell, A. P.; Nagle, R.; Crupi, F.; Hurley, P. K.; Duffy, R., Back-gated Nb-doped MoS₂ junctionless field-effect-transistors. *AIP Advances* **2016**, *6* (2), 025323.
199. Colinge, J. P.; Kranti, A.; Yan, R.; Lee, C. W.; Ferain, I.; Yu, R.; Dehdashti Akhavan, N.; Razavi, P., Junctionless Nanowire Transistor (JNT): Properties and design guidelines. *Solid-State Electronics* **2011**, *65-66*, 33-37.
200. Cao, W.; Kang, J.; Liu, W.; Banerjee, K., A Compact Current–Voltage Model for 2D Semiconductor Based Field-Effect Transistors Considering Interface Traps, Mobility Degradation, and Inefficient Doping Effect. *IEEE Transactions on Electron Devices* **2014**, *61* (12), 4282-4290.
201. Chen, K.; Hu, C.; Fang, P.; Lin, M. R.; Wollesen, D. L., Predicting CMOS speed with gate oxide and voltage scaling and interconnect loading effects. *IEEE Transactions on Electron Devices* **1997**, *44* (11), 1951-1957.
202. Zhu, W. J.; Ma, T. P., Temperature dependence of channel mobility in HfO₂-gated NMOSFETs. *IEEE Electron Device Letters* **2004**, *25* (2), 89-91.
203. Bhattacharjee, S.; Ganapathi, K. L.; Chandrasekar, H.; Paul, T.; Mohan, S.; Ghosh, A.; Raghavan, S.; Bhat, N., Nitride Dielectric Environments to Suppress Surface Optical Phonon Dominated Scattering in High-Performance Multilayer MoS₂ FETs. *Advanced Electronic Materials* **2017**, *3* (1), 1600358.
204. Fuhrer, M. S.; Hone, J., Measurement of mobility in dual-gated MoS₂ transistors. *Nature Nanotechnology* **2013**, *8*, 146.
205. Ong, Z.-Y.; Fischetti, M. V., Mobility enhancement and temperature dependence in top-gated single-layer MoS₂. *Physical Review B* **2013**, *88* (16), 165316.
206. Takagi, S.; Toriumi, A.; Iwase, M.; Tango, H., On the universality of inversion layer mobility in Si MOSFET's: Part I-effects of substrate impurity concentration. *IEEE Transactions on Electron Devices* **1994**, *41* (12), 2357-2362.

-
207. Suryavanshi, S. V.; Pop, E., S2DS: Physics-based compact model for circuit simulation of two-dimensional semiconductor devices including non-idealities. *Journal of Applied Physics* **2016**, *120* (22), 224503.
208. Kim, S.; Konar, A.; Hwang, W.-S.; Lee, J. H.; Lee, J.; Yang, J.; Jung, C.; Kim, H.; Yoo, J.-B.; Choi, J.-Y.; Jin, Y. W.; Lee, S. Y.; Jena, D.; Choi, W.; Kim, K., High-mobility and low-power thin-film transistors based on multilayer MoS₂ crystals. *Nature Communications* **2012**, *3*, 1011.
209. Mirabelli, G.; Duffy, R.; Hurley, P. K.; Monaghan, S.; Cherkaoui, K.; Schmidt, M.; Sheehan, B.; Povey, I. M.; McCarthy, M.; Nagle, R.; Bell, A., Mo-Based Transition-Metal-Dichalcogenide Junctionless Field-Effect-Transistors. *Meeting Abstracts* **2016**, *MA2016-01* (26), 1289-1289.
210. Das, S.; Demarteau, M.; Roelofs, A., Nb-doped single crystalline MoS₂ field effect transistor. *Applied Physics Letters* **2015**, *106* (17), 173506.
211. Leong, W. S.; Luo, X.; Li, Y.; Khoo, K. H.; Quek, S. Y.; Thong, J. T. L., Low Resistance Metal Contacts to MoS₂ Devices with Nickel-Etched-Graphene Electrodes. *ACS Nano* **2015**, *9* (1), 869-877.
212. Cui, X.; Shih, E.-M.; Jauregui, L. A.; Chae, S. H.; Kim, Y. D.; Li, B.; Seo, D.; Pistunova, K.; Yin, J.; Park, J.-H.; Choi, H.-J.; Lee, Y. H.; Watanabe, K.; Taniguchi, T.; Kim, P.; Dean, C. R.; Hone, J. C., Low-Temperature Ohmic Contact to Monolayer MoS₂ by van der Waals Bonded Co/h-BN Electrodes. *Nano Letters* **2017**, *17* (8), 4781-4786.
213. Kappera, R.; Voiry, D.; Yalcin, S. E.; Branch, B.; Gupta, G.; Mohite, A. D.; Chhowalla, M., Phase-engineered low-resistance contacts for ultrathin MoS₂ transistors. *Nature Materials* **2014**, *13*, 1128.
214. Leong, W. S.; Ji, Q.; Mao, N.; Han, Y.; Wang, H.; Goodman, A. J.; Vignon, A.; Su, C.; Guo, Y.; Shen, P.-C.; Gao, Z.; Muller, D. A.; Tisdale, W. A.; Kong, J., Synthetic Lateral Metal-Semiconductor Heterostructures of Transition Metal Disulfides. *Journal of the American Chemical Society* **2018**, *140* (39), 12354-12358.
215. Valsaraj, A.; Chang, J.; Rai, A.; Register, L. F.; Banerjee, S. K., Theoretical and experimental investigation of vacancy-based doping of monolayer MoS₂ on oxide. *2D Materials* **2015**, *2* (4), 045009.
216. Rai, A.; Valsaraj, A.; Movva, H. C. P.; Roy, A.; Tutuc, E.; Register, L. F.; Banerjee, S. K. In *Interfacial-oxygen-vacancy mediated doping of MoS₂ by high-k dielectrics*, 2015 73rd Annual Device Research Conference (DRC), 21-24 June 2015; 2015; pp 189-190.
217. McClellan, C. J.; Yalon, E.; Smithe, K. K. H.; Suryavanshi, S. V.; Pop, E. In *Effective n-type doping of monolayer MoS₂ by AlOx*, 2017 75th Annual Device Research Conference (DRC), 25-28 June 2017; 2017; pp 1-2.
218. Alharbi, A.; Shahrjerdi, D., Analyzing the Effect of High-k Dielectric-Mediated Doping on Contact Resistance in Top-Gated Monolayer MoS₂ Transistors. *IEEE Transactions on Electron Devices* **2018**, *65* (10), 4084-4092.
219. Liu, X.; Qu, D.; Ryu, J.; Ahmed, F.; Yang, Z.; Lee, D.; Yoo, W. J., P-Type Polar Transition of Chemically Doped Multilayer MoS₂ Transistor. *Advanced Materials* **2016**, *28* (12), 2345-2351.
220. Kiriya, D.; Tosun, M.; Zhao, P.; Kang, J. S.; Javey, A., Air-Stable Surface Charge Transfer Doping of MoS₂ by Benzyl Viologen. *Journal of the American Chemical Society* **2014**, *136* (22), 7853-7856.
221. Du, Y.; Liu, H.; Neal, A. T.; Si, M.; Ye, P. D., Molecular Doping of Multilayer MoS₂ Field-Effect Transistors: Reduction in Sheet and Contact Resistances. *IEEE Electron Device Letters* **2013**, *34* (10), 1328-1330.

-
222. Yang, L.; Majumdar, K.; Liu, H.; Du, Y.; Wu, H.; Hatzistergos, M.; Hung, P. Y.; Tieckelmann, R.; Tsai, W.; Hobbs, C.; Ye, P. D., Chloride Molecular Doping Technique on 2D Materials: WS₂ and MoS₂. *Nano Letters* **2014**, *14* (11), 6275-6280.
223. English, C. D.; Shine, G.; Dorgan, V. E.; Saraswat, K. C.; Pop, E., Improved Contacts to MoS₂ Transistors by Ultra-High Vacuum Metal Deposition. *Nano Letters* **2016**, *16* (6), 3824-3830.
224. Wang, Y.; Kim, J. C.; Wu, R. J.; Martinez, J.; Song, X.; Yang, J.; Zhao, F.; Mkhoyan, A.; Jeong, H. Y.; Chhowalla, M., Van der Waals contacts between three-dimensional metals and two-dimensional semiconductors. *Nature* **2019**, *568* (7750), 70-74.
225. Bolshakov, P.; Smyth, C. M.; Khosravi, A.; Zhao, P.; Hurley, P. K.; Hinkle, C. L.; Wallace, R. M.; Young, C. D., Contact Engineering for Dual-Gate MoS₂ Transistors Using O₂ Plasma Exposure. *ACS Applied Electronic Materials* **2019**, *1* (2), 210-219.
226. Baugher, B. W. H.; Churchill, H. O. H.; Yang, Y.; Jarillo-Herrero, P., Intrinsic Electronic Transport Properties of High-Quality Monolayer and Bilayer MoS₂. *Nano Letters* **2013**, *13* (9), 4212-4216.
227. Yang, H.; Li, C.; Yue, L.; Wen, C.; Zhang, J.; Wu, D., Improving Electrical Performance of Few-Layer MoS₂ FETs via Microwave Annealing. *IEEE Electron Device Letters* **2019**, *40* (7), 1116-1119.
228. Kwon, H.-J.; Kim, S.; Jang, J.; Grigoropoulos, C. P., Evaluation of pulsed laser annealing for flexible multilayer MoS₂ transistors. *Applied Physics Letters* **2015**, *106* (11), 113111.
229. Abraham, M.; Mohny, S. E., Annealed Ag contacts to MoS₂ field-effect transistors. *Journal of Applied Physics* **2017**, *122* (11), 115306.
230. Souder, A.; Brodie, D. E., Electrical Contacts and Conductivity of MoS₂ Layer Structures. *Canadian Journal of Physics* **1971**, *49* (20), 2565-2571.
231. Souder, A. D.; Brodie, D. E., The Effect of Contact Annealing on Hall Data for MoS₂ Layer Structures. *Canadian Journal of Physics* **1972**, *50* (11), 1223-1225.
232. Roh, J.; Lee, J.-H.; Jin, S. H.; Lee, C., Negligible hysteresis of molybdenum disulfide field-effect transistors through thermal annealing. *Journal of Information Display* **2016**, *17* (3), 103-108.
233. Bolshakov, P.; Zhao, P.; Azcatl, A.; Hurley, P. K.; Wallace, R. M.; Young, C. D., Electrical characterization of top-gated molybdenum disulfide field-effect-transistors with high-k dielectrics. *Microelectronic Engineering* **2017**, *178*, 190-193.
234. Cristiano, F.; Shayesteh, M.; Duffy, R.; Huet, K.; Mazzamuto, F.; Qiu, Y.; Quillec, M.; Henrichsen, H. H.; Nielsen, P. F.; Petersen, D. H.; La Magna, A.; Caruso, G.; Boninelli, S., Defect evolution and dopant activation in laser annealed Si and Ge. *Materials Science in Semiconductor Processing* **2016**, *42*, 188-195.
235. Hurley, P. K.; É, O. C.; Djara, V.; Monaghan, S.; Povey, I. M.; Long, R. D.; Sheehan, B.; Lin, J.; McIntyre, P. C.; Brennan, B.; Wallace, R. M.; Pemble, M. E.; Cherkaoui, K., The Characterization and Passivation of Fixed Oxide Charges and Interface States in the Al₂O₃/InGaAs MOS System. *IEEE Transactions on Device and Materials Reliability* **2013**, *13* (4), 429-443.
236. Qiu, H.; Pan, L.; Yao, Z.; Li, J.; Shi, Y.; Wang, X., Electrical characterization of back-gated bi-layer MoS₂ field-effect transistors and the effect of ambient on their performances. *Applied Physics Letters* **2012**, *100* (12), 123104.
237. Kim, J. H.; Lee, J.; Kim, J. H.; Hwang, C. C.; Lee, C.; Park, J. Y., Work function variation of MoS₂ atomic layers grown with chemical vapor deposition: The effects of

thickness and the adsorption of water/oxygen molecules. *Applied Physics Letters* **2015**, *106* (25), 251606.

238. Lu, Q.; Fang, C.; Liu, Y.; Shao, Y.; Han, G.; Zhang, J.; Hao, Y., Temperature dependence of annealing on the contact resistance of MoS₂ with graphene electrodes observed. *Japanese Journal of Applied Physics* **2018**, *57* (4S), 04FP07.

239. Ciarrocchi, A.; Avsar, A.; Ovchinnikov, D.; Kis, A., Thickness-modulated metal-to-semiconductor transformation in a transition metal dichalcogenide. *Nature Communications* **2018**, *9* (1), 919.

240. Wang, Y.; Li, L.; Yao, W.; Song, S.; Sun, J. T.; Pan, J.; Ren, X.; Li, C.; Okunishi, E.; Wang, Y.-Q.; Wang, E.; Shao, Y.; Zhang, Y. Y.; Yang, H.-t.; Schwier, E. F.; Iwasawa, H.; Shimada, K.; Taniguchi, M.; Cheng, Z.; Zhou, S.; Du, S.; Pennycook, S. J.; Pantelides, S. T.; Gao, H.-J., Monolayer PtSe₂, a New Semiconducting Transition-Metal-Dichalcogenide, Epitaxially Grown by Direct Selenization of Pt. *Nano Letters* **2015**, *15* (6), 4013-4018.

241. Yim, C.; Passi, V.; Lemme, M. C.; Duesberg, G. S.; Ó Coileáin, C.; Pallecchi, E.; Fadil, D.; McEvoy, N., Electrical devices from top-down structured platinum diselenide films. *npj 2D Materials and Applications* **2018**, *2* (1), 5.

242. Yim, C.; McEvoy, N.; Riazimehr, S.; Schneider, D. S.; Gity, F.; Monaghan, S.; Hurley, P. K.; Lemme, M. C.; Duesberg, G. S., Wide Spectral Photoresponse of Layered Platinum Diselenide-Based Photodiodes. *Nano Letters* **2018**, *18* (3), 1794-1800.

243. Wagner, S.; Yim, C.; McEvoy, N.; Kataria, S.; Yokaribas, V.; Kuc, A.; Pindl, S.; Fritzen, C.-P.; Heine, T.; Duesberg, G. S.; Lemme, M. C., Highly Sensitive Electromechanical Piezoresistive Pressure Sensors Based on Large-Area Layered PtSe₂ Films. *Nano Letters* **2018**, *18* (6), 3738-3745.

244. Walsh, L. A.; Addou, R.; Wallace, R. M.; Hinkle, C. L., Chapter 22 - Molecular Beam Epitaxy of Transition Metal Dichalcogenides. In *Molecular Beam Epitaxy (Second Edition)*, Henini, M., Ed. Elsevier: 2018; pp 515-531.

245. Herrera-Gomez, A. AAnalyzer, 2002.

246. Mirabelli, G.; Walsh, L. A.; Gity, F.; Bhattacharjee, S.; Cullen, C. P.; Ó Coileáin, C.; Monaghan, S.; McEvoy, N.; Nagle, R.; Hurley, P. K.; Duffy, R., Effects of Annealing Temperature and Ambient on Metal/PtSe₂ Contact Alloy Formation. *ACS Omega* **2019**, *4* (17), 17487-17493.

247. Klootwijk, J. H.; Timmering, C. E. In *Merits and limitations of circular TLM structures for contact resistance determination for novel III-V HBTs*, Proceedings of the 2004 International Conference on Microelectronic Test Structures (IEEE Cat. No.04CH37516), 22-25 March 2004; 2004; pp 247-252.

248. Kang, J.; Liu, W.; Sarkar, D.; Jena, D.; Banerjee, K., Computational Study of Metal Contacts to Monolayer Transition-Metal Dichalcogenide Semiconductors. *Physical Review X* **2014**, *4* (3), 031005.

249. McDonnell, S.; Smyth, C.; Hinkle, C. L.; Wallace, R. M., MoS₂-Titanium Contact Interface Reactions. *ACS Applied Materials & Interfaces* **2016**, *8* (12), 8289-8294.

250. Smyth, C. M.; Addou, R.; McDonnell, S.; Hinkle, C. L.; Wallace, R. M., Contact Metal-MoS₂ Interfacial Reactions and Potential Implications on MoS₂-Based Device Performance. *The Journal of Physical Chemistry C* **2016**, *120* (27), 14719-14729.

251. Smyth, C. M.; Addou, R.; McDonnell, S.; Hinkle, C. L.; Wallace, R. M., WSe₂-contact metal interface chemistry and band alignment under high vacuum and ultra high vacuum deposition conditions. *2D Materials* **2017**, *4* (2), 025084.

-
252. Smyth, C. M.; Walsh, L. A.; Bolshakov, P.; Catalano, M.; Addou, R.; Wang, L.; Kim, J.; Kim, M. J.; Young, C. D.; Hinkle, C. L.; Wallace, R. M., Engineering the Palladium–WSe₂ Interface Chemistry for Field Effect Transistors with High-Performance Hole Contacts. *ACS Applied Nano Materials* **2019**, *2* (1), 75-88.
253. Lince, J. R.; Carré, D. J.; Fleischauer, P. D., Schottky-barrier formation on a covalent semiconductor without Fermi-level pinning: The metal-MoS₂ (0001) interface. *Physical Review B* **1987**, *36* (3), 1647-1656.
254. Rosa, C. J. L. d. l.; Arutchelvan, G.; Leonhardt, A.; Huyghebaert, C.; Radu, I.; Heyns, M.; Gendt, S. D., Relation between film thickness and surface doping of MoS₂ based field effect transistors. *APL Materials* **2018**, *6* (5), 058301.
255. Mirabelli, G.; Gity, F.; Monaghan, S.; Hurley, P. K.; Duffy, R. In *Impact of impurities, interface traps and contacts on MoS₂ MOSFETs: Modelling and experiments*, 2017 47th European Solid-State Device Research Conference (ESSDERC), 11-14 Sept. 2017; 2017; pp 288-291.
256. Chen, K.; Chang, S. In *Phonon limited electron mobility calculation of transition metal dichalcogenide monolayer*, 2016 IEEE 16th International Conference on Nanotechnology (IEEE-NANO), 22-25 Aug. 2016; 2016; pp 139-141.
257. Gunst, T.; Markussen, T.; Stokbro, K.; Brandbyge, M., First-principles method for electron-phonon coupling and electron mobility: Applications to two-dimensional materials. *Physical Review B* **2016**, *93* (3), 035414.
258. Howell, S. L.; Jariwala, D.; Wu, C.-C.; Chen, K.-S.; Sangwan, V. K.; Kang, J.; Marks, T. J.; Hersam, M. C.; Lauhon, L. J., Investigation of Band-Offsets at Monolayer–Multilayer MoS₂ Junctions by Scanning Photocurrent Microscopy. *Nano Letters* **2015**, *15* (4), 2278-2284.
259. Berg, M.; Keyshar, K.; Bilgin, I.; Liu, F. Z.; Yamaguchi, H.; Vajtai, R.; Chan, C.; Gupta, G.; Kar, S.; Ajayan, P.; Ohta, T.; Mohite, A. D., Layer dependence of the electronic band alignment of few-layer MoS₂ on SiO₂ measured using photoemission electron microscopy. *Physical Review B* **2017**, *95* (23), 235406.
260. Keyshar, K.; Berg, M.; Zhang, X.; Vajtai, R.; Gupta, G.; Chan, C. K.; Beechem, T. E.; Ajayan, P. M.; Mohite, A. D.; Ohta, T., Experimental Determination of the Ionization Energies of MoSe₂, WS₂, and MoS₂ on SiO₂ Using Photoemission Electron Microscopy. *ACS Nano* **2017**, *11* (8), 8223-8230.
261. Deng, Q.; Li, Y.; Shen, Y.; Chen, L.; Wang, G.; Wang, S., Numerical simulation on n-MoS₂/p-Si heterojunction solar cells. *Modern Physics Letters B* **2017**, *31* (07), 1750079.
262. Mishra, V.; Smith, S.; Liu, L.; Zahid, F.; Zhu, Y.; Guo, H.; Salahuddin, S., Screening in Ultrashort (5 nm) Channel MoS₂ Transistors: A Full-Band Quantum Transport Study. *IEEE Transactions on Electron Devices* **2015**, *62* (8), 2457-2463.
263. Wickramaratne, D.; Zahid, F.; Lake, R. K., Electronic and thermoelectric properties of few-layer transition metal dichalcogenides. *The Journal of Chemical Physics* **2014**, *140* (12), 124710.
264. Cheiwchanchamnangij, T.; Lambrecht, W. R. L., Quasiparticle band structure calculation of monolayer, bilayer, and bulk MoS₂. *Physical Review B* **2012**, *85* (20), 205302.
265. Cheng, L.; Liu, Y., What Limits the Intrinsic Mobility of Electrons and Holes in Two Dimensional Metal Dichalcogenides? *Journal of the American Chemical Society* **2018**, *140* (51), 17895-17900.
266. Chen, X.; Wu, Z.; Xu, S.; Wang, L.; Huang, R.; Han, Y.; Ye, W.; Xiong, W.; Han, T.; Long, G.; Wang, Y.; He, Y.; Cai, Y.; Sheng, P.; Wang, N., Probing the electron

states and metal-insulator transition mechanisms in molybdenum disulphide vertical heterostructures. *Nature Communications* **2015**, *6*, 6088.

267. Wang, R.; Ruzicka, B. A.; Kumar, N.; Bellus, M. Z.; Chiu, H.-Y.; Zhao, H., Ultrafast and spatially resolved studies of charge carriers in atomically thin molybdenum disulfide. *Physical Review B* **2012**, *86* (4), 045406.

268. Ma, N.; Jena, D., Carrier statistics and quantum capacitance effects on mobility extraction in two-dimensional crystal semiconductor field-effect transistors. *2D Materials* **2015**, *2* (1), 015003.

269. Pal, A.; Cao, W.; Kang, J.; Banerjee, K. In *How to derive the highest mobility from 2D FETs — A first-principle study*, 2017 IEEE International Electron Devices Meeting (IEDM), 2-6 Dec. 2017; 2017; pp 31.3.1-31.3.4.

270. Arora, N. D.; Hauser, J. R.; Roulston, D. J., Electron and hole mobilities in silicon as a function of concentration and temperature. *IEEE Transactions on Electron Devices* **1982**, *29* (2), 292-295.

271. Fiori, G.; Szafranek, B. N.; Iannaccone, G.; Neumaier, D., Velocity saturation in few-layer MoS₂ transistor. *Applied Physics Letters* **2013**, *103* (23), 233509.

272. Takenaka, M.; Ozawa, Y.; Han, J.; Takagi, S. In *Quantitative evaluation of energy distribution of interface trap density at MoS₂ MOS interfaces by the Terman method*, 2016 IEEE International Electron Devices Meeting (IEDM), 3-7 Dec. 2016; 2016; pp 5.8.1-5.8.4.

273. Zhao, P.; Azcatl, A.; Gomeniuk, Y. Y.; Bolshakov, P.; Schmidt, M.; McDonnell, S. J.; Hinkle, C. L.; Hurley, P. K.; Wallace, R. M.; Young, C. D., Probing Interface Defects in Top-Gated MoS₂ Transistors with Impedance Spectroscopy. *ACS Applied Materials & Interfaces* **2017**, *9* (28), 24348-24356.

274. Young, C. D.; Zhao, P.; Bolshakov-Barrett, P.; Azcatl, A.; Hurley, P. K.; Gomeniuk, Y. Y.; Schmidt, M.; Hinkle, C. L.; Wallace, R. M., (Invited) Evaluation of Few-Layer MoS₂ Transistors with a Top Gate and HfO₂ Dielectric. *ECS Transactions* **2016**, *75* (5), 153-162.

275. Azcatl, A.; McDonnell, S.; K. C, S.; Peng, X.; Dong, H.; Qin, X.; Addou, R.; Mordi, G. I.; Lu, N.; Kim, J.; Kim, M. J.; Cho, K.; Wallace, R. M., MoS₂ functionalization for ultra-thin atomic layer deposited dielectrics. *Applied Physics Letters* **2014**, *104* (11), 111601.

276. Gaur, A.; Balaji, Y.; Lin, D.; Adelman, C.; Van Houdt, J.; Heyns, M.; Mocuta, D.; Radu, I., Demonstration of $2e12\text{cm}^{-2}\text{eV}^{-1}$ 2D-oxide interface trap density on back-gated MoS₂ flake devices with 2.5nm EOT. *Microelectronic Engineering* **2017**, *178*, 145-149.

277. Jmol: an open-source Java viewer for chemical structures in 3D. <http://www.jmol.org/>.

278. Liang, Y.; Yoo, H. D.; Li, Y.; Shuai, J.; Calderon, H. A.; Robles Hernandez, F. C.; Grabow, L. C.; Yao, Y., Interlayer-Expanded Molybdenum Disulfide Nanocomposites for Electrochemical Magnesium Storage. *Nano Letters* **2015**, *15* (3), 2194-2202.

279. Yakovkin, I. N., INTERLAYER INTERACTION AND SCREENING IN MoS₂. *Surface Review and Letters* **2014**, *21* (03), 1450039.

280. Schenk, A.; Heiser, G., Modeling and simulation of tunneling through ultra-thin gate dielectrics. *Journal of Applied Physics* **1997**, *81* (12), 7900-7908.

281. Zhu, Y.; Zhou, R.; Zhang, F.; Appenzeller, J., Vertical charge transport through transition metal dichalcogenides – a quantitative analysis. *Nanoscale* **2017**, *9* (48), 19108-19113.

282. Zhang, F.; Zhu, Y.; Appenzeller, J. In *Novel two-terminal vertical transition metal dichalcogenide based memory selectors*, 2017 75th Annual Device Research Conference (DRC), 25-28 June 2017; 2017; pp 1-2.

-
283. Santos, E. J. G.; Kaxiras, E., Electrically Driven Tuning of the Dielectric Constant in MoS₂ Layers. *ACS Nano* **2013**, *7* (12), 10741-10746.
284. Lin, M.-W.; Kravchenko, I. I.; Fowlkes, J.; Li, X.; Poretzky, A. A.; Rouleau, C. M.; Geoghegan, D. B.; Xiao, K., Thickness-dependent charge transport in few-layer MoS₂ field-effect transistors. *Nanotechnology* **2016**, *27* (16), 165203.
285. Su, C.; Tsai, T.; Liou, Y.; Lin, Z.; Lin, H.; Chao, T., Gate-All-Around Junctionless Transistors With Heavily Doped Polysilicon Nanowire Channels. *IEEE Electron Device Letters* **2011**, *32* (4), 521-523.
286. Zhao, D. D.; Nishimura, T.; Lee, C. H.; Nagashio, K.; Kita, K.; Toriumi, A., Junctionless Ge p-Channel Metal–Oxide–Semiconductor Field–Effect Transistors Fabricated on Ultrathin Ge-on-Insulator Substrate. *Applied Physics Express* **2011**, *4* (3), 031302.
287. Cho, S.; Park, S. H.; Park, B.; Harris, J. S. In *Silicon-compatible bulk-type compound junctionless field-effect transistor*, 2011 International Semiconductor Device Research Symposium (ISDRS), 7-9 Dec. 2011; 2011; pp 1-2.
288. Jiang, J.; Sun, J.; Dou, W.; Zhou, B.; Wan, Q., Junctionless in-plane-gate transparent thin-film transistors. *Applied Physics Letters* **2011**, *99* (19), 193502.
289. Colinge, J.-P.; Lee, C.-W.; Ferain, I.; Akhavan, N. D.; Yan, R.; Razavi, P.; Yu, R.; Nazarov, A. N.; Doria, R. T., Reduced electric field in junctionless transistors. *Applied Physics Letters* **2010**, *96* (7), 073510.
290. Lee, M. L.; Fitzgerald, E. A.; Bulsara, M. T.; Currie, M. T.; Lochtefeld, A., Strained Si, SiGe, and Ge channels for high-mobility metal-oxide-semiconductor field-effect transistors. *Journal of Applied Physics* **2004**, *97* (1), 011101.
291. Guan, X.; Zhu, G.; Wei, X.; Cao, J., Tuning the electronic properties of monolayer MoS₂, MoSe₂ and MoSSe by applying z-axial strain. *Chemical Physics Letters* **2019**, *730*, 191-197.
292. Hosseini, M.; Elahi, M.; Pourfath, M.; Esseni, D., Strain-Induced Modulation of Electron Mobility in Single-Layer Transition Metal Dichalcogenides MX₂ (M = Mo, W; X = S, Se). *IEEE Transactions on Electron Devices* **2015**, *62* (10), 3192-3198.
293. Jang, D.; Yakimets, D.; Eneman, G.; Schuddinck, P.; Bardon, M. G.; Raghavan, P.; Spessot, A.; Verkest, D.; Mocuta, A., Device Exploration of NanoSheet Transistors for Sub-7-nm Technology Node. *IEEE Transactions on Electron Devices* **2017**, *64* (6), 2707-2713.
294. Loubet, N.; Hook, T.; Montanini, P.; Yeung, C.; Kanakasabapathy, S.; Guillom, M.; Yamashita, T.; Zhang, J.; Miao, X.; Wang, J.; Young, A.; Chao, R.; Kang, M.; Liu, Z.; Fan, S.; Hamieh, B.; Sieg, S.; Mignot, Y.; Xu, W.; Seo, S.; Yoo, J.; Mochizuki, S.; Sankarapandian, M.; Kwon, O.; Carr, A.; Greene, A.; Park, Y.; Frougier, J.; Galatage, R.; Bao, R.; Shearer, J.; Conti, R.; Song, H.; Lee, D.; Kong, D.; Xu, Y.; Arceo, A.; Bi, Z.; Xu, P.; Muthinti, R.; Li, J.; Wong, R.; Brown, D.; Oldiges, P.; Robison, R.; Arnold, J.; Felix, N.; Skordas, S.; Gaudiello, J.; Standaert, T.; Jagannathan, H.; Corliss, D.; Na, M.; Knorr, A.; Wu, T.; Gupta, D.; Lian, S.; Divakaruni, R.; Gow, T.; Labelle, C.; Lee, S.; Paruchuri, V.; Bu, H.; Khare, M. In *Stacked nanosheet gate-all-around transistor to enable scaling beyond FinFET*, 2017 Symposium on VLSI Technology, 5-8 June 2017; 2017; pp T230-T231.
295. Mertens, H.; Ritzenthaler, R.; Hikavy, A.; Kim, M. S.; Tao, Z.; Wostyn, K.; Chew, S. A.; Keersgieter, A. D.; Mannaert, G.; Rosseel, E.; Schram, T.; Devriendt, K.; Tsvetanova, D.; Dekkers, H.; Demuyne, S.; Chasin, A.; Besien, E. V.; Dangol, A.; Godny, S.; Douhard, B.; Bosman, N.; Richard, O.; Geypen, J.; Bender, H.; Barla, K.; Mocuta, D.; Horiguchi, N.; Thean, A. V. In *Gate-all-around MOSFETs based on vertically stacked horizontal Si*

nanowires in a replacement metal gate process on bulk Si substrates, 2016 IEEE Symposium on VLSI Technology, 14-16 June 2016; 2016; pp 1-2.

296. Kim, S.; Guillorn, M.; Lauer, I.; Oldiges, P.; Hook, T.; Na, M. In *Performance trade-offs in FinFET and gate-all-around device architectures for 7nm-node and beyond*, 2015 IEEE SOI-3D-Subthreshold Microelectronics Technology Unified Conference (S3S), 5-8 Oct. 2015; 2015; pp 1-3.

297. Agarwal, T.; Szabo, A.; Bardou, M. G.; Soree, B.; Radu, I.; Raghavan, P.; Luisier, M.; Dehaene, W.; Heyns, M. In *Benchmarking of monolithic 3D integrated MX2 FETs with Si FinFETs*, 2017 IEEE International Electron Devices Meeting (IEDM), 2-6 Dec. 2017; 2017; pp 5.7.1-5.7.4.

298. Lee, C.; Cline, B.; Sinha, S.; Yeric, G.; Wong, H. P. In *32-bit Processor core at 5-nm technology: Analysis of transistor and interconnect impact on VLSI system performance*, 2016 IEEE International Electron Devices Meeting (IEDM), 3-7 Dec. 2016; 2016; pp 28.3.1-28.3.4.